SAPIENZA
UNIVERSITÀ DI ROMA

Olivine-clinopyroxene-melt cation exchange reactions as a tool for quantitative understanding magma dynamics

PhD Thesis

Flavio Di Stefano

XXXII ciclo

Supervisor:

Prof. Silvio Mollo

Co-Supervisor:

Dr. Piergiorgio Scarlato

Introduction

The overall understanding of volcanic processes has evolved exponentially in the last decades, thanks to the rapid advances of geophysical and geochemical monitoring instruments making possible *real-time* and *in situ* observations of pre-eruptive dynamics. Thus, the study of active volcanoes provides a plethora of data that must be interpreted in light of what we know about the evolution of magmas (e.g., fractional crystallization, magma mixing, assimilation of host rock by magma, degassing and ascent processes). Albeit this goal is still far from being achieved, the modern style of petrology applied to volcanology offers innovative and visionary scenarios in the comprehension of magma dynamics. Following this line of reasoning, the chemistry of melts and crystals recording the intensive thermodynamic variables (i.e., pressure, *P*; temperature, *T*; volatile content and composition of the system, H_2O, *X*) can be used to model the most important processes during the evolution of a magmatic system.

In this study, I have adopted a petrological approach based on the partitioning behavior of major and trace elements between crystals (i.e., olivine and clinopyroxene) and melts on both experimental and natural products, in order to gain quantitative constraints on specific pre-eruptive volcanic processes. In the first part of this PhD thesis, I have experimentally explored the effect of carbonate assimilation on primitive basaltic magmas through the compositional information enclosed in olivine crystals. Divalent cation partitioning (Ni^{2+}, Mg^{2+}, Fe^{2+}, Mn^{2+}, Ca^{2+}) between olivine and decarbonated melts have been discussed and compared with previous models to gain refined predictive equations that more accurately quantify the geochemical evolution of primitive skarn environments. Concomitantly, Rare Earth Elements (REE), Y, and Sc partition coefficients between olivine and basaltic melts assimilating variable $CaCO_3$ contents have been debated in the framework of the crystal lattice strain theory (i.e., optimum ionic radius, r_0; Young Modulus, *E*; strain-free partition coefficient, D_0). The comparison between cumulates and magmatic skarns from the Colli Albani Volcanic District (Italy) and experiments from this PhD study provides quantitative

constraints on the geochemical changes of olivine phenocrysts and their melt inclusions as a function of carbonate assimilation in terms of both major and trace element partitioning.

In the second part of this PhD thesis, the compositional information recorded in chemically zoned clinopyroxene phenocrysts from the recent 2003-2017 activity of Stromboli volcano (Aeolian Islands, Italy) have been used to unravel the most effective pre-eruptive volcanic processes driving the geochemical evolution of the magmatic plumbing system. The Present-day (<1.2 kyr) activity of Stromboli is fed by a vertically-extended mush column with an open-conduit configuration in which the hot and mafic magma (low porphyritic or *lp*-magma) from depth is continuously injected in the homogeneous shallow reservoir (highly porphyritic or *hp*-magma). Clinopyroxene phenocrysts exhibit marked diopside-augite heterogeneities caused by continuous *lp-hp* magma mixing and antecryst recycling testifying to the continuous disruption and cannibalism of relic antecrysts from the mush. The transition between diopside and augite has been used to establish the *P*-*T*-H_2O crystallization conditions over times and to quantify minimum residence times of diopsidic antecrysts and diopsidic recharge bands. On this basis, I argued a distinct phase in the life of Stromboli volcano commenced at least after the 2003 paroxysm. This phase is characterized by more efficient mechanisms of mush disruption and cannibalism, in concert with gravitational instability of the solidification front, involving diopsidic antecrysts remobilization and transport by *lp*-magmas permeating the mush.

Olivine compositional changes in primitive magmatic skarn environments: A reassessment of divalent cation partitioning models to quantify the effect of carbonate assimilation

Flavio Di Stefano[1,*], Silvio Mollo[1,2], Piergiorgio Scarlato[2], Manuela Nazzari[1,2], Olivier Bachmann[3], Marco Caruso[1]

[1]Dipartimento di Scienze della Terra, Sapienza-Università di Roma, P.le Aldo Moro 5, 00185 Roma, Italy

[2]Istituto Nazionale di Geofisica e Vulcanologia, Via di Vigna Murata 605, 00143 Rome, Italy

[3]Department of Earth Sciences, Institute of Geochemistry and Petrology, ETHZ, Clausiusstrasse 25, 8092 Zurich, Switzerland

Abstract

The geochemical evolution of olivine from primitive magmatic skarn environments has been studied by atmospheric pressure experiments carried out at 1,250, 1,200, and 1,150 °C under QFM oxygen buffering conditions. The starting materials were three synthetic basalts (i.e., $^{melt}Mg\#_{78}$, $^{melt}Mg\#_{75}$, and $^{melt}Mg\#_{72}$) doped with variable amounts of $CaCO_3$, in order to reproduce the natural concentration levels of CaO-rich magmas interacting with the skarn rock shells. Results from decarbonation experiments evidence that the crystallization of Fo-CaO-rich, NiO-poor olivines is more favored at higher temperatures when primitive basaltic magmas assimilate increasing amounts of carbonate materials. The number of large size Ca cations entering olivine crystal lattice is proportional to the amount of Ca-O-Si bonds available in the melt. Due to differences between Fe^{2+} and Mg cation radii, the Ca-Fe^{2+} substitutions into M2 crystallographic site are more facilitated than Ca-Mg ones, thus enhancing the forsterite component in olivine. The partitioning behavior of Ni, Mg, Fe^{2+}, Mn, and Ca between olivine and melt has been also investigated to better understand cation redistribution mechanisms at the magma-carbonate reaction zone. In this context, some partitioning models from the literature have been refined to more accurately quantify the geochemical evolution of primitive skarn systems. Under the effect of $CaCO_3$ assimilation, the partitioning of divalent cations, can be parameterized as a function of temperature, bulk composition (mostly, CaO and MgO contents in both olivine and melt) and melt structure (expressed as the number of non-bridging oxygens per tetrahedrally coordinated cations). Conversely, the exchange partition coefficients between Fe^{2+}/Ca/Mn/Ni and Mg do not vary significantly as a function of temperature and $^{melt}Mg\#$, due to the limited influence of these parameters on the melt structure. In turn, cation exchange reactions are primarily controlled by the strong depolymerizing effect of $CaCO_3$ assimilation that increases the number of structural sites critically important to accommodating network-modifying cations in the melt phase. The comparison between cumulates and magmatic skarns from the Colli Albani Volcanic District (Italy) and experiments from this study provides quantitative constraints on

the geochemical evolution of olivine phenocrysts and their melt inclusions as a function of carbonate assimilation.

1. Introduction

Crustal contamination may significantly contribute to the differentiation path of magma (DePaolo, 1981; Foland et al., 1993; Patiño Douce, 1999; Spera and Bohrson, 2001, 2004; Barnes et al., 2005; Mollo et al., 2011; Del Bello et al., 2014). This is particularly true during magma-carbonate interaction which is characterized as a multi-stage reaction zone advancing from the carbonate wall-rock towards the innermost part of the magma chamber (Wenzel et al., 2002; Gaeta et al., 2009; Mollo et al., 2010; Di Rocco et al., 2012; Mollo and Vona, 2014). The interaction mechanism is generally associated with the formation of three distinct skarn domains (Di Rocco et al., 2012): (1) exoskarns i.e., thermometamorphic rocks derived by decarbonation of the protolith, (2) endoskarns i.e., magmatic rocks derived by crystallization and desilication phenomena at the exoskarn-magma interface, and (3) cumulates i.e., highly crystalline rocks derived by magma contamination and crystal accumulation at the endoskarn-magma interface. The principal products of carbonate thermal decomposition are the formation of CaO-rich melts and the release of CO_2 (Deegan et al., 2010; Mollo et al., 2010, 2011, 2013a; Freda et al., 2011). This latter has important implications for anomalously high CO_2 degassing rates currently estimated at several continental arc volcanoes. Indeed, in mature continental arcs reworking of crustal limestone by hot mafic magmas may be an important source of CO_2 flux (Mason et al., 2017). For example, Carter and Dasgupta (2015) have shown that magma-induced upper plate decarbonation alone may potentially contribute to the excess of CO_2 released into the atmosphere (i.e., up to ~3% of the current global arc CO_2 flux may be crustally derived). Further experimental data have also illustrated that melt composition and melt fraction are effective controlling factors in the transition from assimilation to skarnification, and that both heat and aqueous fluids released from an intruding magma may enhance significantly CO_2 degassing (Carter and Dasgupta, 2016).

During magma-carbonate interaction, the exoskarn domain is characterized by low temperature, metamorphic/metasomatic reactions where the oxidative capacity of CO_2-rich fluids (X_{CO2}>0.99) leads to high oxidation conditions (≥MH buffer; Di Rocco et al., 2012). The endoskarn domain is governed by significant magma cooling and differentiation under moderate-to-high oxidation conditions (≥NNO buffer; Wenzel et al., 2002). The abundant crystallization of CaTs-rich clinopyroxene phenocrysts (Mollo et al., 2010; Carter and Dasgupta, 2015) produces silica-poor, alkali-rich magmas typical of ultrapotassic volcanism (Gaeta et al., 2009). The cumulate domain represents the primitive skarn environment where high temperature, less oxidized (~QFM buffer), primitive magmas fractionate Fo-rich olivine phenocrysts accumulating at the base and periphery of the magma chamber (Di Rocco et al., 2012). Considering the temporal and spatial relationships between exoskarns, endoskarns, and cumulates, the occurrence of olivine as liquidus phase and its compositional evolution are strictly dependent on the progressive advancement of the magma-skarn interface, the thermal (differentiation) path of the system, and the degree of CaO contamination (Wenzel et al., 2002; Barnes et al. 2005; Chadwick et al., 2007; Coulson et al., 2007; Freda et al., 2008; Iacono Marziano et al., 2008; Gaeta et al., 2009; Di Rocco et al., 2012; Jolis et al., 2015). In this scenario, the overall skarn environment acts as a continuous source of CO_2 gas phase and CaO-rich melts that variably interact with primitive basaltic magmas, thus controlling their geochemical evolution under olivine-saturated to olivine + clinopyroxene-cosaturated to clinopyroxene-saturated conditions (cf. Gaeta et al., 2009).

The purpose of this study is to experimentally investigate the early stage of carbonate assimilation when high temperature, primitive basaltic magmas assimilate variable amounts of carbonate material and then equilibrate with olivine phenocrysts. These experimental data allow to better constrain the effect of CaO contamination on the evolutionary behavior of the primitive magmatic skarn environment that is represented by the endoskarn domain. The partitioning of divalent cations (i.e., Ni, Mg, Fe, Mn, and Ca) between olivine and melt has been also investigated due to its importance in estimating the solidification temperature of rocks (e.g., Hart and Davis, 1978;

Ford et al., 1983; Beattie, 1993; Putirka 2005, 2008; Putirka et al., 2007, 2011; Wang and Gaetani, 2008; Li and Ripley, 2010; Matzen et al., 2013; Pu et al., 2017), in ascertaining the equilibrium condition of minerals (e.g., Roeder and Emslie, 1970; Leeman and Scheidegger, 1977; Snyder and Carmichael, 1992; Putirka 2005, 2016; Toplis, 2005; Filiberto and Dasgupta, 2011), and in understanding magmatic processes (e.g., Danyushevsky and Plechov, 2011; Mollo et al., 2015). In this context, several olivine-melt partitioning equations published over the last decades have been collected and integrated all together into an Excel spreadsheet submitted online as supplementary material (Hart and Davis, 1978; Beattie et al., 1991; Snyder and Carmichael, 1992; Beattie, 1993; Jones, 1995, 2016; Libourel, 1999; Putirka, 2005, 2016; Toplis, 2005; Putirka et al., 2007, 2011; Wang and Gaetani, 2008; Pu et al., 2017). The equations more suitable for modeling decarbonation data from this study have been selected, discussed and reappraised in terms of temperature and compositional variations during magma-carbonate interaction. More specifically, the predictive ability of these equations has been improved by including compositional parameters that more accurately describe the variance of the data obtained from decarbonation experiments.

2. Starting materials, experimental conditions and analytical methods

Three different basaltic starting materials were synthesized in batches of ~2 g from pure oxides and carbonates mixed by grinding under ethanol in an agate mortar for ~1 h. These mixtures were chosen in order to obtain three basalts with different primitive characters of $^{melt}Mg\#_{72}$, $^{melt}Mg\#_{75}$, and $^{melt}Mg\#_{78}$ [$^{melt}Mg\# = X_{MgO} / (X_{MgO} + X_{FeO}) \times 100$, where X_{FeO} refers to FeO recalculated at the QFM buffer, according to the formula of Kress and Carmichael (1991)] (Table 1S). Ni was added to the powdered mixture as solution with nominal concentration of 1,000 ppm. To guarantee obeyance of Henry's Law (Mysen 2006), the Ni concentration is similar to that observed in natural basaltic rocks (cf. Mollo et al., 2013b). A Fe pre-saturated Pt-crucible containing the synthetic powder was loaded in a 1 atm vertical tube CO-CO_2 gas-mixing furnace at the quartz-fayalite-magnetite (QFM) buffer. Melting experiments were conducted at the HP-HT Laboratory of Experimental Volcanology and

Geophysics of the Istituto Nazionale di Geofisica e Vulcanologia (INGV) in Rome, Italy. The temperature was kept at 900 °C for 1 h to ensure decarbonation and, then, was raised up to 1,600 °C and kept for 1 h to ensure melting and to obtain glass starting material. The resulting glass was removed from the Pt-crucible and, then, powdered. Backscattered images and microprobe analyses performed on chips extracted from top, middle, and bottom of the Pt-crucible, demonstrated homogeneity and the absence of crystalline phases. In order to minimize loss of transition metals, some aliquots of the powder were previously loaded into the Pt-crucible and run for 3 h at 1,600 °C to saturate the crucible (cf. Conte et al., 2006). The sample holder was then quenched and cleaned in a hot HF solution. The same approach was adopted to saturate the Pt-wire (0.1 mm in diameter) used for the equilibrium experiments conducted at 1 atm and the QFM buffer. Through this strategy, the Fe loss from the samples was kept to <5% of the initial amount. Notably, all the experiments were carried out at 1 atm on the basis of the following considerations: i) our magma-carbonate interaction experiments can be more properly compared with previous studies investigating and modeling the partitioning of divalent cations between olivine and melt at ambient pressure (e.g., Roeder and Emslie, 1970; Leeman and Scheidegger, 1977; Hart and Davis, 1978; Snyder and Carmichael, 1992; Kohn and Schofield, 1994; Jones, 1995, 2016; Beattie, 1993; Libourel, 1999; Wang and Gaetani, 2008), ii) olivine is always the liquidus phase and its stability field increases at the expense of clinopyroxene (Snyder and Carmichael, 1992; Mollo et al., 2015), iii) cation exchange reactions in olivine do not substantially change from low to moderate crustal depths (e.g., Roeder and Emslie, 1970; Takahashi, 1978; Sack et al., 1987; Gee and Sack, 1988; Kushiro and Mysen, 2002; Toplis, 2005; Matzen et al., 2011), and iv) the effect of H_2O and P_{H2O} on olivine stability is practically negligible in primitive magmatic skarn environments due to the strong amount (~45 wt.%) of CO_2 released during calcite thermal decomposition (Wenzel et al., 2002; Di Rocco et al., 2012). The equilibrium temperature was measured by a Pt-$Pt_{90}Rh_{10}$ thermocouple located within 1 cm of the sample chandelier holding the experimental Pt-loops (about 1.5 mm in diameter) charged with about 45 μg of powdered starting material (cf. Mollo and Vona, 2014). The oxygen fugacity was monitored

and maintained constant over the experimental temperatures of 1,150, 1,200 and 1,250 °C by means of an yttria-doped-zirconia solid electrolyte oxygen sensor ($SIRO_2$, Ceramic Oxide Fabricators, Ltd., Australia) and two digital thermal mass flow meters (for CO and CO_2) controlled via software. The $^{melt}Mg\#_{72}$, $^{melt}Mg\#_{75}$, and $^{melt}Mg\#_{78}$ basaltic powders were also doped with 0, 10, and 20 wt.% of $CaCO_3$ in order to obtain total CaO contents of ~11, ~16, and ~22 wt.%, respectively. At a given experimental temperature, three Pt-loops containing basalts with the same $^{melt}Mg\#$ but different CaO contents were simultaneously suspended within the furnace. The superliquidus temperature of 1,300 °C was reached in 1 h starting from room temperature and it was maintained for 0.5 h before beginning cooling. It was experimentally verified that no crystalline phases formed during thermal pre-treatment at 1,300 °C. The samples were cooled at a rate of 30 °C/h from 1,300 °C down to the final target temperature that was kept constant for 72 h. Each experiment was fast-quenched by dropping the charge into a water bath. The run product was mounted in epoxy, and a polished thin section was produced from the epoxy block. According to previous reversal and cooling rate experiments conducted by Mollo et al. (2013b, 2013c) on similar basalts, the experimental duration of 72 h is sufficient to ensure the achievement of mineral-melt chemical equilibrium and ferric-ferrous equilibration in the melt at atmospheric pressure. Vetere et al. (2013) have also demonstrated that the relaxation kinetics of basaltic melts are extremely rapid in time (i.e., from milli- to micro-seconds) and independent of the superheating paths used in laboratory.

Major oxide analyses of experimental products were performed with a Jeol-JXA8200 EDS-WDS combined electron microprobe equipped with five wavelength-dispersive spectrometers and installed at the HP-HT Lab of INGV. The analytical conditions were 15 kV accelerating voltage and 10 nA beam current, 5 μm beam diameter, and 20 s counting time. The following standards were adopted for the various chemical elements: jadeite (Si and Na), corundum (Al), forsterite (Mg), andradite (Fe), rutile (Ti), orthoclase (K), barite (Ba), apatite (P), spessartine (Mn) and metallic nickel (Ni). Sodium and potassium have been analyzed first to reduce possible volatilization effects. The precision of the microprobe was measured through the analysis of well-characterized synthetic oxides

and minerals. Data quality was ensured by analyzing standard materials as unknowns based on counting statistics, analytical precision and accuracy were better than 5% for all cations (Tables 2S and 3S).

The Ni concentration (at ppm levels) in the residual glass was too low to be accurately measured via microprobe. Thus, further analyses were performed at the Institute of Geochemistry and Petrology of the ETH Zürich, Switzerland. Data were collected through a 193 nm excimer laser coupled with a second generation two-volume constant geometry ablation cell (Resonetics:S-155LR) and a high-sensitivity, sector-field inductively-coupled plasma mass spectrometer (ICP-MS; Thermo:Element XR). Points with a spot size of 13 μm were set on chemically homogeneous portions of the material previously analyzed by electron microprobe, and ablated with a pulse rate of 10 Hz and an energy density of 3.5 J/cm^3 for 40 sec. The isotope was analyzed relative to an internal standard of known composition (i.e., NIST612). A second standard (i.e., GSD-1G) was used as an unknown to check the quality of data during each analytical run. ^{29}Si was used as internal standard. The analytical precision corresponds to the 1 sigma errors calculated from variations in replicate analyses that resulted invariably greater than the fully integrated 1 sigma errors determined from counting statistics alone.

3. Results

3.1. Phase relations and abundances

Olivine, clinopyroxene, titanomagnetite, and glass occur in the experimental charges, showing variable proportions as a function of temperature, starting melt composition (i.e., ^{melt}Mg#), and degree of $CaCO_3$ assimilation (Table 1). Modal phase abundances have been derived by mass balance calculations (Table 1), yielding relative low residual sum of squares ($\Sigma r^2 < 0.75$). This points to a fairly good conservation of mass relative to the chemical analyses of crystals and glasses, suggesting (near-)equilibrium crystallization conditions (Stormer and Nicholls, 1978). The most important features of the experimental charges can be schematized as follows (Table 1): i) olivine saturates the

basaltic melt in all the experimental charges, ii) the amount of olivine is maximum (12%) in the most primitive $^{melt}Mg\#_{78}$ experimental charge and decreases with increasing $CaCO_3$ assimilation, iii) at 1,250 °C, clinopyroxene is always absent, irrespective of the starting melt composition (i.e., $^{melt}Mg\#$) and the amount of $CaCO_3$ assimilated, iv) at 1,200 °C, clinopyroxene does not crystallize from the undoped experimental charges ($^{melt}Mg\#_{78}$, $^{melt}Mg\#_{75}$, and $^{melt}Mg\#_{72}$) but occurs in the most differentiated $^{melt}Mg\#_{72}$ basalt doped with 10 and 20 wt.% $CaCO_3$, v) at 1,150 °C, clinopyroxene is ubiquitous in basalts assimilating 20 wt.% $CaCO_3$ and its modal content increases from ~9% to ~20%, as the melt composition shifts from $^{melt}Mg\#_{78}$ to $^{melt}Mg\#_{72}$, vi) titanomagnetite is extremely rare (~1%), appearing only at 1,150 °C in the most differentiated $^{melt}Mg\#_{72}$ basalt, vii) at 1,250 °C, olivine nucleates and grow as large, euhedral, and isolated crystals showing regular planar faces and lengths up to ~3 mm, and viii) at 1,150 °C, an intricate network of elongated crystals occurs, due to the enlargement of the stability field of clinopyroxene at the expense of olivine (see mineral proportions in Table 1).

3.2. Glass chemistry

The glass analyzed around olivine and clinopyroxene is chemically homogeneous (Table 2S), attesting that chemical nutrients were supplied to the growing crystals at equilibrium proportions (note that equilibrium values have been derived for the Fe^{2+}-Mg exchange reaction between olivine and melt; see discussion below). As the temperature decreases, the glass composition remains almost constant in terms of SiO_2, whereas Na_2O + K_2O increase with olivine and clinopyroxene crystallization (Table 2S). The most important chemical variations occur as a function of $CaCO_3$ assimilation, causing melt desilication (i.e., SiO_2 decreases from ~52 to ~43 wt.%) and decarbonation (i.e., CaO increases from ~11 to ~22 wt.%), in agreement with what observed in previous studies (Fulignati et al., 2000; Gaeta et al., 2009; Mollo et al., 2010; Di Rocco et al., 2012; Gozzi et al., 2014; Mollo and Vona, 2014; Ammannati et al., 2016). Residual glasses from the most primitive $^{melt}Mg\#_{78}$ basalt are characterized by the highest contents of CaO, TiO_2, Al_2O_3, and MnO (Table 2S),

corresponding to the lowest degree of clinopyroxene crystallization (Table 1). In contrast, the concentrations of FeO, Na_2O, and K_2O are maximum in the residual glasses formed from the most evolved clinopyroxene-saturated $^{melt}Mg\#_{72}$ starting composition (Table 2S). The TAS (total alkali vs. silica; Le Bas et al., 1986) diagram classifies the residual glasses as basalt-basaltic andesite (from 0 to 10 wt.% $CaCO_3$ assimilation) and basanite-tephrite (20 wt.% $CaCO_3$ assimilation).

3.3. Mineral chemistry

Olivine is the liquidus phase in all the experimental charges and its chemistry varies considerably as a function of the experimental conditions (Table 3S). As the temperature decreases, MgO is less favorably incorporated into olivine crystal lattice, whereas the opposite occurs for FeO, MnO, NiO, and CaO (Fig. 1). The most primitive $^{melt}Mg\#_{78}$ basalt forms olivines with the highest MnO, MgO, and CaO concentrations and the lowest FeO and NiO contents (Fig. 1). With increasing $CaCO_3$ assimilation, olivine shows MgO and CaO enrichments, counterbalanced by FeO, MnO, and NiO depletions. Olivines with CaO contents up to 2.33 wt.% are consistent with those (1.31-2.36 wt.% CaO) equilibrated by previous magma-carbonate interaction experiments conducted on basaltic to shoshonitic compositions doped with $CaCO_3$ amounts variable from 5 to 20 wt.% (cf. Conte et al., 2009; Mollo et al., 2010; Jolis et al., 2013). In order to compare olivine components from this study with those reported in literature (e.g., Wenzel et al., 2001, 2002; Gaeta et al., 2009; Iacono Marziano et al., 2009; Dallai et al., 2011; Di Rocco et al., 2012; Gozzi et al., 2014; Hayes et al., 2015; Redi et al., 2017), the mineral stoichiometry has been calculated in Table 3S as a simple solid solution of forsterite (Fo; Mg_2SiO_4) and fayalite (Fa; Fe_2SiO_4), following the same method adopted by previous authors. The maximum Fo_{93} content is measured for crystals from the primitive $^{melt}Mg\#_{78}$ basalt assimilating 20 wt.% of $CaCO_3$ at 1,250 °C (Table 3S). The Fo content decreases from 93 to 87 with decreasing $^{melt}Mg\#$, temperature, and $CaCO_3$ (Table 3S). For the sake of completeness, a more comprehensive solution model for olivine components has been also used in this study, by considering forsterite, fayalite, larnite or calcio-olivine (Ca-ol; Ca_2SiO_4), and tephroite (Teph; Mn_2SiO_4) as end-

members (see Table 3S). This strategy allows to better evidence that, with increasing $CaCO_3$ assimilation, Fo and Ca-ol remarkably increase at the expense of Fa and Teph (Fig. 2).

The clinopyroxene chemistry closely resembles that already discussed in previous experimental works (Mollo et al., 2010; Mollo and Vona, 2014), showing preferential enrichments in TiO_2, Al_2O_3, FeO, and CaO during $CaCO_3$ assimilation, in concert with a remarkable depletion in MgO (Table 4S). The molecular proportions of Ca-Tschermak (CaTs, $CaAl_2SiO_6$), CaFe-Tschermak (CaFeTs; $CaFeSiAlO_6$), and CaTi-Tschermak (CaTiTs, $CaTiAl_2O_6$) are observed to increase from 0.08 to 0.11, from 0.01 to 0.03, and from 0.05 to 0.07, respectively. In contrast, diopside (Di, $CaMgSi_2O_6$) and enstatite (En, $Mg_2Si_2O_6$) decrease from 0.51 to 0.45 and from 0.07 to 0.02, respectively (Table 4S).

Magnetite, which appears only in the most evolved $^{melt}Mg\#_{72}$ basalt equilibrated at 1,150 °C, shows an increase of Al_2O_3, FeO_{tot}, MnO, and MgO with increasing $CaCO_3$, as well as a likewise decrease of TiO_2 (Table 5S). Consequently, the ulvospinel (Usp, $TiFe_2O_4$) component is observed to decrease from 0.36 to 0.14 (Table 5S).

4. Discussion

4.1. Geochemical evolution of olivine in primitive magmatic skarn environments

Relative to the formation of natural magmatic skarn environments (Dunworth and Wilson, 1998; Battistini et al., 2001; Wenzel et al., 2001, 2002; Gaeta et al., 2009; Dallai et al., 2011; Di Rocco et al., 2012; Del Bello et al., 2014; Gozzi et al., 2014; Redi et al., 2017), data from this study allow to better understand the geochemical evolution of olivine (Figs. 1 and 2) from the interior of the magma chamber (i.e., uncontaminated basalt) towards the carbonate wall-rock (i.e., contaminated basalt). This makes also possible to quantify the complex interplay between temperature and bulk compositional changes during magma cooling, crystallization, and carbonate assimilation. For example, at the highest temperature of 1,250 °C, clinopyroxene does not crystallize from $^{melt}Mg\#_{78}$ and $^{melt}Mg\#_{72}$ basalts, even if the degree of assimilation increases by up to 20 wt.% $CaCO_3$. Therefore,

at high temperature, olivine is energetically more favored than clinopyroxene (Table 1). The composition of olivine shifts from Fo_{87} to Fo_{93} when the melt desilication proceeds from 50 to 42 wt.% SiO_2 with increasing $CaCO_3$. This is consistent with the chemistry (Fo_{88-91}) of natural olivine phenocrysts from cumulate and endoskarn rocks formed at the early stage of carbonate assimilation by basaltic magmas (Dunworth and Wilson, 1998; Wenzel et al., 2001, 2002; Gaeta et al., 2009; Dallai et al., 2011; Di Rocco et al., 2012; Gozzi et al., 2014; Redi et al., 2017). Natural products are generally characterized by orthocumulate to mesocumulate to adcumulate textures (Irvine, 1982), resulting from the aggregation of mafic crystals in a reaction-cumulate zone at the periphery of the magma chamber, where CaO-rich melts are persistently extracted from the skarn rock shells (Wenzel et al., 2002). More specifically, primitive skarn-bearing dunite cumulates result from high temperature reactions commencing at 1,200-1,260 °C and oxygen fugacity close to QFM buffer (Wenzel et al., 2002). Under such circumstances, the activity of CaO and the Fe speciation in the pristine melt facilitate the incorporation of Ca cations into the more stable (i.e., Fe^{2+}-bearing) olivine phenocrysts (Wenzel et al., 2001; Fulignati et al., 2004; Dallai et al., 2011; Redi et al., 2017). Experimental olivines obtained during assimilation of 10 wt.% $CaCO_3$ show CaO contents up to ~1.5 wt.% (Fig. 1), resembling the natural concentration levels (~1.4 wt.% CaO) measured in primitive magmatic skarn environments. At 1,200 °C, the assimilation of 10 wt.% $CaCO_3$ expands the stability field of clinopyroxene (~8%), but this phenomenon is observed only for the most evolved $^{melt}Mg\#_{72}$ basalt (Table 1). At 1,150 °C, clinopyroxene dominates the phase assemblage (~12%) of the uncontaminated $^{melt}Mg\#_{72}$ basalt and its amount increases (~20%) with increasing $CaCO_3$. In contrast, $^{melt}Mg\#_{75}$ and $^{melt}Mg\#_{78}$ basalts segregate clinopyroxene (~5-15%) only under the effect of $CaCO_3$ assimilation, evidencing that olivine is the unique stable mineral in the undoped primitive magmas (Table 1). This means that, at the magma chamber-host rock interface, the cosaturation surface of olivine and clinopyroxene is strictly dependent on the physicochemical state of the system in terms of *T*, $^{melt}Mg\#$, and $CaCO_3$ content.

In the experimental charges doped with 20 wt.% $CaCO_3$, the modal abundance of clinopyroxene (9-20%) is much lower than that (~40-90%) observed in highly decarbonated natural environments where magmatic rocks are tephrites, phonotephrites, and foidites. Indeed, the oxidative capacity of CO_2 released during $CaCO_3$ decomposition at the skarn shells produces highly oxidized melts (fO_2 ~ MH buffer) with silica-poor ($SiO_2 \approx$ 40-46 wt.%), alkali-rich ($Na_2O + K_2O \approx$ 6-11 wt.%) compositions (Fulignati et al., 2000, 2004; Gaeta et al., 2009; Mollo et al., 2010; Di Rocco et al., 2012; Gozzi et al., 2014; Mollo and Vona, 2014; Ammannati et al., 2016). The desilication reaction is greatly controlled by the fractionation of (Fe^{3+}-bearing) clinopyroxenes at temperatures of 800-1,150 °C, largely exceeding the thermal barrier (600 °C) for calcite breakdown (Lentz, 1999; Mollo et al., 2013a). Clinopyroxene-rich skarn shells (with minor or absent olivine) control the formation of highly decarbonated/oxidized rocks solidifying at low ($T \leq$1,150 °C) thermal conditions (Gaeta et al., 2009; Mollo et al., 2010; Di Rocco et al., 2012). In contrast, the degree of clinopyroxene crystallization is much lower from less oxidized basaltic magmas equilibrated at 1,200-1,250 °C. As a consequence, there is not an effective competitor for CaO incorporation in olivine crystals and the concentration of alkali in the residual melt does not substantially increase due to the relative low olivine content. This phenomenon is typical of high temperature systems where primitive endoskarn-bearing dunite cumulates record mineralogical and textural evidences of mixing between olivine-saturated magmas and CaO-rich melts (Wenzel et al., 2001, 2002; Hayes et al., 2015).

From a compositional point of view, experimental data from this study evidence that Fo in olivine is positively correlated with T, ^{melt}Mg#, and $CaCO_3$, whereas Ca-ol is mostly controlled by the degree of $CaCO_3$ assimilation (Fig. 2). This geochemical variation can be expressed by the general reaction:

$$\left[2CaCO_3\right]^{cal} + \left[SiO_2 + 2MgO\right]^{melt} + \left[Fe_2SiO_4\right]^{Ol} = \left[Mg_2SiO_4 - Ca_2SiO_4\right]^{Ol} + \left[2FeO\right]^{melt} + \left[2CO_2\right]^{fluid} \quad (1)$$

Reaction (1) describes the high temperature, less oxidized (fO_2 ~ QFM buffer) domain that develops at the periphery of magma chambers when olivine-saturated basaltic magmas are initially contaminated by CaO-rich melts from the skarn shells. In this scenario, olivine occurs as a stable phase at the early stage of $CaCO_3$ assimilation, showing high-Fo, high-CaO, and low-NiO contents (Dallai et al., 2011; Ammannati et al., 2016). Notably, NiO in the experimental Fo_{87-93} olivines decreases from 0.65 to 0.15 wt.% with increasing $CaCO_3$, in agreement with that observed for natural phenocrysts (Fo_{86-93} and 0.09-0.53 wt.% NiO) from cumulate rocks (Wenzel et al., 2001, 2002; Gaeta et al., 2009; Dallai et al., 2011; Di Rocco et al., 2012; Ammannati et al., 2016). Ni basically occupies the small M1 crystallographic site of olivine (Annersten et al., 1982; Galoisy et al., 1995), responding to high crystal field effects (Wood, 1974). At magmatic temperatures, Fe^{2+} is preferentially ordered in the M2 site (Heinemann et al., 1999), whereas Mg is randomly distributed between M1 and M2 sites. Since Ca is essentially restricted to only the large M2 site, the effect of carbonate assimilation increases the number of Ca-Fe^{2+} substitutions (Coogan et al., 2005). The high CaO abundance in olivine (Fig. 1) is addressed to the strong codependency between Fo molecule and the mafic melt composition (Libourel, 1999). According to the equilibrium Fe-Mg exchange reaction (Roeder and Emslie, 1970), the Mg/Fe^{2+} ratio of olivine increases with increasing the MgO/FeO ratio of the melt, thus enhancing the Fo component (Fig. 2). At the same time, mixing phenomena between uncontaminated basalts and CaO-rich melts from the skarn shells lead to the formation of desilicated and decarbonated magmas. To better demonstrate this contamination mechanism, the activities of silica (a_{SiO2}^{melt}), calcium (a_{CaO}^{melt}), and magnesium (a_{MgO}^{melt}) of the experimental melts have been calculated through the pseudo-activity models of Bottinga at al. (1981), Libourel (1999), and Leeman (1978), respectively:

$$a_{SiO2}^{melt} = X_{SiO2}^{melt} / \left(X_{SiO2}^{melt} + X_{TiO2}^{melt} + X_{Na2O}^{melt} + X_{K2O}^{melt} \right), \quad (2)$$

$$a_{CaO}^{melt} = \left(X_{CaO}^{melt} + X_{Na2O}^{melt} + X_{K2O}^{melt}\right)^2 / \left(X_{SiO2}^{melt} + X_{TiO2}^{melt}\right), \text{ and} \quad (3)$$

$$a_{MgO}^{melt} = X_{MgO}^{melt} / \left(X_{MgO}^{melt} + X_{FeO}^{melt} + X_{MnO}^{melt} + X_{CaO}^{melt} + X_{NiO}^{melt}\right) \quad (4)$$

Where X_i^{melt} is the molar fraction of the element *i* in the melt. Results from these calculations are plotted in the [(Fo + Ca-ol)/Fa] vs. [(a_{CaO}^{melt} + a_{MgO}^{melt})/a_{SiO2}^{melt})] diagram (Fig. 3) showing an appreciable positive correlation (R^2 = 0.67) between the olivine molecule proportions and the melt activity-composition relations. Note that the [(a_{CaO}^{melt} + a_{MgO}^{melt})/a_{SiO2}^{melt})] term acts as an indicator of open-system processes, accounting for either the CaO-rich, SiO_2-poor nature of the contaminated basalts, or the primitive character of the melt. According to the early formula proposed by Leeman (1978), [(a_{CaO}^{melt} + a_{MgO}^{melt})/a_{SiO2}^{melt})] should be intended as a complex activity function where the activities of SiO_2, CaO, and MgO are approximated according to equations (2), (3), and (4). The carbonate assimilation process is accompanied by an increase of a_{CaO}^{melt} and a decrease of a_{SiO2}^{melt} (Ferguson, 1978; Libourel, 1999). This facilitates the incorporation of Fo in olivine (Fig. 3) that, in turn, is governed by the activity of silica in the melt (Leeman, 1978). Note also that a_{MgO}^{melt} greatly enlarges the stability field of olivine (Roeder and Emslie, 1970; Ford et al., 1983; Snyder and Carmichael, 1992; Bédard, 2005). As a consequence, olivine crystallization is ubiquitous in basaltic systems contaminated by $CaCO_3$ assimilation up to 20 wt.%, despite the stability field of olivine is reduced in favor of clinopyroxene (Table 1).

Previous experimental (Mollo et al., 2010; Jolis et al., 2013; Mollo and Vona, 2014; Carter and Dasgupta, 2015) and natural (Gaeta et al., 2009; Troll et al., 2012, 2013; Doroshkevich et al., 2012; Spandler et al., 2012; Del Bello et al., 2014) studies have documented that a high-calcium activity in magmas favors abundant clinopyroxene formation. The chemistry of clinopyroxene

progressively changes from the magmatic domain towards the skarn shells, according to the following expression (Mollo et al., 2010; Mollo and Vona, 2014):

$$\begin{aligned}&\left[2CaCO_3\right]^{cal}+\left[2Al_2O_3+TiO_2+FeO\right]^{melt}+\left[CaMgSi_2O_6-Mg_2Si_2O_6\right]^{Cpx}=\\&\left[CaAlAlSiO_6-CaFeAlSiO_6-CaTiAlSiO_6\right]^{Cpx}+\left[3MgO+SiO_2\right]^{melt}+\left[2CO_2\right]^{fluid}\end{aligned}\qquad(5)$$

Results from this study conform to reaction (5), attesting that CaTs + CaFeTs + CaTiTs in clinopyroxene increase with $CaCO_3$ by lowering the amount of Di + En (Table 2S). Reactions (1) and (5) can be also combined to describe the spatial and temporal evolution of a basaltic system contaminated by carbonate material:

$$\begin{aligned}&\left[4CaCO_3\right]^{cal}+\left[2Al_2O_3+TiO_2\right]^{melt}+\left[Fe_2SiO_4\right]^{Ol}+\left[CaMgSi_2O_6-Mg_2Si_2O_6\right]^{Cpx}=\\&\left[Mg_2SiO_4-Ca_2SiO_4\right]^{Ol}+\left[CaAlAlSiO_6-CaFeAlSiO_6-CaTiAlSiO_6\right]^{Cpx}\\&+\left[MgO+FeO\right]^{melt}+\left[4CO_2\right]^{fluid}\end{aligned}\qquad(6)$$

The generalized decarbonation reaction (6) evidences that, as the degree of $CaCO_3$ assimilation increases, the contamination of magma proceeds from i) a high temperature, less oxidized domain characterized by olivine-saturated basaltic melts (Dunworth and Wilson, 1998; Wenzel et al., 2001, 2002; Hayes et al., 2015) to ii) an intermediate domain marked by olivine and clinopyroxene cosaturation (Fulignati et al., 2000, 2004; Dallai et al., 2011; Redi et al., 2017) to iii) a low temperature, highly oxidized domain governed by abundant clinopyroxene fractionation and formation of silica-poor, alkali-rich melts (Battistini et al., 2001; Gaeta et al., 2009; Di Rocco et al., 2012; Carter and Dasgupta, 2015). Therefore, reaction (6) requires that the iron speciation in the melt progressively changes under the oxidative action of CO_2, in agreement with the expression (e.g., Spandler et al., 2012):

$$[CO_2]^{fluid} + [2FeO]^{melt} = [CO]^{fluid} + [Fe_2O_3]^{melt} \quad (7)$$

In an open-system, the continuous flux of CO_2 gas through the magma shifts the equilibrium of reaction (7) to the right side, resulting in more oxidizing conditions (Connolly and Cesare, 1993). From the innermost part of the magma chamber towards the skarn shells, more oxidized magmas are produced through the redistribution of C-H-O species between melt and fluids. The progressive oxidation of magma during carbonate assimilation contributes to the destabilization of (Fe^{2+}-bearing) olivine and the crystallization of (Fe^{3+}-bearing) clinopyroxene (Wenzel et al., 2002; Gaeta et al., 2009; Del Bello et al., 2014; Mollo and Vona, 2014; Carter and Dasgupta, 2015). The stoichiometry of reaction (6) denotes as the number of MgO and FeO moles in the decarbonated magma increases through the coupled substitutions Fa ↔ Fo-Ca-ol and Di-En ↔ CaTs-CaFeTs-CaTiTs. Importantly, this exchange reaction explains also the crystallization of Al-Mg-rich spinel under more oxidized conditions (Fulignati et al., 2000, 2004; Wenzel et al., 2001, 2002; Gaeta et al., 2009; Di Rocco et al., 2012), in agreement with the CaO-rich melt inclusions found in olivine and spinel phenocrysts formed at the reaction-cumulate zone (Conte et al., 2009).

4.2. Divalent cation partitioning

Decarbonation experiments from this study provide a new dataset (Table 6S) of olivine-melt partition coefficients for Ni, Mg, Fe, Mn, and Ca applicable to primitive magmatic skarn environments. D_i^{2+} is calculated as C_i^{xls} / C_i^{melt}, where C_i^{xls} is the concentration of a chemical element *i* in the crystal and C_i^{melt} is the concentration of the same element in the melt. Despite the effects of temperature and bulk composition on D_i^{2+} are inextricably interrelated by phase relationships (e.g., Snyder and Carmichael, 1992; Libourel, 1999), D_{Ca}^{2+} and D_{Mg}^{2+} are observed to increase with increasing $CaCO_3$, whereas D_{Fe}^{2+}, D_{Mn}^{2+}, and D_{Ni}^{2+} decrease (Fig. 4). D_{Ca}^{2+}, D_{Mn}^{2+}, and D_{Ni}^{2+} are also positively correlated with ^{melt}Mg# (Fig. 4).

The $\ln D_i^{2+}$ vs. $1/T$ plot (Fig. 5a) is tentatively used to evaluate the individual effect of temperature on the partitioning behavior of divalent cations. The plot illustrates the decrease of the partition coefficient with increasing temperature (Fig. 5a), in agreement with the thermodynamic formalism describing the positive entropy of fusion of silicate minerals (Blundy and Wood, 1994; Wood and Blundy, 1997):

$$\ln D_i^{2+} = \ln\left(\gamma_i^{melt} / \gamma_i^{Ol}\right) + \left(\Delta G^{fusion} / RT\right) \quad (8)$$

Where γ_i^{melt} and γ_i^{Ol} are, respectively, the activity coefficients of the element *i* in the melt and olivine, ΔG^{fusion} is the Gibbs free energy of fusion (i.e., the difference between the free energy of melt and isochemical olivine at the temperature *T* of the system), and *R* is the universal ideal gas constant. The first term and the second term on the right of reaction (8) refer to the dependence of D_i^{2+} on the bulk composition and temperature, respectively. These terms can be parameterized through the regression analysis of experimentally-derived partition coefficients. For example, D_{Ni}^{2+} ($R^2 = 0.66$), D_{Mg}^{2+} ($R^2 = 0.86$), and D_{Fe}^{2+} ($R^2 = 0.68$) are moderately correlated with *T* (Fig. 5a), as cations with relatively small (≤ 0.78 Å) ionic radii and high ionic potentials (Hart and Davis, 1978; Leeman 1978; Takahashi, 1978; Wang and Gaetani, 2008). In contrast, D_{Mn}^{2+} ($R^2 = 0.21$) and D_{Ca}^{2+} ($R^2 = 0.41$) are weakly influenced by *T* (Fig. 5a), as cations with relatively large (≥ 0.83 Å) ionic radii and low ionic potentials (Henderson and Dale, 1968; Watson, 1977; Kohn and Schofield, 1994; Snyder and Carmichael, 1992; Libourel, 1999). Below 880 °C, Fe^{2+} tends to order onto the M1 site with increasing temperature, but it is also known that Fe^{2+} concentrates on the M2 site above 880 °C (Heinemann et al., 1999). Distortion of the M1 and M2 octahedra increases with substitution of the larger Fe^{2+} cation for Mg (Papike et al., 2005). According to the ionic size criteria, the large Ca (Coogan et al., 2005) and partially Mn (Francis and Ribbe, 1980; Henderson et al. 1996; Redfern et

al. 1996) cations have no crystal field stabilization energy in olivine, entering into the larger and more distorted M2 site. The opposite occurs for Ni, being essentially restricted to the smaller Ml site (Annersten et al., 1982; Galoisy et al., 1995). During $CaCO_3$ assimilation, the number of Ca atoms available in the melt phase increases roughly two-fold and the bulk composition shifts from ~11 to ~22 wt.% CaO (Table 2S). As a consequence, Ca is greatly incorporated into the M2 site of olivine, responding to the effect of melt chemistry rather than temperature changes (cf. Libourel, 1999). Under such circumstances, a_{CaO}^{melt} is the most effective melt compositional parameter describing the variance of D_i^{2+} (Fig. 5b). This agrees with the studies of Watson (1979) and Jurewicz and Watson (1988), denoting as D_{Ca}^{2+} can be approximated as a linear function of Ca in the melt.

4.2.1. Ca partitioning

D_{Ca}^{2+} is documented to linearly increase with decreasing Fo in olivine (Jurewicz and Watson, 1988), following the apparent relationship determined by the colinearity between *T* and Fo (Libourel, 1999). Exchange reactions for minor divalent cations involve substitutions for both Fe^{2+} and Mg in the olivine crystal structure, as expressed by the formalism of Snyder and Carmichael (1992):

$$X_{Fa}^{Ol} FeSi_{1/2}O_2^{Ol} + X_{Fo}^{Ol} MgSi_{1/2}O_2^{Ol} + M^{2+}O^{melt} = X_{Fa}^{Ol} FeO^{melt} + X_{Fo}^{Ol} MgO^{melt} + M^{2+}Si_{1/2}O_2^{Ol} \quad (9)$$

M^{2+} refers to Ca, whereas X_{Fa}^{Ol} and X_{Fo}^{Ol} indicate the mole fractions of $FeSi_{1/2}O_2^{Ol}$ and $MgSi_{1/2}O_2^{Ol}$ in olivine, respectively. The partitioning of Ca is related to a marked non-ideal substitution (Mukhopadhyay and Lindsley, 1983; Adams and Bishop, 1985), causing that the equilibrium constant of reaction (9) has both compositional and temperature dependence. From the definition of the Gibbs free energy, reaction (9) can be rearranged to quantitatively evaluate these relative contributions on D_{Ca}^{2+} (Snyder and Carmichael, 1992):

$$\ln D_{Ca}^{2+} = -11.32(\pm 1.25) + 12{,}468(\pm 2{,}332)/T(K) - 0.3478(\pm 0.255)\left[X_{Fo}^{Ol} \ln\left(X_{MgO}^{melt}/a_{Fo}^{Ol}\right) + X_{Fa}^{Ol} \ln\left(X_{FeO}^{melt}/a_{Fa}^{Ol}\right)\right] \quad (10)$$

Where a_{Fo}^{Ol} and a_{Fa}^{Ol} are the activity of Fo and Fa in olivine, respectively. When equation (10) is tested with experimental data from this study, the predicted D_{Ca}^{2+} values are affected by a very low uncertainty of $^{Eqn.(10)}$SEE = 0.02 (Fig. 1aS). The success of equation (10) with data not included in its calibration dataset highlights as models based on thermodynamic principles can be realistically extrapolated to a broad range of compositions outside of the experimental database used to formulate the activity coefficients of divalent cations (c.f. Toplis, 2005). Moreover, olivine and melt compositions from decarbonation experiments allow to isolate the effect of *T* from that of CaO produced via $CaCO_3$ assimilation. When the temperature of the system is kept constant, Ca cations into M2 crystallographic site increases with increasing CaO in the melt, causing that the number of structural sites available for Fe decreases (Fig. 1). In other words, when the influence of *T* is isolated, both Ca and Fo content in olivine increases as the melt phase becomes progressively enriched in CaO (Figs. 1 and 2). The cation-oxygen bond distance in olivine decreases from 2.17 (Fa) to 2.11 Å (Fo), implying that the incorporation of large divalent cations into crystal structure is more facilitated for Fo-rich olivines (Snyder and Carmichael, 1992 and references therein). Coherently, experimental $Fo_{87\text{-}92}$ olivines from this study are consistent with those obtained by Jurewicz and Watson (1988), showing that D_{Ca}^{2+} is a linear function of Fo content in olivine. According to Berndt et al. (2005), Fo in olivine also increases with ^{melt}Mg# over a wide range of basaltic compositions, temperature, and oxygen fugacities. Experiments from this study extend this finding to decarbonated melts, showing positive correlations between Fo, ^{melt}Mg#, and D_{Ca}^{2+} (Fig. 2). However, Toplis and Carroll (1995) have observed that the linear dependence of D_{Ca}^{2+} on Fo ceases for crystals with forsterite content lower than 55 mol%. This occurs because the activity-composition relations in olivine vary

significantly over broad chemical intervals, reflecting deviation from ideality in the forsterite-fayalite solid solution (Toplis, 2005). The close relationship between D_{Ca}^{2+} and silicate melts has been the focus of several previous works (Libourel et al., 1989; Shi and Libourel, 1991; Shi, 1993; Libourel, 1999), showing that calcium and silica in the melt phase are colinear compositional variables determining the enrichment of Ca cations in olivine. In this framework, the calcium pseudo-activity model proposed by Libourel (1999) represents a well-calibrated proxy to predict the partitioning of calcium between olivine and silicate melts reproducing a wide spectrum of natural magmatic compositions (cf. Roeder, 1974; Longhi et al., 1978; Dunn, 1987; Colson et al., 1988; Gee and Sack, 1988; Longhi and Pan, 1988; Nielsen et al., 1988; Snyder et al., 1993; Toplis and Carroll, 1995). According to this model, the effect of melt composition on Ca partitioning is described by the relationship:

$$D_{Ca}^{2+} = \left[CaO/\left(CaO+MgO\right)\right]^{Ol} / a_{CaO}^{melt} \quad (11)$$

It is worth noting that silicate melts from primitive magmatic skarn environments are subjected to important chemical modifications due to the anticorrelated effects of CaO enrichments and SiO_2 depletions (Wenzel et al., 2001, 2002). Therefore, olivine-melt compositional changes caused by the assimilation of carbonate material (i.e., open-system process) are not compatible with the CaO concentration levels of natural magmas (i.e., closed-system process). This causes that equation (11) is affected by a systematic overestimate ($^{Eqn.(11)}$SEE = 0.20) for primitive magmatic skarn compositions (Fig. 1bS). The ability prediction of equation (11) can be significantly improved ($^{Eqn.(12)}$SEE = 0.01 and $^{Eqn.(12)}R^2$ = 0.76) by simplifying the pseudo-activity parameter as follows (Fig. 1cS):

$$a_{CaO}^{melt} = X_{CaO}^{melt} / X_{SiO2}^{melt} \quad (12)$$

This result is not surprising because, according to Libourel (1999), the amount of Ca entering olivine is proportional to the number of Si and Ca atoms available in the melt structure in the form of network-former (i.e., Si-O-Si) and network-modifier (i.e., Ca-O-Si), respectively. As the melt becomes less polymerized, the number of bridging oxygens (i.e., BO, oxygens bonded to two tetrahedrally coordinated cations) decreases, whereas the amount of non-bridging oxygens (i.e., NBO, oxygens bonded to a tetrahedrally coordinated cation and to a different cation in another coordination state) increases (Kohn and Schofield, 1994; Lee and Stebbins, 2003). The melt structure is expressed as NBO/T (i.e., the number of NBO per tetrahedrally coordinated cations T; Mysen et al., 1985), whereas the different Si network connectivity in the melt is described in terms of Q^n-species (i.e., individual structure of oxygen tetrahedra surrounding a central, tetrahedrally-coordinated cation; Mysen et al., 1982). The distribution of Q^n-species in silicate melts is governed by the equilibrium reaction: $2Q^n = Q^{n-1} + Q^{n+1}$. The reaction shifts to the right as the ionic potential (Z^+/r_i^2 where Z^+ and r_i are cation charge and radius, respectively) of the network modifying cations increases (Maekawa et al., 1991). This explains why, as network modifiers, divalent alkaline earth metals ($Z^+/r_i^2 > 2$) have a more effective role in the melt structure than monovalent alkaline metals ($Z^+/r_i^2 << 2$). Cation stabilization in a polyhedron of oxygens is proportional to Z^+/r_i^2 (Watson, 1976) and, consequently, alkaline earth metals are likely also more soluble into the low-SiO_2 melt (basic melt) than high-SiO_2 melt (acidic melt). As the concentration of Ca-O-Si bonds increases during carbonate assimilation, the melt polymerization decreases according to the cation exchange (Libourel, 1999):

$$\text{Si-O-Si} + \text{Ca-O-Ca} \leftrightarrow 2\text{Ca-O-Si} \quad (13)$$

It is apparent that a_{CaO}^{melt} has a non-ideal behavior in multicomponent silicate melts, showing a non-linear correlation with X_{CaO}^{melt} (Rein and Chipman, 1965). However, the significant improvement

obtained by equation (12) indicates that the formation of Ca-O-Si bonds is energetically more favored in magmas assimilating great amounts of carbonate material. The increase of Ca cations in the melt results in i) an increase in the proportion of octahedral relative to tetrahedral sites and ii) changes of the energy of substitution of Ca in octahedral sites (cf. Leeman, 1978). Therefore, in primitive magmatic skarn systems, the combined effects of decarbonation and desilication cause that SiO_2-poor, CaO-rich melts coexist with Ca-rich olivines. In this specific scenario, the variation of D_{Ca}^{2+} can be mostly modeled as function of the number of Si and Ca atoms available in the melt structure, independently of the influence of *T* and Fo content.

4.2.2. Mg partitioning

Considering the temperature-composition relationship that governs the partitioning behavior of chemical elements, different solution of the thermodynamic equation (8) have been proposed by authors (e.g., Roeder and Emslie, 1970; Langmuir and Hanson, 1981; Ford et al., 1983; Beattie, 1993; Putirka et al., 2005, 2007; Putirka, 2008; Jones, 2016; Pu et al., 2017) to derive models predicting either D_{Mg}^{2+} or the saturation *T* of olivine. Through the statistical formula for the standardized regression coefficient (i.e., the original unstandardized regression coefficient of the independent variable, multiplied by the standard deviation of the independent variable, and divided by the standard deviation of the dependent variable), it is possible to quantify the influence of *T*, a_{CaO}^{melt} (i.e., the degree of carbonate assimilation) and MgO in the melt (i.e., the primitive character of the melt) on D_{Mg}^{2+}. Experimental data from this study show that D_{Mg}^{2+} increases by ~29% with increasing $CaCO_3$, and decreases by ~27% and ~44% with increasing *T* and X_{MgO}^{melt}, respectively. The amount of MgO in the melt is the parameter with the greatest influence on D_{Mg}^{2+}, coherently with the studies of Leeman (1978) and Kohn and Schofield (1994). However, D_{Mg}^{2+} is not (almost) univocally controlled by the isolated effect of MgO in the melt. In the recent review study of Pu et al. (2017), the olivine-melt

equations of Beattie (1993) and Putirka et al. (2007) have been recognized as the most accurate predictive models for D_{Mg}^{2+}. Pu et al. (2017) have also reappraised the general formulation of Beattie (1993) to derive a new empirical model based on the regression fit of 123 olivine-melt experiments. To test the validity of all these models under open-system decarbonation conditions, the following equations from Beattie (1993) (i.e., equation 14), Putirka et al. (2007) (i.e., equation 15), and Pu et al. (2017) (i.e., equation 16) have been considered:

$$D_{Mg}^{2+} = \left(0.666 - (0.0135X_{CaO}^{melt} - 0.049X_{MnO}^{melt} + 0.031X_{FeO}^{melt})\right) / \left(X_{MgO}^{melt} + 0.259X_{MnO}^{melt} + 0.279X_{FeO}^{melt} + 0.0056X_{CaO}^{melt}\right) \quad (14)$$

$$\ln D_{Mg}^{2+} = -2.158 + 55.09P(GPa)/T(°C) - 6.213\cdot10^{-2}X_{H2O}^{melt} + 4{,}430/T(°C) + 5.115\cdot10^{-2}\left(X_{Na2O}^{melt} + X_{K2O}^{melt}\right) \quad (15)$$

$$\ln D_{Mg}^{2+} = -4.74(\pm0.2) + 6{,}701(\pm182)/T(K) - 1.12(\pm0.08)\ln(X_{FeO}^{melt} + X_{MgO}^{melt} + X_{MnO}^{melt} + X_{CaO}^{melt} + X_{NiO}^{melt}) - 1.08(\pm0.15)\ln(X_{SiO2}^{melt}) + 0.64(\pm0.07)\left[3.5\ln(1 - X_{Al2O3}^{melt}) + 7\ln(1 - X_{TiO2}^{melt})\right] \quad (16)$$

The comparison between predicted and experimentally-derived D_{Mg}^{2+} values provides that $^{Eqn.(14)}$SEE, $^{Eqn.(15)}$SEE, and $^{Eqn.(16)}$SEE are 1.73 (Fig. 2aS), 0.96 (Fig. 2bS), and 1.27 (Fig. 2cS), respectively. Equation (14) of Beattie (1993) and equation (16) of Pu et al. (2017) include regression parameters for the melt (i.e., X_{Ca}^{melt} and X_{SiO2}^{melt}) that are greatly influenced by magma decarbonation and desilication phenomena, thus lowering their ability predictions under open-system conditions. Mg is undoubtedly the major component of magmatic olivines and, as evidenced by the decarbonation reaction (6), its concentration increases with Ca content. For the case of Colli Albani Volcanic Complex (Italy), natural olivines from endoskarns are systematically enriched in Fo and CaO with respect to those from uncontaminated magmas (Gaeta et al., 2009; Di Rocco et al., 2014). The same

geochemical trend has been observed for xenoliths from several eruptions of Vesuvius (Italy; Dallai et al., 2011; Hayes et al., 2015; Jolis et al., 2015; Redi et al., 2017) and dunite cumulates from the Ioko-Dovyren Intrusion (North Baikal, Russia; Wenzel et al., 2001, 2002). On this basis, the values of D_{Mg}^{2+} experimentally-derived from this study can be parameterized as a function of a_{CaO}^{melt}, T, and X_{MgO}^{melt}, as follows (cf. Putirka et al., 2007):

$$\begin{aligned}\ln D_{Mg}^{2+} &= 0.03(\pm 0.02) a_{CaO}^{melt} + 0.110(\pm 0.03)\cdot 10^4 / T(K) \\ &\quad - 6.97(\pm 0.42) X_{MgO}^{melt} + 1.93(\pm 0.23)\end{aligned} \tag{17}$$

Within the temperature-composition space of carbonate-bearing basaltic magmas (Fig. 2dS), D_{Mg}^{2+} variations are successfully described by equation (17), providing good regression statistics of $^{Eqn.(17)}R^2 = 0.99$ and $^{Eqn.(17)}SEE = 0.01$.

4.2.3. Fe partitioning

Thermodynamic modeling of olivine-basalt compositions have evidenced that the partitioning of Fe^{2+} is linearly dependent of D_{Mg}^{2+}, but independent of P and T (Jones, 1984, 2016). According to the observation that i) the stoichiometry of olivine is relatively simple, ii) Mg and Fe^{2+} totally dominate all other divalent cations, and iii) the partitioning of transition metals is greatly controlled by heats of fusion rather than heats of mixing for ideal melt and crystal solutions, Jones (2016) (i.e., equation 18) and Wang and Gaetani (2008) (i.e., equation 19) proposed the following regression fits:

$$D_{Fe}^{2+}(\pm 0.13) = 0.298 D_{Mg}^{2+} + 0.027 \tag{18}$$

$$\ln D_{Fe}^{2+} = 1.15(\pm 0.04) \ln D_{Mg}^{2+} + 0.64(\pm 0.06) \tag{19}$$

The application of these linear models to olivine-melt pairs from uncontaminated basaltic experiments yields errors ($^{Eqn.(18)}$SEE = 0.23 and $^{Eqn.(19)}$SEE = 0.10) that are quite similar to the intrinsic calibration errors calculated by Jones (2016) and Wang and Gaetani (2008). In contrast, equations (18) and (19) show systematic overestimates ($^{Eqn.(18)}$SEE = 0.52 and $^{Eqn.(19)}$SEE = 0.30) for olivine-melt pairs from decarbonation experiments (Figs. 3a-bS). It is interesting to note that D_{Fe}^{2+} varies approximately by ~14%, ~37%, and ~49% as a function of T, X_{MgO}^{melt}, and $CaCO_3$, respectively. According to reaction (10), the thermodynamics of olivine mixing requires that Ca substitutes for both Fe^{2+} and Mg in the crystal lattice during magma-carbonate interaction. This is consistent with the study of Jurewicz and Watson (1988) attesting that the concentration of calcium in olivine is highly correlated with iron in both crystal and melt. Due to differences between Fe^{2+} and Mg cation radii, the Ca-Fe^{2+} substitutions in olivine are more facilitated than Ca-Mg ones, as the amount of Ca cations in the melt increases (Warner and Luth, 1973; Adams and Bishop, 1985). In this view, the equation (18) of Jones (2016) can be refined by considering the influence of the activity of calcium in the melt:

$$D_{Fe}^{2+} = 0.11(\pm 0.01) - 0.46(\pm 0.04) D_{Mg}^{2+} - 0.13(\pm 0.05) a_{CaO}^{melt} \quad (20)$$

The regression fit of equation (20) is greatly improved ($^{Eqn.(20)}R^2$ = 0.92 and $^{Eqn.(20)}$SEE = 0.03; Fig. 3cS), pointing out that the linear relationship between D_{Fe}^{2+} and D_{Mg}^{2+} cannot be assumed as independent on melt composition under open-system conditions. According to the exchange reaction (13), the melt polymerization decreases as the concentration of Ca-O-Si bonds increases (Shi and Libourel, 1991; Libourel, 1999), thus influencing the proportion of octahedral relative to tetrahedral sites and, ultimately, the activity of the chemical species in the melt (Mysen, 2004). The increasing amount of Ca cations in the melt enhances the breaking of Si−O−Si bonds and reduces the number

of NBO necessary for the network-modifying cations to form their preferred coordination polyhedra. In other words, the disruption of tetrahedral units by Ca cations increases the number of structural sites critically important to accommodating network-modifying cations in the melt structure (i.e., Fe^{2+}, Mn, and Ni), lowering the value of D_i^{2+}. Several experimental studies (e.g., Mysen and Virgo, 1980; Mysen et al., 1982; Kushiro and Mysen, 2002; Gaetani, 2004; Mysen, 2004; Mysen and Dubinsky, 2004; Li and Ripley, 2010; Wang and Gaetani, 2008) have demonstrated that D_i^{2+} for network-modifying cations varies as a function of NBO/T. The solubility of network-modifying cations in silicate melts decreases as the activity of NBO decreases with increasing silica content (Mysen, 2004), so that divalent cations are preferentially incorporated into olivine crystal lattice (e.g., Libourel, 1999). Log-linear relations between D_i^{2+} and NBO/T exhibit more negative slopes with increasing the valence cation due to an increased availability of NBO to form the metal-oxygen polyhedra (Walter and Thibault, 1995; Jana and Walker, 1997; Jaeger and Drake, 2000). More specifically, steric hindrance leads to the cation with the highest ionic potential (Ni >Mg >Fe^{2+} >Mn >Ca) to form bonds with oxygen in the less polymerized Q^n-species (Mysen and Dubinsky, 2004). Following these principles, Wang and Gaetani (2008) rearranged the thermodynamically-based equation of Beattie et al. (1991) in the form:

$$\ln D_{Fe}^{2+} = -0.51(\pm 0.02)\ln(NBO/T) + 6{,}000(\pm 400)/T(K) - 3.8(\pm 0.4) \qquad (21)$$

Noteworthy, the values of D_{Fe}^{2+} predicted by equation (21) match quite well ($^{Eqn.(21)}$SEE = 0.25) with those measured from magma-carbonate interaction experiments (Fig. 3dS). According to Wang and Gaetani (2008), the partitioning of Fe^{2+} decreases with melt depolymerization (i.e., with $CaCO_3$ assimilation; Fig. 3dS) due to the enhanced disorder in the melt structure and the reduced occupancy of octahedral sites by divalent cations (Leeman, 1978). These latter are bonded to energetically non-equivalent NBO, so that the bond strength between Si and NBO depends on the number of BO in the

different Q^n-species (Mysen, 2004). Therefore, D_{Fe}^{2+} in the equation (21) is non-linear function of NBO/T because of the different i) solution mechanisms of network-modifying cations, ii) activity-composition relations of chemical elements in decarbonated melts, and iii) types of NBO available in the coexisting Q^n-species (Mysen, 2004).

4.2.4. Mn partitioning

Since the study of Watson (1977), silicate melts have been considered as complex atomic structures that, together with the saturation temperature of olivine, govern the partitioning behavior of Mn. However, D_{Mn}^{2+} is more dependent on melt composition and structure rather than temperature (Watson, 1977). The same conclusion was reached by Kohn and Schofield (1994) for the simplified Fo-Ab-An system in which small changes in NBO/T are accompanied by large D_{Mn}^{2+} variations in highly depolymerized melts, but the effect of changing temperature by 100 °C is too small to be observable. Wang and Gaetani (2008) proposed a thermodynamically-based expression to quantify D_{Mn}^{2+} as a function of both melt composition and temperature:

$$\ln D_{Mn}^{2+} = -0.41(\pm 0.06)\ln(NBO/T) + 6{,}100(\pm 1{,}500)/T(K) - 4.0(\pm 0.9) \quad (22)$$

Equation (22) is applicable to a relatively broad range of melt compositions in equilibrium with primitive olivines that, importantly, are compositionally similar to those ($Fo_{87\text{-}93}$) from this study. However, D_{Mn}^{2+} values predicted by equation (22) are underestimated ($^{Eqn.(22)}SEE = 0.54$) relative to those measured for olivine-melt pairs from decarbonation experiments (Fig. 4aS). D_{Mn}^{2+} progressively decreases with increasing $CaCO_3$ due to the lower chemical potential of Mn, as the number of NBO increases in the more depolymerized melt (Fig. 4aS). Note that steric hindrance effects are more operative in CaO-rich melts, making not possible to satisfy the bonding requirements for Mn without

distorting and destabilizing the silicate framework (Kohn and Schofield, 1994). Although the magnitude of the partition coefficient scales with the degree of melt polymerization, the melt structure affects significantly the element partitioning when NBO/T is lower than a certain threshold value. For example, complementary results from Gaetani (2004), Huang et al. (2006), and Mollo et al. (2016) denote that the partitioning of REE between clinopyroxene and silicate melt increases markedly below a NBO/T equals to 0.4. Turning to the case of olivine, Schmidt et al. (2006) and Wang and Gaetani (2008) reported that the dependence of divalent cation partitioning on melt composition becomes negligible at NBO/T >0.6. The review study of Bédard (2005) reports a compilation of olivine-melt partition coefficients from both experimental and natural products analyzed over a span of 25 years. The D_{Mn}^{2+} vs. NBO/T diagram (Fig. 6) shows a monotonic increase of the partition coefficients from ~0.4 to ~4.1, as NBO/T decreases from ~1.8 to ~0.3. D_{Mn}^{2+} values from decarbonation experiments are consistent with those from Bédard (2005), aligning along a trend with a steeper slope at NBO/T <0.6 (Fig. 6). At higher NBO/T, the polymeric units become completely dissociated and the number of BO decreases (Fig. 6). The change of D_{Mn}^{2+} reflects the combined effects of temperature, crystal chemistry, and melt structure (e.g., Bédard, 2005; Wang and Gaetani, 2008). In fact, if the number of Ca cations in the melt affects the activity of Mn (Kohn and Schofield, 1994), it is also true that an increasing $CaMgSiO_4$ component in olivine changes the standard free energy of Mn in the crystal lattice (Takahashi, 1978). Mn and Ca cations reside in the same M2 crystallographic site and, therefore, the presence of one will to some degree affects the incorporation of the other, causing that D_{Mn}^{2+} decreases with increasing Ca into olivine (Lumpkin et al., 1983; Annersten et al., 1984; Akamatsu et al., 1988; Snyder and Carmichael, 1992). On this basis, the equation (22) of Wang and Gaetani (2008) can be refined for decarbonated magmas by including the X_{Ca}^{Ol} term:

$$\ln D_{Mn}^{2+} = -0.41(\pm 0.11)\ln(NBO/T) + 65.39(\pm 25.18)/T(K) - 0.42(\pm 0.07)X_{CaO}^{Ol} + 0.41(\pm 0.07) \quad (23)$$

As a result, the regression statistics ($^{Eqn.(23)}R^2$ = 0.92 and $^{Eqn.(23)}$SEE = 0.03) of equation (23) are remarkably improved. Therefore, for primitive magmatic skarn melts with NBO/T >0.6, Mn partitioning systematics can be more precisely quantified taking into account the control of both crystal and melt compositions (Fig. 4bS).

4.2.5. Ni partitioning

The temperature dependence of Ni-Mg exchange reaction is strictly related to the difference in the enthalpy of fusion between Mg_2SiO_4 and Ni_2SiO_4 components in olivine (Jones, 2016). At a given bulk composition, D_{Ni}^{2+} is observed to decrease with *P* and *T* (Matzen et al., 2013, 2017; Ammannati et al., 2016). On the contrary, during magma cooling and crystallization, most of D_{Ni}^{2+} changes are the effect of covarying temperature and melt composition (Watson, 1977; Hart and Davis, 1978; Lynn et al., 2017). Since Ca and Ni are strongly ordered and reside in different olivine crystallographic sites, D_{Ni}^{2+} and D_{Ca}^{2+} are found to be independent of X_{CaO}^{Ol} and X_{NiO}^{Ol}, respectively. According to the exchange equation (10), Snyder and Carmichael (1992) modeled the variation of D_{Ni}^{2+} through the thermodynamic solution:

$$\ln D_{Ni}^{2+} = -2.575(\pm 0.484) + 4{,}592(\pm 724)/T(K)\left[X_{Fo}^{Ol}\ln\left(X_{MgO}^{melt}/a_{Fo}^{Ol}\right) + X_{Fa}^{Ol}\ln\left(X_{FeO}^{melt}/a_{Fa}^{Ol}\right)\right] \quad (24)$$

Decarbonated data from this study are not adequately described ($^{Eqn.(24)}$SEE = 3.62; Fig. 5aS) by equation (24), suggesting that D_{Ni}^{2+} cannot be univocally addressed to the temperature-dependence exchange between Ni and Mg (cf. Snyder and Carmichael, 1992). For example, the broad range of

Ni contents measured in natural olivines is caused by the marked variations of MgO and SiO_2 in the melt during crystallization (e.g., Irvine and Kushiro, 1976; Hart and Davis, 1978; Takahashi, 1978; Jones, 1984; Clague et al., 1991; Korenaga and Kelemen, 2000; Sobolev et al., 2005, 2007; Putirka et al., 2011; Matzen et al., 2013; Ammannati et al., 2016; Lynn et al., 2017). Moreover, among all divalent cations, Ni has the highest crystal field stabilization energy in octahedral sites (~29.2 kcal/mol; Dunitz and Orgel, 1957). Consequently, as the value of NBO/T decreases (i.e., the number of NBO to form coordination polyhedra decreases), Ni is preferentially incorporated into olivine crystal lattice relative to Mg (Henderson and Dale, 1968; Irvine and Kushiro, 1976; Watson, 1977; Takahashi, 1978). The variation of D_{Ni}^{2+} with NBO/T has been modeled by Wang and Gaetani (2008) through the expression:

$$\ln D_{Ni}^{2+} = -0.71(\pm 0.04)\ln(NBO/T) + 7{,}100(\pm 900)/T(K) - 2.5(\pm 0.6) \quad (25)$$

Although equation (25) has been calibrated specifically to siliceous eclogite partial melts or basalts, its predictive power ($^{Eqn.(25)}$SEE = 1.86; Fig. 5bS) for decarbonated compositions is apparently better than that of the activity-based equation (24). Noteworthy, Ca cations form NBO bonds less sterically hindered and energetically more favored than divalent cations with smaller ionic radii and higher ionic potentials, such as Ni (e.g., Kohn and Schofield, 1994; Mysen and Dubinsky, 2004; Mysen and Richet, 2005). Therefore, during $CaCO_3$ assimilation, the depolymerizing effect of Ca reduces the steric distortion of Ni octahedra in the melt (cf. Keppler, 1992; Keppler and Bagdassarov, 1999; Mysen and Dubinsky, 2004; Jackson et al., 2005; Mysen, 2006, 2008; Wang and Gaetani, 2008; Li and Ripley, 2010) by enhancing cation solubility and lowering D_{Ni}^{2+} (Takahashi, 1978; Mysen and Virgo, 1980; Libourel, 1999; Schmidt et al., 2006; Mysen, 2007, 2008; Wang and Gaetani, 2008). In the review study of Pu et al. (2017), a set of melt components is used to describe the degree of

depolymerization (also in agreement with the early studies of Beattie et al., 1991 and Beattie, 1993), in order to derive the following model for D_{Ni}^{2+}:

$$\begin{aligned}\ln D_{Ni}^{2+} = {} & -4.32(\pm 0.33) + 9{,}416(\pm 296)/T(K) - 0.71(\pm 0.13) \\ & \ln(X_{FeO}^{melt} + X_{MgO}^{melt} + X_{MnO}^{melt} + X_{CaO}^{melt} + X_{NiO}^{melt}) + 0.53(\pm 0.24) \\ & \ln(X_{SiO2}^{melt}) + 0.35(\pm 0.11)\left[3.5\ln(1 - X_{Al2O3}^{melt}) + 7\ln(1 - X_{TiO2}^{melt})\right]\end{aligned} \quad (26)$$

It is interesting to note that the parameterization of equation (26) makes the model very suitable for basaltic melts assimilating carbonate material, yielding $^{Eqn.(26)}$SEE = 1.54 (Fig. 5cS). This outcome is a clear evidence that the partitioning behavior of Ni is independent of olivine chemistry, as the direct consequence of the control exerted by melt composition and structure on cations with high ionic potentials (Gaetani 2004; Schmidt et al. 2006; Wang and Gaetani, 2008).

4.3. Cation exchange reactions

Cation redistribution reactions based on the equilibrium between olivine and melt are generally expressed by the exchange partition coefficient, $K_{D(i-j)} = \left(X_i^{Ol} / X_j^{Ol}\right)/\left(X_i^{melt} / X_j^{melt}\right)$, where *i* and *j* refer to the two chemical elements of interest. Roeder and Emslie (1970) argued that, under equilibrium conditions, $K_{D(Fe-Mg)}$ exhibits an approximately constant mean value of 0.30 (±0.03), irrespective of temperature, melt redox state, and bulk composition. Although this approach is used as an evidence of equilibrium in both natural and experimental systems, it is also know that $K_{D(Fe-Mg)}$ changes systematically from 0.13 to 0.45, responding to the variable physicochemical state of the crystallizing system (e.g., Longhi et al., 1978; Takahashi, 1978; Ford et al., 1983; Jones, 1984; Gee and Sack 1988; Herzberg and O'Hara 1998; Kushiro and Walter, 1998; Kushiro and Mysen, 2002; Toplis 2005; Mibe et al., 2006; Filiberto and Dasgupta, 2011; Putirka, 2016; Mollo and Hammer, 2017). The melt composition and structure have a great influence on the Fe^{2+}-Mg exchange, especially

for the effect of $Na_2O + K_2O$ (e.g., Sack et al., 1987; Gee and Sack, 1988; Toplis, 2005), TiO_2 (e.g., Jones, 1988; Wagner and Grove, 1997), SiO_2 (e.g., Longhi et al., 1978; Toplis, 2005), and NBO/T (e.g., Kushiro and Walter, 1998; Kushiro and Mysen, 2002; Mibe et al., 2006; Filiberto and Dasgupta, 2011). Bearing this in mind, Putirka (2016) has recently performed the global regression analysis of 1,270 experimental data from literature, finding that olivine crystals in equilibrium with both terrestrial and extraterrestrial magmas provide a mean Fe^{2+}-Mg exchange value of 0.33 (±0.04). In this respect, magma-carbonate interaction data from this study show that $K_{D(Fe-Mg)}$ narrowly changes from 0.29 to 0.36 (Table 7S), as a clear evidence of equilibrium crystallization of olivines from the decarbonated melts (cf. Bickle et al., 1977; Filiberto and Dasgupta, 2011; Matzen et al., 2011; Barr and Grove, 2013). As a further test of equilibrium, the measured $K_{D(Fe-Mg)}$ values have been compared with those predicted by the models of Toplis (2005) (i.e., equation 27) and Putirka (2016) (i.e., equations 28 and 29):

$$K_{D(Fe-Mg)} = \exp\left\{\left[\frac{-6766}{RT(K)} - \frac{7.34}{R}\right] + \ln\left[0.036\%X_{SiO2}^{melt}\#-0.22\right] + \left[\frac{3{,}000\left(1-2X_{Fo}^{Ol}\right)}{RT(K)}\right] + \left[\frac{0.035\left(P(bar)-1\right)}{RT(K)}\right]\right\} \quad (27)$$

$$K_{D(Fe-Mg)} = 0.25 + 0.0018SiO_2 - 3.27\cdot10^{-4}\left(Na_2O + K_2O\right)^2 \quad (28)$$

$$K_{D(Fe-Mg)} = 0.0583 + 0.00252SiO_2 + 0.028P(GPa) - 0.0091\left(Na_2O + K_2O\right) - 0.013383\log(fO_2) \quad (29)$$

The $\%X_{SiO2}^{melt}\#$ parameter of equation (27) refers to the molar silica content of the melt recalculated according to Toplis (2005). Notably, the equation (29) of Putirka (2016) treats all iron in the melt as

FeO_t, referring to a mean equilibrium value of Fe^{2+}-Mg exchange close to 0.29 (±0.051). For the present decarbonation experiments, equations (27), (28), and (29) evidence equilibrium olivine crystallization, yielding $K_{D(Fe-Mg)}$ values of 0.26-0.30, 0.32-0.34, and 0.23-0.27, respectively (Fig. 6S). The standard error of estimates ($^{Eqn.(27)}$SEE = 0.04, $^{Eqn.(28)}$SEE = 0.02, and $^{Eqn.(29)}$SEE = 0.02) are also very similar to the intrinsic calibration errors ($^{Eqn.(27)}$SEE = 0.03, $^{Eqn.(28)}$SEE = 0.04, and $^{Eqn.(29)}$SEE = 0.04) of the models. With increasing $CaCO_3$ assimilation, D_{Fe}^{2+} decreases from ~5% to ~13%, whereas D_{Mg}^{2+} increases from ~3% to ~5% (Fig. 4). The maximum deviation between D_{Fe}^{2+} and D_{Mg}^{2+} is calculated for basalts doped with 20 wt.% $CaCO_3$. However, $CaCO_3$ assimilation does not affect significantly the D_{Fe}^{2+}/D_{Mg}^{2+} ratio, implying that the value of $K_{D(Fe-Mg)}$ increases only slightly. It is therefore concluded that the Fe^{2+}-Mg exchange reaction between olivine and decarbonated melt is not perfectly invariant with $K_{D(Fe-Mg)}$ ranging from 0.29 to 0.35, but the mean value of $K_{D(Fe-Mg)}$ equally tends towards the equilibrium condition of 0.33±0.04 established for terrestrial and extraterrestrial magmas (cf. Putirka, 2016).

According to Mysen (2008), the exchange reaction between Fe^{2+}/Ca/Mn/Ni and Mg quantitatively describes the equilibrium state of two cations with different electronic properties (e.g., ionic potentials) and different affinities for energetically non-equivalent NBO in Q^n-species. Fig. 7 shows that these exchange partition coefficients do not vary significantly with T and ^{melt}Mg#, responding to a restricted NBO/T change with maximum deviation of only ~16% (see also Table 7S). In contrast, important NBO/T changes are observed with increasing $CaCO_3$ (Fig. 7), showing maximum deviation of ~64%. The role of the melt structure has been broadly emphasized in literature as one of the most striking parameter determining $K_{D(Fe-Mg)}$ fluctuations (e.g., Kushiro and Walter, 1998; Kushiro and Mysen, 2002; Toplis, 2005; Mibe et al., 2006; Filiberto and Dasgupta, 2011). During cation partitioning between olivine and mafic melts, $K_{D(Fe-Mg)}$ increases with increasing NBO/T, and then decreases with further NBO/T increase (Fig. 8a). Such behavior depends on the

relative proportions of four-, five-, and six-coordinated Mg and Fe^{2+} cations in the melt (Kushiro and Walter, 1998; Kushiro and Mysen, 2002). In the last decades, three different second order polynomial curves have been regressed by authors for mafic terrestrial (Kushiro and Walter, 1998; Mibe et al., 2006) and Martian (Filiberto and Dasgupta, 2011) basalts. These curves are characterized by a maximum value of $K_{D(Fe-Mg)}$ at NBO/T of ~1.5-2 (Fig. 8a). The Fe^{2+}-Mg exchanges from decarbonation experiments deviate from the modeled parabolas at NBO/T >0.9, when the amount of $CaCO_3$ assimilated by melts is 20 wt.% (Fig. 8a). Despite the value of $K_{D(Fe-Mg)}$ decreases slightly with increasing CaO in the melt, the corresponding value of NBO/T increases remarkably (Fig. 8a). This behavior supports the finding that i) the effect of Ca on melt structure is much more influencing than T and ^{melt}Mg#, ii) the value of NBO/T does not account for the dominant type of network-modifying cations and the structural changes in the melt (i.e., coordination number, ionic potential, steric hindrance, and distortion of the polyhedra), and iii) the number of Ca-Fe^{2+} substitutions in olivine M2 site is bounded by the larger Ca cations relative to the smaller Fe^{2+} ones.

The geometry of M2 octahedral site and the cation size are limiting factors for the partitioning of divalent cations between olivine and melt, leading to a marked non-ideal Ca-Mg substitution (Adams and Bishop, 1985; Davidson and Mukhopadhyay, 1984; Mukhopadhyay and Lindsley, 1983; Warner and Luth, 1973; Snyder and Carmichael, 1992). Consequently, $K_{D(Ca-Mg)}$ varies in a narrow range of ~0.008-0.015, as the degree of $CaCO_3$ assimilation increases by up to 20 wt.% (Fig. 7). Moreover, the positive correlation between $K_{D(Ca-Mg)}$ and NBO/T (Fig. 8b) confirms the control of the melt structure on the cation exchange reaction. The same conclusion applies to $K_{D(Mn-Mg)}$ (Fig. 8c) and $K_{D(Ni-Mg)}$ (Fig. 8d) showing minimum values at NBO/T of ~1.5, in agreement with those found for highly depolymerized basaltic melts (Mysen, 2006). The variation of $K_{D(Ni-Mg)}$ may be addressed to either the influence of the melt structure on the solubility of Ni cations (Irvine and Kushiro, 1976; Takahashi, 1978), or the temperature dependence of the Ni-Mg exchange reaction

(Matzen et al., 2013). $K_{D(Mn-Mg)}$ shows little variations with temperature (Kohn and Schofield, 1994), being mostly controlled by the effect of $CaCO_3$ assimilation (Fig. 7). This reflects the higher number of NBO coordinating Mn cations as the amount of CaO in the melt increases (Watson, 1977). Furthermore, Mn and Ca compete for the same M2 site in olivine (Fig. 1) and, consequently, less octahedral crystallographic sites are available for Mn cations during magma-carbonate interaction (Takahashi, 1978; Kohn and Schofield, 1994). It is interesting to note that the value of NBO/T does not greatly scales with ^{melt}Mg# (Fig. 8), due to an almost equal substitution between Fe^{2+} and Mg as network-modifying cations with comparable ionic potentials. Thus, the value of $K_{D(Fe-Mg)}$ is observed to weakly increase when ^{melt}Mg# decreases from 78 to 72 (Fig. 8a). In contrast, at a given NBO/T value, $K_{D(Ca-Mg)}$ (Fig. 8b), $K_{D(Mn-Mg)}$ (Fig. 8c), and $K_{D(Ni-Mg)}$ (Fig. 8d) decrease remarkably with decreasing ^{melt}Mg# or, alternatively, with increasing D_{Mg}^{2+} (Fig. 4). This demonstrates that the effect of Mg on the exchange partition coefficient is always subordinate to that of Ca, accounting for the following considerations: i) the content of MgO in the melt changes by only ~20%, whereas CaO increases markedly by ~50% and ii) the depolymerizing effect of Ca in the melt is always greater than that of Mg because Mg-NBO bonds are sterically more hindered and less energetically favored than Ca-NBO bonds (Mysen, 2008).

4.4. Applications to the primitive magmatic skarns of the Colli Albani Volcanic District

The Colli Albani Volcanic District (CAVD) is located close to the city of Rome (Italy) and is one of the main volcanic settings belonging to the ultrapotassic Roman Province (e.g., Freda et al., 2008). The eruptive products at CAVD testify to complex contamination reactions due to the emplacement of magmas within a thick carbonate sequence localized at ~2 km depth (Freda et al., 2008 and references therein). In particular, lithic clasts in pyroclastic deposits have been recognized as cumulates and skarns (either endoskarns or exoskarns) representing the rock compositional heterogeneity at the magma-carbonate interface (e.g., Gaeta et al., 2009; Di Rocco et al., 2012). The

paragenesis of lithic clasts is dominated by olivine and clinopyroxene, with mineral compositions and proportions variable as a function of the degree of carbonate assimilation. The NiO vs. Fo diagram (Fig. 9a) displays the chemical changes of olivine phenocrysts found in cumulates and endoskarns at CAVD (data from Gaeta et al., 2009 and Di Rocco et al., 2012). Olivine phenocrysts from cumulates are less influenced by the effect of carbonate assimilation, showing that NiO and Fo contents decrease along a prevailing crystal fractionation path (Fig. 9a). In contrast, the composition of olivines from endoskarns is greatly controlled by the degree of carbonate assimilation, leading to the formation of NiO-poor, Fo-CaO-rich phenocrysts. Results from $^{melt}Mg\#_{78}$ decarbonation experiments confirm that Ni is less efficiently incorporated in the olivine crystal lattice, as the amount of carbonate assimilated increases from 0 to 10 to 20 wt.% (Fig. 9a). Intriguingly, natural $Fo_{94\text{-}97}$ olivines with extremely low Ni contents are not captured in full by the experimental path. These phenocrysts are found in CaO-rich endoskarns grading to the exoskarn domain close to the carbonate wall-rocks (Di Rocco et al., 2012). Therefore, $Fo_{94\text{-}97}$ olivines are the product of higher degrees of carbonate assimilation at the magma-carbonate interface (cf. Conte et al., 2009; Mollo et al., 2010, 2013a; Mollo and Vona, 2014) where calcite dissolution and magma contamination phenomena are more effective (Carter and Dasgupta, 2015, 2016). The Ni vs. CaO diagram (Fig. 9b) shows the contamination path of melt inclusions entrapped in the same olivine phenocrysts from cumulates and endoskarns (data from Gaeta et al., 2009 and Di Rocco et al., 2012). Ni is negatively correlated with CaO due to early fractionation of olivine (Gaeta et al., 2009) and dilution of the contaminated magma by carbonate assimilation (Carter and Dasgupta, 2016). The melt inclusion with the highest Ni and lowest CaO contents is used as starting composition to track the combined effects of assimilation and fractional crystallization (AFC). Olivine-melt partition coefficients of Ca (D_{Ca}^{2+} = 0.15) and Ni (D_{Ni}^{2+} = 11.22) are estimated through Eqns. 11 and 26, respectively. The CaO content of the assimilant is set to 45 wt.%, corresponding to the thermal decomposition of $CaCO_3$ (Mollo et al., 2013a). The amount of fractionated olivine is lower than 8% and the ratio of the assimilation rate to the crystallization rate changes from 0.01 to 0.2, in order to reproduce variable degrees of carbonate assimilation. Modeling

results confirm that cumulates at CAVD are less affected by magma-carbonate interaction (Fig. 9b) and are produced by degrees of carbonate assimilation lower than 6% (cf. Gaeta et al., 2009; Di Rocco et al., 2012). Conversely, the geochemical signature of endoskarns accounts for stronger carbonate assimilation effects (Fig. 9b), in agreement with previous AFC calculations conducted by Di Rocco et al. (2012) using trace element and isotope data of cumulate and endoskarn rocks.

5. Summary and conclusions

Magma-carbonate interaction experiments from this study have been designed to better understand the chemical variation of olivine in primitive magmatic skarn environments, as well as to resolve the influence of temperature and bulk composition on the partitioning behavior of divalent cations between olivine crystals and decarbonated melts. Considering the wide spectrum of partitioning models reported in literature, some predictive equations can be refined to better quantify the effect of carbonate assimilation. Through this approach, the following conclusions can be drawn:

1) the crystallization of Fo-CaO-rich, NiO-poor olivines is more favored at higher temperatures when primitive basaltic melts assimilate up to 20 wt.% of carbonate material;
2) under such open-system conditions, the amount of Ca entering olivine crystal lattice is proportional to the number of Ca-O-Si bonds available in the melt structure;
3) the partitioning behavior of divalent cations between olivine and melt changes as a function of temperature, crystal composition, and melt structure. As the degree of $CaCO_3$ assimilation increases, D_{Ca}^{2+} and D_{Mg}^{2+} increase, whereas D_{Fe}^{2+}, D_{Mn}^{2+}, and D_{Ni}^{2+} decrease;
4) D_{Ca}^{2+} is prevalently controlled by CaO and MgO contents in olivine, as well as the activity of calcium in the melt (a_{CaO}^{melt});
5) D_{Mg}^{2+} is parameterized as function of a_{CaO}^{melt}, T, and MgO in the melt;

6) D_{Fe}^{2+} is a linear function of both D_{Mg}^{2+} and a_{CaO}^{melt}. Nevertheless, a log-linear relationship between D_{Fe}^{2+} and the number of non-bridging oxygens per tetrahedrally coordinated cations is also found, testifying to the primary effect of Ca on the melt structure;
7) D_{Mn}^{2+} changes responding either to the higher energy state of Mn cations in more depolymerized melts, or the progressive increase of Ca cations in the olivine M2 site;
8) D_{Ni}^{2+} is independent of olivine composition due to the fact that its value is practically controlled by the degree of melt polymerization;
9) the exchange partition coefficients between Fe^{2+}/Ca/Mn/Ni and Mg do not vary significantly as a function of T and ^{melt}Mg#. The melt structure primarily controls the values of the exchange partition coefficients;
10) $K_{D(Fe-Mg)}$ is not perfectly invariant with increasing $CaCO_3$ assimilation. Despite little fluctuations, the mean value of the Fe^{2+}-Mg exchange invariably approaches to the equilibrium condition of 0.33±0.04;
11) the comparison between natural data from cumulates and endoskarns at the Colli Albani Volcanic District (Italy) and those experimentally-derived in this study indicates that the geochemical signature of olivine phenocrysts and their melt inclusions is strictly controlled by the degree of carbonate assimilation.

Acknowledgments

The preliminary version of this study benefited from insightful and valuable comments of Keith Putirka. Thanks go to Marcel Guillong for his support with laser ablation analyses.

References

Adams, G.E., Bishop, F.C., 1986. The olivine—clinopyroxene geobarometer: experimental results in the CaO-FeO-MgO-SiO_2 system. Contrib. to Mineral. Petrol. 94, 230-237

Adams, G.E., Bishop, F.C., 1985. An experimental investigation of thermodynamic mixing properties and unit-cell parameters of forsterite-monticellite solid solution. Am. Mineral. 70, 714-722

Akamatsu, T., Fujino, K., Kumazawa, M., Fujimura, A., Kato, M., Sawamoto, H., Yamanaka, T., 1988. Pressure and temperature dependence of cation distribution in Mg-Mn olivine. Phys. Chem. Miner. 16, 105-113

Ammannati, E., Jacob, D.E., Avanzinelli, R., Foley, S.F., Conticelli, S., 2016. Low Ni olivine in silica-undersaturated ultrapotassic igneous rocks as evidence for carbonate metasomatism in the mantle. Earth Planet. Sci. Lett. 444, 64-74

Annersten, H., Ericsson, T., Filippidis, A., 1982. Cation Ordering in Ni-Fe Olivines. Am. Mineral. 67, 1212-1217

Barnes, C.G., Prestvik, T., Sundvoll, B., Surratt, D., 2005. Pervasive assimilation of carbonate and silicate rocks in the Hortavær igneous complex, north-central Norway. Lithos 80, 179-199

Barr, J.A., Grove, T.L., 2013. Experimental petrology of the Apollo 15 group A green glasses: Melting primordial lunar mantle and magma ocean cumulate assimilation. Geochim. Cosmochim. Acta 106, 216-230

Beattie, P., 1993. Olivine-melt and orthopyroxene-melt equilibria. Contrib. to Mineral. Petrol. 115, 103-111

Beattie, P., Ford, C., Russell, D., 1991. Partition coefficients for olivine-melt and orthopyroxene-melt systems. Contrib. to Mineral. Petrol. 109, 212-224

Bédard, J.H., 2005. Partitioning coefficients between olivine and silicate melts. Lithos 83, 394-419

Berndt, J., Koepke, J., Holtz, F., 2005. An experimental investigation of the influence of water and oxygen fugacity on differentiation of MORB at 200 MPa. J. Petrol. 46, 135-167

Bickle, M.J., Ford, C.E., Nisbet, E.G., 1977. The petrogenesis of peridotitic komatiites: evidence from high-pressure melting experiments. Earth Planet. Sci. Lett. 37, 97-106

Blundy, J.D., Wood, B.J., 1994. Prediction of crystal-melt partition coefficients from elastic moduli. Nature 372, 452-454

Bottinga, Y., Weill, D.F., Richet, P., 1981. Thermodynamic modeling of silicate melts. In Thermodynamics of minerals and melts Springer, New York, NY, pp. 207-245

Carter, L.B., Dasgupta, R., 2016. Effect of melt composition on crustal carbonate assimilation - Implications for the transition from calcite consumption to skarnification and associated CO_2 degassing. Geochem. Geophys. Geosyst. 17, 3893-3916.

Carter, L.B., Dasgupta, R., 2015. Hydrous basalt-limestone interaction at crustal conditions: Implications for generation of ultracalcic melts and outflux of CO_2 at volcanic arcs. Earth Planet. Sci. Lett. 427, 202-214

Chadwick, J.P., Troll, V.R., Ginibre, C., Morgan, D., Gertisser, R., Waight, T.E., Davidson, J.P., 2007. Carbonate assimilation at Merapi Volcano, Java, Indonesia: Insights from crystal isotope stratigraphy. J. Petrol. 48, 1793-1812

Clague, D.A., Weber, W.S., Dixon, J.E., 1991. Picritic glasses from Hawaii. Nature 353, 553

Colson, R.O., McKay, G.A., Taylor, L.A., 1989. Charge balancing of trivalent trace elements in olivine and low-Ca pyroxene: A test using experimental partitioning data. Geochim. Cosmochim. Acta 53, 643-648

Connolly, J.A.D., Cesare, B., 1993. C-O-H-S fluid composition and oxygen fugacity in graphitic metapelites. J. Metamorph. Geol. 11, 379-388

Conte, A.M., Dolfi, D., Gaeta, M., Misiti, V., Mollo, S., Perinelli, C., 2009. Experimental constraints on evolution of leucite-basanite magma at 1 and 10^{-4} GPa: implications for parental compositions of Roman high-potassium magmas. Eur. J. Mineral. 21, 763-782

Coogan, L.A., Hain, A., Stahl, S., Chakraborty, S., 2005. Experimental determination of the diffusion coefficient for calcium in olivine between 900°C and 1500°C. Geochim. Cosmochim. Acta 69, 3683-3694

Coulson, I.M., Westphal, M., Anderson, R.G., Kyser, T.K., 2007. Concomitant skarn and syenitic magma evolution at the margins of the Zippa Mountain pluton. Mineral. Petrol. 90, 199-221

Dallai, L., Cioni, R., Boschi, C., D'Oriano, C., 2011. Carbonate-derived CO2purging magma at depth: Influence on the eruptive activity of Somma-Vesuvius, Italy. Earth Planet. Sci. Lett. 310, 84-95

Danyushevsky, L.V., Plechov, P., 2011. Petrolog3: Integrated software for modeling crystallization processes. Geochem. Geophys. Geosyst., 12, Q07021

Davidson, P.M., Mukhopadhyay, D.K., 1984. Ca-Fe-Mg olivines: phase relations and a solution model. Contrib. Mineral. Petrol. 86, 256-263

Deegan, F.M., Troll, V.R., Freda, C., Misiti, V., Chadwick, J.P., McLeod, C.L., Davidson, J.P., 2010. Magma-carbonate interaction processes and associated CO_2 release at Merapi Volcano, Indonesia: insights from experimental petrology. Journal of Petrology 51, 1027-1051

DePaolo, D.J., 1981. Trace element and isotopic effects of combined wall rock assimilation and fractional crystallization. Earth Planet. Sci. Lett. 53, 189-202

Del Bello, E., Mollo, S., Scarlato, P., von Quadt, A., Forni, F., Bachmann, O., 2014. New petrological constraints on the last eruptive phase of the Sabatini Volcanic District (central Italy): Clues from mineralogy, geochemistry, and Sr-Nd isotopes. Lithos 205, 28-38

Di Battistini, G., Montanini, A., Vernia, L., Venturelli, G., Tonarini, S., 2001. Petrology of melilite-bearing rocks from the Montefiascone Volcanic Complex (Roman Magmatic Province): New insights into the ultrapotassic volcanism of Central Italy. Lithos 59, 1-24

Di Rocco, T., Freda, C., Gaeta, M., Mollo, S., Dallai, L., 2012. Magma chambers emplaced in carbonate substrate: Petrogenesis of skarn and cumulate rocks and implications for CO_2 degassing in volcanic areas. J. Petrol. 53, 2307-2332

Doroshkevich, A.G., Ripp, G.S., Izbrodin, I.A., Savatenkov, V.M., 2012. Alkaline magmatism of the Vitim province, West Transbaikalia, Russia: Age, mineralogical, geochemical and isotope (O, C, D, Sr and Nd) data. Lithos 152, 157-172

Dunitz, J.D., Orgel, L.E., 1957. Electronic properties of transition-metal oxides—I: Distortions from cubic symmetry. J. Phys. Chem. Solids 3, 20-29

Dunn, T., 1987. Partitioning of Hf, Lu, Ti, and Mn between olivine, clinopyroxene and basaltic liquid. Contrib. Mineral. Petrol. 96, 476-484

Dunworth, E.A., Wilson, M., 1998. Olivine melilitites of the SW German Tertiary volcanic province: Mineralogy and petrogenesis. J. Petrol. 39, 1805-1836

Ferguson, A.K., 1978. Ca-enrichment in olivines from volcanic rocks. Lithos 11, 189-194

Filiberto, J., Dasgupta, R., 2011. Fe^{2+}-Mg partitioning between olivine and basaltic melts: Applications to genesis of olivine-phyric shergottites and conditions of melting in the Martian interior. Earth Planet. Sci. Lett. 304, 527-537

Foland, K.A., Landoll, J.D., Henderson, C.M.B., Chen, J., 1993. Formation of cogenetic quartz and nepheline syenites. Geochim. Cosmochim. Acta 57, 697-704

Ford, C.E., Russel, D.G., Craven, J.A., Fisk, M.R., 1983. Olivine-Liquid Equilibria: Temperature, Pressure and Composition Dependence of the Crystal/Liquid Cation Partition Coefficients for Mg, Fe^{2+}, Ca and Mn. J. Petrol. 24, 256-266

Francis, C.A., Ribbe, P.H., 1980. The forsterite-tephroite series: I. Crystal structure refinements. Am. Mineral. 65, 1263-1269

Freda, C., Gaeta, M., Giaccio, B., Marra, F., Palladino, D.M., Scarlato, P., Sottili, G., 2011. CO_2-driven large mafic explosive eruptions: the Pozzolane Rosse case study from the Colli Albani Volcanic District (Italy). Bull. Volc. 73, 241-256.

Freda, C., Gaeta, M., Misiti, V., Mollo, S., Dolfi, D., Scarlato, P., 2008. Magma-carbonate interaction: An experimental study on ultrapotassic rocks from Alban Hills (Central Italy). Lithos 101, 397-415

Fulignati, P., Marianelli, P., Santacroce, R., Sbrana, A., 2004. Probing the Vesuvius magma chamber-host rock interface through xenoliths. Geol. Mag. 141, 417-428.

Fulignati, P., Marianelli, P., Santacroce, R., Sbrana, A., 2000. The skarn shell of the 1944 Vesuvius magma chamber. Genesis and PTX conditions from melt and fluid inclusion data. Eur. J. Mineral. 12, 1025-1039.

Gaeta, M., Di Rocco, T., Freda, C., 2009. Carbonate assimilation in open magmatic systems: The role of melt-bearing skarns and cumulate-forming processes. J. Petrol. 50, 361-385

Gaetani, G.A., 2004. The influence of melt structure on trace element partitioning near the peridotite solidus. Contrib. to Mineral. Petrol. 147, 511-527

Galoisy, L., Calas, G., Brown, G.E., 1995. Intracrystalline distribution of Ni in San Carlos olivine: an EXAFS study. Am. Mineral. 80, 1089-1092

Gee, L.L., Sack, R.O., 1988. Experimental petrology of melilite nephelinites. J. Petrol. 29, 1233-1255

Gozzi, F., Gaeta, M., Freda, C., Mollo, S., Di Rocco, T., Marra, F., Dallai, L., Pack, A., 2014. Primary magmatic calcite reveals origin from crustal carbonate. Lithos 190-191, 191-203

Hart, S.R., Davis, K.E., 1978. Nickel partitioning between olivine and silicate melt. Earth Planet. Sci. Lett. 40, 203-219

Hayes, B., Lissenberg, C.J., Bédard, J.H., Beard, C., 2015. The geochemical effects of olivine slurry replenishment and dolostone assimilation in the plumbing system of the Franklin Large Igneous Province, Victoria Island, Arctic Canada. Contrib. to Mineral. Petrol. 169

Heinemann, R., Staack, V., Fischer, A., Kroll, H., Vad, T., Kirfel, A., 1999. Temperature dependence of Fe, Mg partitioning in Acapulco olivine. Am. Mineral. 84, 1400-1405

Henderson, P., Dale, I.M., 1970. The partitioning of selected transition element ions between olivine and groundmass of oceanic basalts. Chem. Geol. 3, 267-274

Henderson, C.M.B., Knight, K.S., Redfern, S.A.T., Wood, B.J., 1996. High-temperature study of octahedral cation exchange in olivine by neutron powder diffraction. Science 271, 1713-1715

Herzberg, C., O'Hara, M.J., 1998. Phase equilibrium constraints on the origin of basalts, picrites, and komatiites. Earth Sci. Rev. 44, 39-79

Huang, F., Lundstrom, C.C., McDonough, W.F., 2006. Effect of melt structure on trace-element partitioning between clinopyroxene and silicic, alkaline, aluminous melts. Am. Mineral. 91, 1385-1400

Iacono Marziano, G., Gaillard, F., Scaillet, B., Pichavant, M., Chiodini, G., 2009. Role of non-mantle CO_2 in the dynamics of volcano degassing: The Mount Vesuvius example. Geology, 37, 319-322

Iacono Marziano, G., Gaillard, F., Pichavant, M., 2008. Limestone assimilation by basaltic magmas: an experimental re-assessment and application to Italian volcanoes. Contrib. Mineral. Petrol. 155, 719-738

Irvine, T.N., 1982. Terminology for layered intrusions. J. Petrol. 23, 127-162

Irvine, T.N., Kushiro, I., 1976. Partitioning of Ni and Mg between olivine and silicate liquids. Carnegie Inst. Wash. Yearb. 75, 668-675

Jaeger, W.L., Drake, M.J., 2000. Metal-silicate partitioning of Co, Ga, and W: dependence on silicate melt composition. Geochim. Cosmochim. Acta 64, 3887-3895

Jackson, W.E., Farges, F., Yeager, M., Mabrouk, P.A., Rossano, S., Waychunas, G.A., Solomon, E.I., Brown, G.E., 2005. Multispectroscopic study of Fe(II) in silicate glasses: implications for the coordination environment of Fe(II) in silicate melts. Geochim. Cosmochim. Acta 69, 4315-4332

Jana, D., Walker, D., 1997. The influence of sulfur on partitioning of siderophile elements. Geochim. Cosmochim. Acta 61, 5255-5277

Jolis, E.M., Troll, V.R, Harris, C., Freda, C., Gaeta, M., Orsi G, Siebe, C., 2015. Skarn xenolith record crustal CO2 liberation during Pompeii and Pollena eruptions, Vesuvius volcanic system, central Italy. Chem. Geol. 415, 17-36

Jolis, E.M., Freda, C., Troll, V.R., Deegan, F.M., Blythe, L.S., McLeod, C.L., Davidson, J.P., 2013. Experimental simulation of magma-carbonate interaction beneath Mt. Vesuvius, Italy. Contrib. to Mineral. Petrol. 166, 1335-1353

Jones, J.H., 2016. Thoughts and Reminiscences on Experimental Trace Element Partitioning. Geochemical Perspect. 5, 147-251

Jones, J.H., 1995. Experimental trace element partitioning. In: Ahrens, T.J. (Ed.) Rock Physics and Phase Relations, A Handbook of Physical Constants. AGU Reference Shelf 3, American Geophysical Union, Washington, D.C., USA, 73-104

Jones, J.H., 1988. Partitioning of Mg and Fe between olivine and liquids of lunar compositions: the roles of composition, pressure, and Ti speciation (Abstract). In: Lunar Planetary Science XIX. Lunar and Planetary Institute, Houston, USA, 561-562

Jones, J.H., 1984. Temperature and pressure-independent correlations of olivine liquid partition coefficients and their application to trace element partitioning. Contrib. to Mineral. Petrol. 88, 126-132

Jurewicz, A.J.G., Watson, E.B., 1988. Cations in olivine, Part 2: Diffusion in olivine xenocrysts, with applications to petrology and mineral physics. Contrib. to Mineral. Petrol. 99, 186-201

Keppler, H., 1992. Crystal field spectra and geochemistry of transition metal ions in silicate melts and glasses. Am. Mineral. 77, 62-75

Keppler, H., Bagdassarov, N.S., 1999. The speciation of Ni and Co in silicate melts from optical absorption spectra to 1500°C. Chem. Geol. 158, 105-115

Kohn, S.C., Schofield, P.F., 1994. The importance of melt composition in controlling trace-element behaviour: an experimental study of Mn and Zn partitioning between forsterite and silicate melts. Chem. Geol. 117, 73-87

Korenaga, J., Kelemen, P.B., 2000. Major element heterogeneity in the mantle source of the North Atlantic igneous province. Earth Planet. Sci. Lett. 184, 251-268

Kress, V.C., Carmichael, I.S., 1991. The compressibility of silicate liquids containing Fe_2O_3 and the effect of composition, temperature, oxygen fugacity and pressure on their redox states. Contrib. to Mineral. Petrol. 108, 82-92

Kushiro, I., Mysen, B.O., 2002. A possible effect of melt structure on the Mg-Fe partitioning between olivine and melts. Geochim. Cosmochim. Acta 66, 2267-2272

Kushiro, I., Walter, M.J., 1998. Mg-Fe partitioning between olivine and mafic-ultramafic melts. Geophys. Res. Lett. 25, 2337-2340

Langmuir, C.H., Hanson, G.N., 1981. Calculating Mineral—Melt Equilibria with Stoichiometry, Mass Balance, and Single-Component Distribution Coefficients. In Thermodynamics of minerals and melts Springer, New York, NY, pp. 247-271

Le Bas, M., Maitre, R.L., Streckeisen, A., Zanettin, B., IUGS Subcommission on the Systematics of Igneous Rocks, 1986. A chemical classification of volcanic rocks based on the total alkali-silica diagram. J. Petrol. 27, 745-750

Lee, S.K., Stebbins, J.F., 2003. The distribution of sodium ions in aluminosilicate glasses: a high-field Na-23 MAS and 3Q MAS NMR study. Geochim. Cosmochim. Acta 67, 1699-1709

Leeman, W.P., 1978. Distribution of Mg^{2+} between olivine and silicate melt, and its implications regarding melt structure. Geochim. Cosmochim. Acta 42, 789-800

Leeman, W.P., Scheidegger, K.F., 1977. Olivine/liquid distribution coefficients and a test for crystal-liquid equilibrium. Earth Planet. Sci. Lett. 35, 247-257

Lentz, D.R., 1999. Petrology, geochemistry, and oxygen isotope interpretation of felsic volcanic and related rocks hosting the Brunswick 6 and 12 massive sulfide deposits (Brunswick Belt), Bathurst mining camp, New Brunswick, Canada. Econ. Geol. 94, 57-86

Li, C., Ripley, E.M., 2010. The relative effects of composition and temperature on olivine-liquid Ni partitioning: Statistical deconvolution and implications for petrologic modeling. Chem. Geol. 275, 99-104

Libourel, G., 1999. Systematics of calcium partitioning between olivine and silicate melt: Implications for melt structure and calcium content of magmatic olivines. Contrib. to Mineral. Petrol. 136, 63-80

Libourel, G., Boivin, P., Biggar, G.M., 1989. The univariant curve liquid = forsterite + anorthite + diopside in the system CMAS at 1 bar: solid solutions and melt structure. Contrib. to Mineral. Petrol. 102, 406-421

Longhi, J., Pan, V., 1988. A reconnaissance study of phase boundaries in low-alkali basaltic liquids. J. Petrol. 29, 115-147

Longhi, J., Walker, D., Hays, J.F., 1978. The distribution of Fe and Mg between olivine and lunar basaltic liquids. Geochim. Cosmochim. Acta 42, 1545-1558

Lumpkin, G.R., Ribbe, P.H., Lumpkin, N.E., 1983. Composition, order-disorder and lattice parameters of olivines; determinative methods for Mg-Mn and Mg-Ca silicate olivines. Am. Mineral. 68, 1174-1182

Lynn, K.J., Shea, T., Garcia, M.O., 2017. Nickel variability in Hawaiian olivine: Evaluating the relative contributions from mantle and crustal processes. Am. Mineral. 102, 507-518

Maekawa, H., Maekawa, T., Kawamura, K., Yokokawa, T., 1991. The structural groups of alkali silicate glasses determined from 29Si MAS-NMR. J. Non-Cryst. Solids 127, 53-64

Mason, E., Edmonds, M., Turchyn, A.V., 2017. Remobilization of crustal carbon dominates volcanic arc emissions. Science 357, 290-294

Matzen. A.K., Baker, M.B., Beckett, J.R., Wood, B.J., Stolper, E.M., 2017. The effect of liquid composition on the partitioning of Ni between olivine and silicate melt. Contrib. to Mineral. Petrol. 172, 1-18

Matzen, A.K., Baker, M.B., Beckett, J.R., Stolper, E.M., 2013. The temperature and pressure dependence of nickel partitioning between olivine and silicate melt. J. Petrol. 54, 2521-2545

Matzen, A.K., Baker, M.B., Beckett, J.R., Stolper, E.M., 2011. Fe-Mg partitioning between olivine and high-magnesian melts and the nature of Hawaiian parental liquids. J. Petrol. 52, 1243-1263

Mibe, K., Orihashi, Y., Nakai, S., Fuji, T., 2006. Element partitioning between transition-zone minerals and ultramafic melt under hydrous conditions. Geophys. Res. Lett. 33, 1-6

Mollo, S., Hammer, J.E., 2017. Dynamic crystallization in magmas. In Mineral reaction kinetics: microstructures, textures, chemical and isotopic signatures. Edited by W. Heinrich and R. Abart. EMU Notes in Mineralogy, Vol. 16 (2016), Chapter 7, 1-46. Published by the European Mineralogical Union and the Mineralogical Society of Great Britain & Ireland

Mollo, S., Forni F., Bachmann, O., Blundy, J.D., De Astis, G., Scarlato, P., 2016. Trace element partitioning between clinopyroxene and trachy-phonolitic melts: A case study from the Campanian ignimbrite (Campi Flegrei, Italy). Lithos 252-253, 160-172

Mollo, S., Giacomoni, P.P., Coltorti, M., Ferlito, C., Iezzi, G., Scarlato, P., 2015. Reconstruction of magmatic variables governing recent Etnean eruptions: constraints from mineral chemistry and *P-T-*f_{O2}-H_2O modelling. Lithos 212-215, 311-320

Mollo, S., Vona, A., 2014. The geochemical evolution of clinopyroxene in the Roman Province: A window on decarbonation from wall-rocks to magma. Lithos 192-195, 1-7

Mollo, S., Heap, M.J., Dingwell, D.B., Hess, K.U., Iezzi, G., Masotta, M., Scarlato, P., Vinciguerra, S., 2013a. Decarbonation and thermal microcracking under magmatic P-T-fCO_2 conditions: the role of skarn substrata in promoting volcanic instability, Geophysical Journal International 195, 369-380

Mollo, S., Blundy, J.D., Scarlato, P., Iezzi, G., Langone, A., 2013b. The partitioning of trace elements between clinopyroxene and trachybasaltic melt during rapid cooling and crystal growth, Contrib. to Mineral. Petrol. 166, 1633-1654

Mollo, S., Putirka, K.D., Iezzi, G., Scarlato, P., 2013c. The control of cooling rate on titanomagnetite composition: Implications for a geospeedometry model applicable to alkaline rocks from Mt. Etna volcano, Contrib. to Mineral. Petrol. 165, 457-475

Mollo, S., Scarlato, P., Freda, C., Gaeta, M., 2011. Basalt-crust interaction processes: insights from experimental petrology, 33-61, in West, J.P., eds., Basalt: Types, Petrology and Uses: New York, Nova Science Publishers, 189

Mollo, S., Gaeta, M., Freda, C., Di Rocco, T., Misiti, V., Scarlato, P., 2010. Carbonate assimilation in magmas: A reappraisal based on experimental petrology. Lithos 114, 503-514

Mukhopadhyay, D.K., Lindsley, D.H., 1983. Phase relations in the join kirschsteinite - fayalite. Am. Mineral. 68, 1089-1094.

Mysen, B.O., 2008. Olivine/melt transition metal partitioning, melt composition, and melt structure-melt polymerization and Qn-speciation in alkaline earth silicate systems. Geochim. Cosmochim. Acta 72, 4796-4812

Mysen, B.O., 2007. The solution behavior of H_2O in peralkaline aluminosilicate melts at high pressure with implications for properties of hydrous melts. Geochim. Cosmochim. Acta 71, 1820-1834

Mysen, B.O., 2006. Redox equilibria of iron and silicate melt structure: Implications for olivine/melt element partitioning. Geochim. Cosmochim. Acta 70, 3121-3138

Mysen, B.O., 2004. Element partitioning between minerals and melt, melt composition, and melt structure. Chem. Geol. 213, 1-16

Mysen, B.O., Richet, P., 2005. Silicate glasses and melts: properties and structure. Elsevier, New York, 548

Mysen, B.O., Dubinsky, E.V., 2004. Melt structural control on olivine/melt element partitioning of Ca and Mn1. Geochim. Cosmochim. Acta 68, 1617-1633.

Mysen, B.O., Virgo, D., 1980. Trace element partitioning and melt structure: An experimental study at 1 atm pressure. Geochim. Cosmochim. Acta 44, 1917-1930

Mysen, B.O., Carmichael, I.S.E., Virgo, D., 1985. A comparison of iron redox ratios in silicate glasses determined by wet-chemical and 57 Fe Mössbauer resonant absorption methods. Contrib. to Mineral. Petrol. 90, 101-106

Mysen, B.O., Virgo, D., Seifert, F.A., 1982. The structure of silicate melts: implications for chemical and physical properties of natural magma. Rev. of Geophys. 20, 353-383

Nielsen R.L., Davidson P.M., Grove T.L., 1988. Pyroxene-melt equilibria: an updated model. Contrib. to Mineral. Petrol. 100, 361-373

Papike, J.J., Karner, J.M., Shearer, C.K., 2005. Comparative planetary mineralogy: Valence state partitioning of Cr, Fe, Ti, and V among crystallographic sites in olivine, pyroxene, and spinel from planetary basalts. Am. Mineral. 90, 277-290

Patiño Douce, A.E., 1999. What do experiments tell us about the relative contributions of crust and mantle to the origin of granitic magmas? Geological Society, London, Special Publications 168, 55-75

Pu, X., Lange, R.A., Moore, G., 2017. A comparison of olivine-melt thermometers based on D_{Mg} and D_{Ni}: The effects of melt composition, temperature, and pressure with applications to MORBs and hydrous arc basalts. Am. Mineral. 102, 750-765

Putirka, K.D., 2016. Rates and styles of planetary cooling on Earth, Moon, Mars, and Vesta, using new models for oxygen fugacity, ferric-ferrous ratios, olivine-liquid Fe-Mg exchange, and mantle potential temperature. Am. Mineral. 101, 819-840

Putirka, K.D., 2005. Mantle potential temperatures at Hawaii, Iceland, and the mid-ocean ridge system, as inferred from olivine phenocrysts: Evidence for thermally driven mantle plumes. Geochemistry, Geophys. Geosystems 6, 1-14

Putirka, K.D., Ryerson, F.J., Perfit, M., Ridley, W.I., 2011. Mineralogy and composition of the oceanic mantle. J. Petrol. 52, 279-313

Putirka, K.D., Perfit, M., Ryerson, F.J., Jackson, M.G., 2007. Ambient and excess mantle temperatures, olivine thermometry, and active vs. passive upwelling. Chem. Geol. 241, 177-206

Redfern, S.A.T., Henderson, C.M.B., Wood, B.J., Harrison, R.J., Knight, K.S., 1996. Determination of olivine cooling rates from metal-cation ordering. Nature 381, 407

Redi, D., Cannatelli, C., Esposito, R., Lima, A., Petrosino, P., De Vivo, B., 2017. Somma-Vesuvius' activity: a mineral chemistry database. Mineral. Petrol. 111, 43-67

Rein, R.H., Chipman, J., 1965. Activities in liquid solution SiO_2-CaO-MgO-Al_2O_3 at 1600°C. Transactions of the Metallurgical Society of AIME 233, 415

Roeder, P.L., 1974. Activity of iron and olivine solubility in basaltic liquids. Earth Planet. Sci. Lett. 23, 397-410

Roeder, P.L., Emslie, R.F., 1970. Olivine-Liquid Equilibrium. Contrib. to Mineral. Petrol. 29, 275-289

Sack, R.O., Walker, D., Carmichael, I.S., 1987. Experimental petrology of alkalic lavas: constraints on cotectics of multiple saturation in natural basic liquids. Contrib. to Mineral. Petrol. 96, 1-23

Schmidt, M.W., 2006. Element Partitioning: The Role of Melt Structure and Composition. Science 312, 1646-1650

Shi, P., 1993. Low pressure phase relationships in the system Na_2O-CaO-FeO-MgO-Al_2O_3-SiO_2 at 1100°C, with implications for the differentiation of basaltic magmas. J. Petrol. 34, 743-762

Shi, P., Libourel, G., 1991. The effects of FeO on the system CMAS at low pressure and implications for basalt crystallization processes. Contrib. to Mineral. Petrol. 108, 129-145

Snyder, D.A., Carmichael, I.S.E., 1992. Olivine-liquid equilibria and the chemical activities of FeO, NiO, Fe_2O_3, and MgO in natural basic melts. Geochim. Cosmochim. Acta 56, 303-318

Snyder, D., Carmichael, I.S.E., Wiebe, R.A., 1993. Experimental study of liquid evolution in an Fe-rich, layered mafic intrusion: constraints of Fe-Ti oxide precipitation on the T-fO_2 and T-P paths of tholeiitic magmas. Contrib. to Mineral. Petrol. 113, 73-86

Sobolev, A.V., Hofmann, A.W., Kuzmin, D.V., Yaxley, G.M., Arndt, N.T., Chung, S.L., Gurenko, A.A., 2007. The amount of recycled crust in sources of mantle-derived melts. Science 316, 412-417

Sobolev, A.V., Hofmann, A.W., Sobolev, S.V., Nikogosian, I.K., 2005. An olivine-free mantle source of Hawaiian shield basalts. Nature 434, 590

Spandler, C., Martin, L.H.J., Pettke, T., 2012. Carbonate assimilation during magma evolution at Nisyros (Greece), South Aegean Arc: Evidence from clinopyroxenite xenoliths. Lithos 146-147, 18-33

Spera, F.J., Bohrson, W.A., 2004. Open-system magma chamber evolution: An energy-constrained geochemical model incorporating the effects of concurrent eruption, recharge, variable assimilation and fractional crystallization (EC-E′ RAχFC). J. Petrol. 45, 2459-2480

Spera, F.J., Bohrson, W.A., 2001. Energy-constrained open-system magmatic processes I: General model and energy-constrained assimilation and fractional crystallization (EC-AFC) formulation. J. Petrol. 42, 999-1018

Stormer, J.C., Nicholls, J., 1978. XLFRAC: a program for the interactive testing of magmatic differentiation models. Comput. Geosci. 4, 143-159

Takahashi, E., 1978. Partitioning of Ni^{2+}, Co^{2+}, Fe^{2+}, Mn^{2+} and Mg^{2+} between olivine and silicate melts: compositional dependence of partition coefficient. Geochim. Cosmochim. Acta 42, 1829-1844

Thibault, Y., Walter, M.J., 1995. The influence of pressure and temperature on the metal-silicate partition coefficients of nickel and cobalt in a model C1 chondrite and implications for metal segregation in a deep magma ocean. Geochim. Cosmochim. Acta 59, 991-1002

Toplis, M.J., 2005. The thermodynamics of iron and magnesium partitioning between olivine and liquid: Criteria for assessing and predicting equilibrium in natural and experimental systems. Contrib. to Mineral. Petrol. 149, 22-39

Toplis, M.J., Carroll, M.R., 1995. An experimental study of the influence of oxygen fugacity on Fe-Ti oxide stability, phase relations, and mineral—melt equilibria in ferro-basaltic systems. J. Petrol. 36, 1137-1170

Troll, V.R., Deegan, F.M., Jolis, E.M., Harris, C., Chadwick, J.P., Gertisser, R., Preece, K., 2013. Magmatic differentiation processes at Merapi Volcano: inclusion petrology and oxygen isotopes. J. Volcanol. Geotherm. Res. 261, 38-49

Troll, V.R., Hilton, D.R., Jolis, E.M., Chadwick, J.P., Blythe, L.S., Deegan, F.M., Zimmer, M., 2012. Crustal CO_2 liberation during the 2006 eruption and earthquake events at Merapi volcano, Indonesia. Geophys. Res. Lett. 39

Vetere, F., Sato, H., Ishibashi, H., De Rosa, R., Donato, P., Ishibashi, H., De Rosa, R., Donato, P., 2013. Viscosity changes during crystallization of a shoshonitic magma: new insights on lava flow emplacement. J. Mineral. Petrol. Sci. 108, 144-160

Wagner, T.P., Grove, T.L., 1997. Experimental constraints on the origin of lunar high-Ti ultramafic glasses. Geochim. Cosmochim. Acta 61, 1315-1327

Wang, Z., Gaetani, G.A., 2008. Partitioning of Ni between olivine and siliceous eclogite partial melt: Experimental constraints on the mantle source of Hawaiian basalts. Contrib. to Mineral. Petrol. 156, 661-678

Watson, E.B., 1977. Partitioning of manganese between forsterite and silicate liquid. Geochim. Cosmochim. Acta 41, 1363-1374

Wenzel, T., Baumgartner, L.P., Konnikov, E.G., Bru, G.E., Kislov, E. V, 2002. Partial Melting and Assimilation of Dolomitic Xenoliths by Mafic Magma: the Ioko-Dovyren Intrusion (North Baikal Region, Russia). J. Petrol. 43, 2049-2074

Wenzel, T., Baumgartner, L.P., Brügmann, G.E., Konnikov, E.G., Kislov, E. V., Orsoev, D.A., 2001. Contamination of mafic magma by partial melting of dolomitic xenoliths. Terra Nov. 13, 197-202

Warner, R.D., Luth, W.C., 1973. Data for the Join Monticellite ($CaMgSiO_4$) - Forsterite (Mg_2SiO_4): Experimental Results and Numerical Analysis. Am. Mineral. 58, 998-1008

Wood, B.J., 1974. The solubility of alumina in orthopyroxene coexisting with garnet. Contrib. to Mineral. Petrol. 46, 1-15

Wood, B.J., Blundy, J.D., 1997. A predictive model for rare earth element partitioning between clinopyroxene and anhydrous silicate melt. Contrib. to Mineral. Petrol. 129, 166-181

Figure captions

Fig. 1. Variation of major oxides in olivine from magma-carbonate interaction experiments. Error bars are not observable if they are smaller than the symbols.

Fig. 2. Variation of olivine components from magma-carbonate interaction experiments. The solution model refers to four end-members: forsterite, fayalite, calcio-olivine (i.e., larnite), and tephroite. Error bars are not observable if they are smaller than the symbols.

Fig. 3. Relationship between olivine and melt compositional variations as a function of temperature, $CaCO_3$, and $^{melt}Mg\#$. a_{MgO}^{melt}, a_{CaO}^{melt}, and a_{SiO2}^{melt} come from the magnesium, calcium, and silicon pseudo-activity models of Leeman (1978), Libourel (1999), and Bottinga at al. (1981), respectively. Error bars are not observable if they are smaller than the symbols.

Fig. 4. Olivine-melt partition coefficients of Ni, Mg, Fe^{2+}, Mn, and Ca from magma-carbonate interaction experiments. Error bars are not observable if they are smaller than the symbols.

Fig. 5. $\ln D_i^{2+}$ vs. $1/T$ diagram showing the linear correlation between divalent partition coefficient and temperature (a). $\ln D_i^{2+}$ vs. a_{CaO}^{melt} diagram showing the linear correlation between divalent partition coefficient and calcium activity in the melt (b). Straight lines refer to regression fits (see the text for further details). Error bars are not observable if they are smaller than the symbols.

Fig. 6. D_{Mn}^{2+} vs. NBO/T diagram showing the partitioning behavior of Mn from magma-carbonate interaction experiments in comparison with previous data from literature reported in Bédard (2005). Error bars are not observable if they are smaller than the symbols.

Fig. 7. Olivine-melt exchange partition coefficients between Fe^{2+}/Ca/Mn/Ni and Mg from magma-carbonate interaction experiments. Error bars are not observable if they are smaller than the symbols.

Fig. 8. $K_{D(Fe-Mg)}$ (a), $K_{D(Ca-Mg)}$ (b), $K_{D(Mn-Mg)}$ (c), and $K_{D(Ni-Mg)}$ (d) from magma-carbonate interaction experiments are plotted against the value of NBO/T. Error bars are not observable if they are smaller than the symbols.

Fig. 9. Natural products from the Colli Albani Volcanic District (CAVD) in Italy are compared with those from this study. The NiO vs. Fo diagram displays the chemical changes of olivine phenocrysts found in cumulates and endoskarns at CAVD (a). Results from $^{melt}Mg\#_{78}$ decarbonation experiments confirm that Ni is negatively correlated with Fo, as the amount of carbonate assimilated increases from 0 to 10 to 20 wt.%. The Ni vs. CaO diagram shows the contamination path of melt inclusions entrapped in the same olivine phenocrysts (b). The melt inclusion with the highest Ni and lowest CaO contents is used as starting composition to track the combined effects of assimilation and fractional crystallization (AFC). Olivine-melt partition coefficients of Ca (D_{Ca}^{2+} = 0.15) and Ni (D_{Ni}^{2+} = 11.22) are estimated through Eqns. 11 and 26, respectively. The CaO content of the assimilant is set to 45 wt.%. The amount of fractionated olivine is lower than 8% and the ratio of the assimilation rate to the crystallization rate changes from 0.01 to 0.2. Natural data from Gaeta et al., 2009 and Di Rocco et al., 2012).

Fig. 1S. D_{Ca}^{2+} values measured from magma-carbonate interaction experiments vs. those predicted by the models of Snyder and Carmichael (1992) (a), Libourel (1999) (b), and this study (c).

Fig. 2S. D_{Mg}^{2+} values measured from magma-carbonate interaction experiments vs. those predicted by the models of Beattie (1993) (a), Putirka et al. (2007) (b), Pu et al. (2017) (c), and this study (d).

Fig. 3S. D_{Fe}^{2+} values measured from magma-carbonate interaction experiments vs. those predicted by the models of Jones (2016) (a), Wang and Gaetani (2008) (b), this study (c), and Wang and Gaetani (2008) (d).

Fig. 4S. D_{Mn}^{2+} values measured from magma-carbonate interaction experiments vs. those predicted by the models of Wang and Gaetani (2008) (a) and this study (b).

Fig. 5S. D_{Ni}^{2+} values measured from magma-carbonate interaction experiments vs. those predicted by the models of Snyder and Carmichael (1992) (a), Wang and Gaetani (2008) (b), and Pu et al. (2017) (c).

Fig. 6S. $K_{D(Fe-Mg)}$ values measured from magma-carbonate interaction experiments vs. those predicted by the models of Toplis (2005) (a), Putirka (2016) for ferric iron in the melt recalculated according to Kress and Carmichael (1991) (b), and Putirka (2016) for all iron in the melt treated as FeO_t (c).

Figures

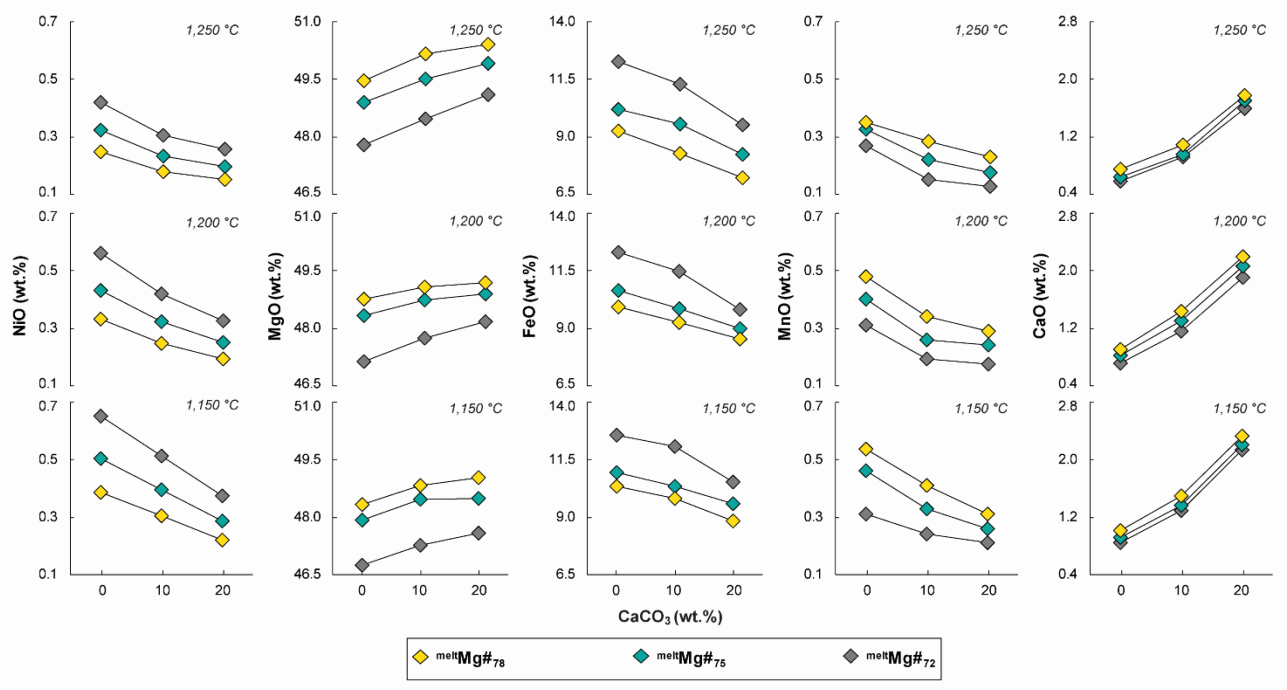

Figure 1

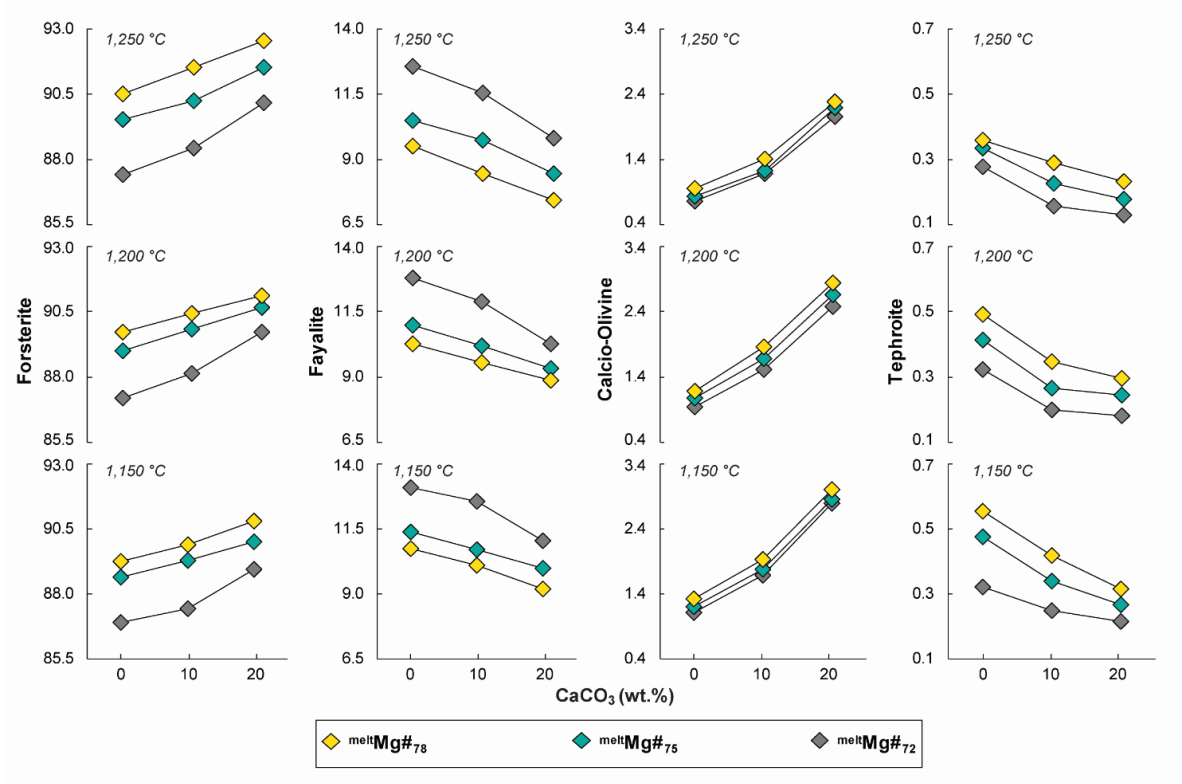

Figure 2

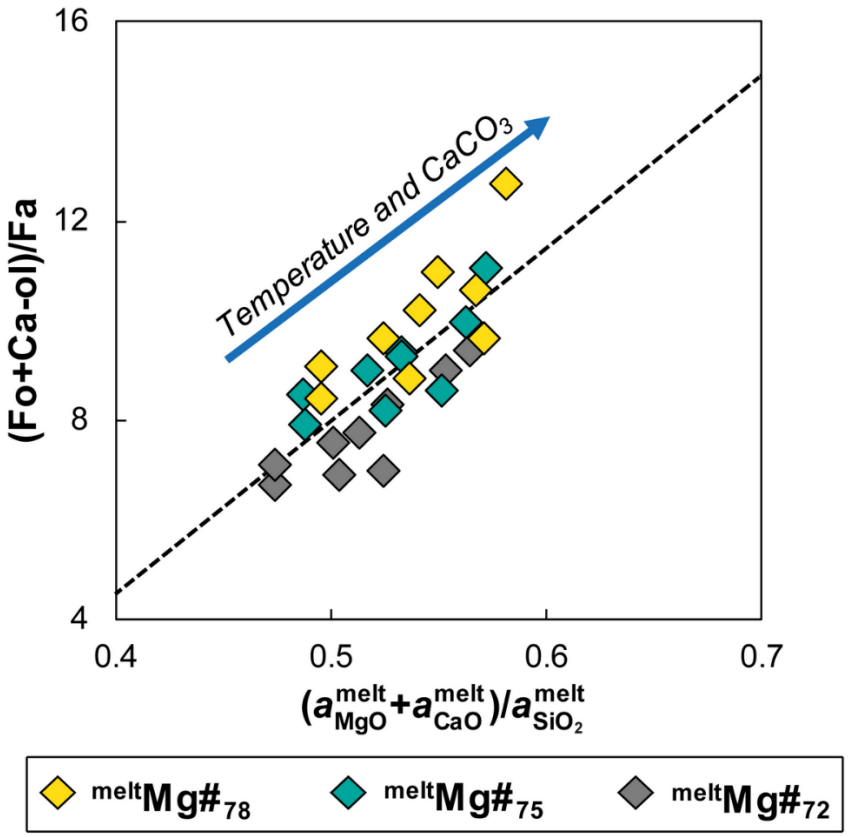

Figure 3

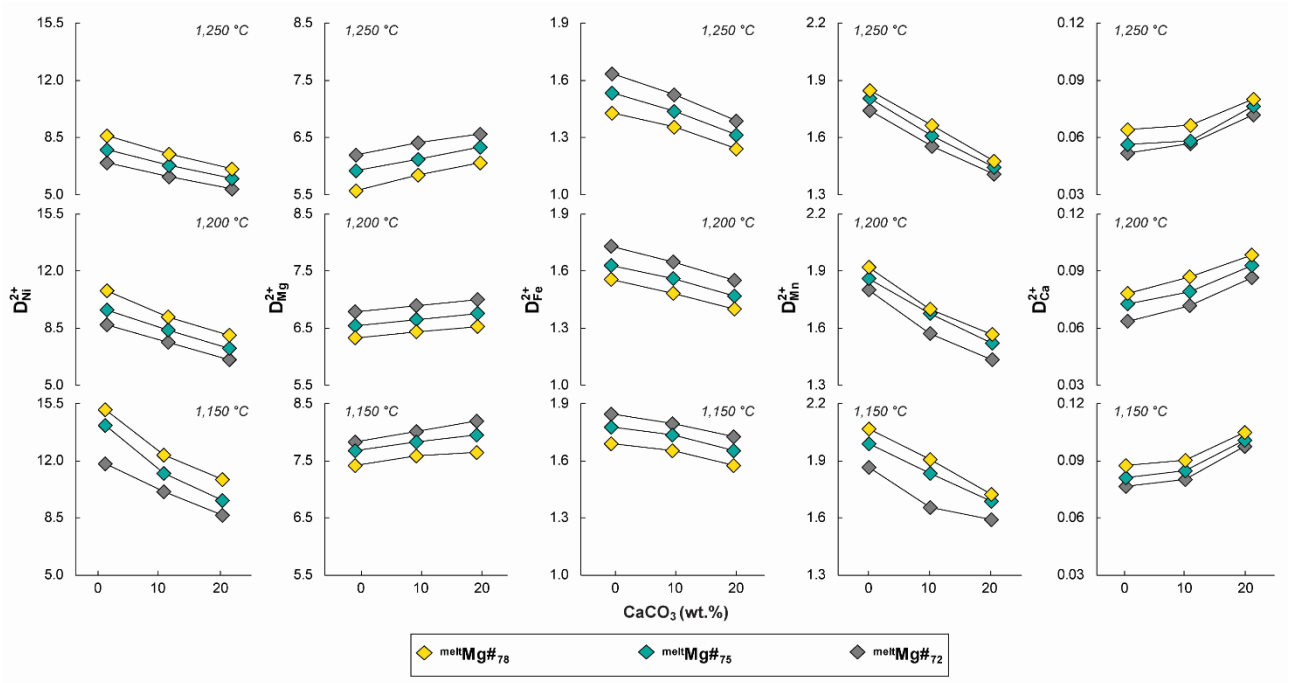

Figure 4

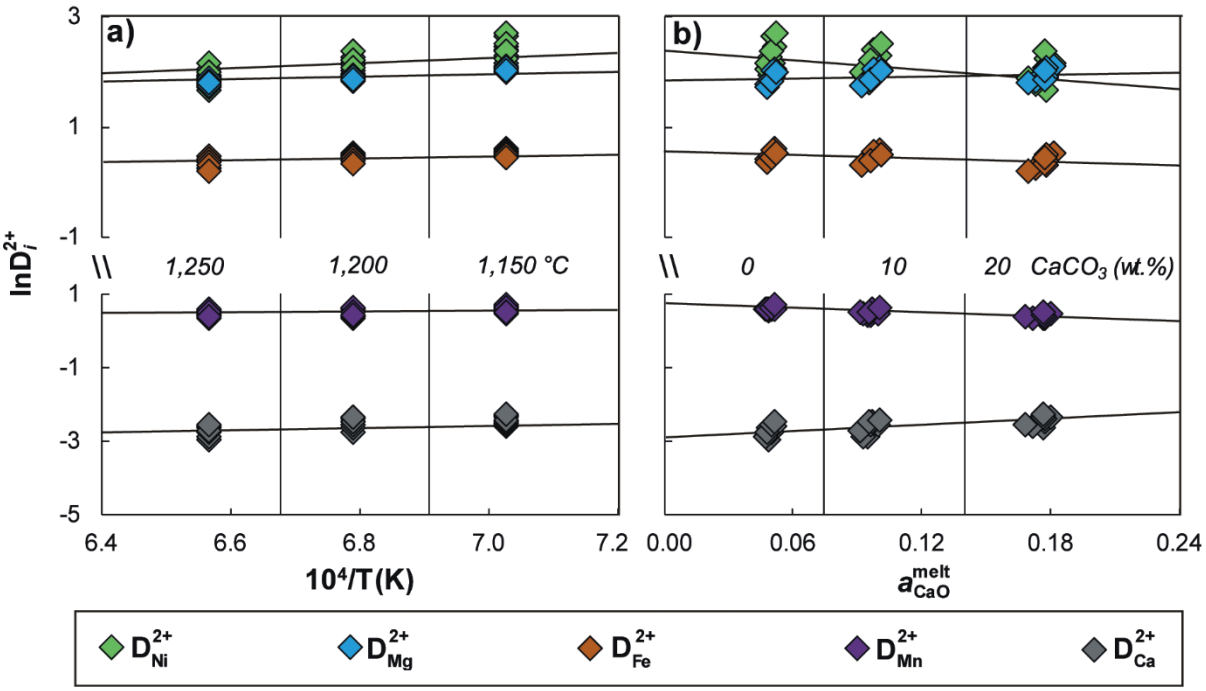

Figure 5

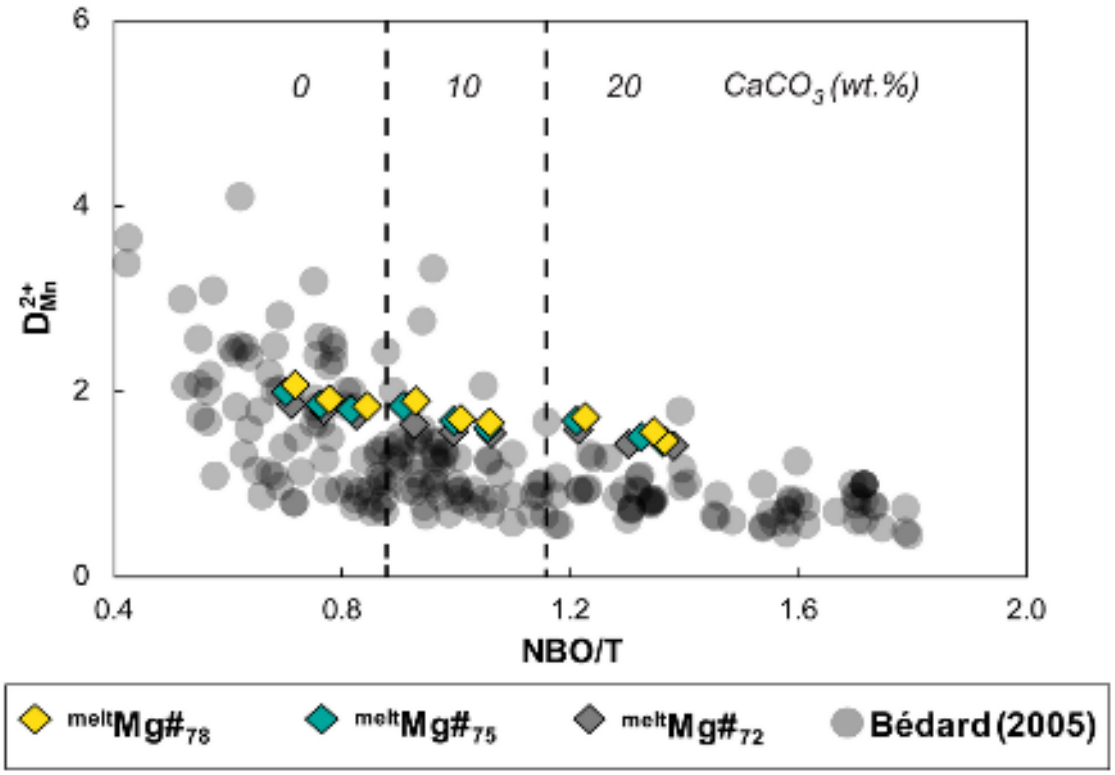

Figure 6

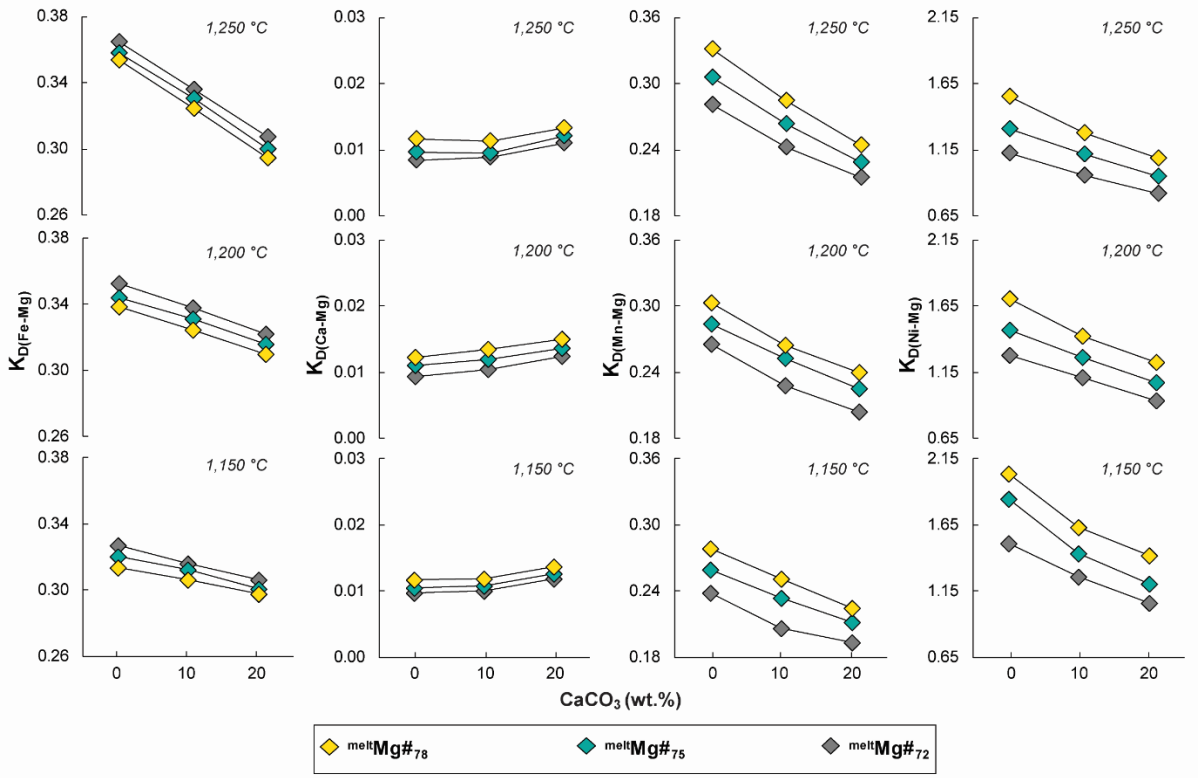

Figure 7

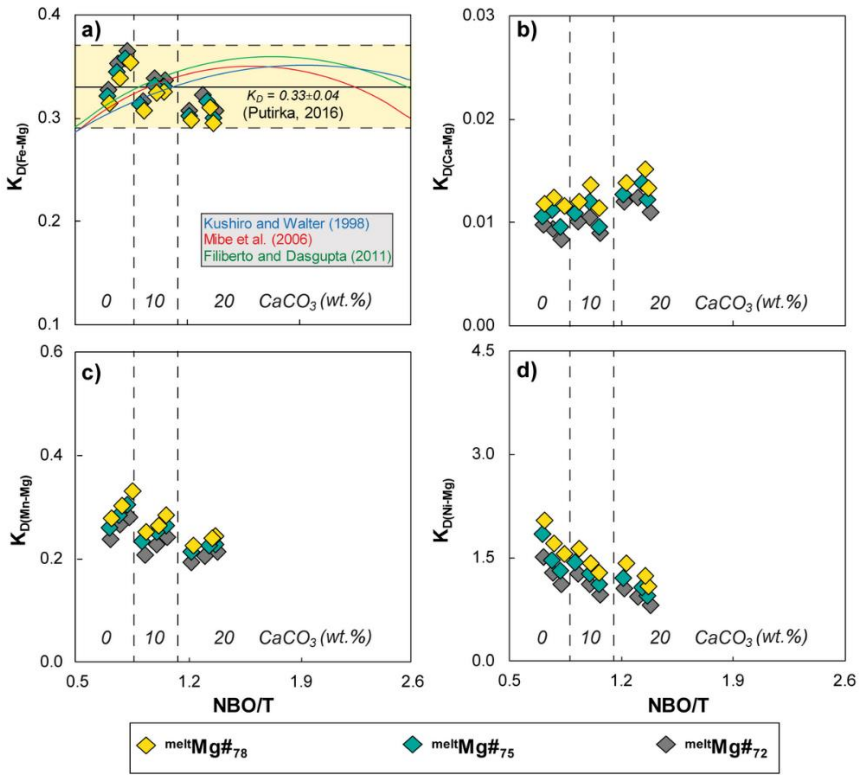

Figure 8

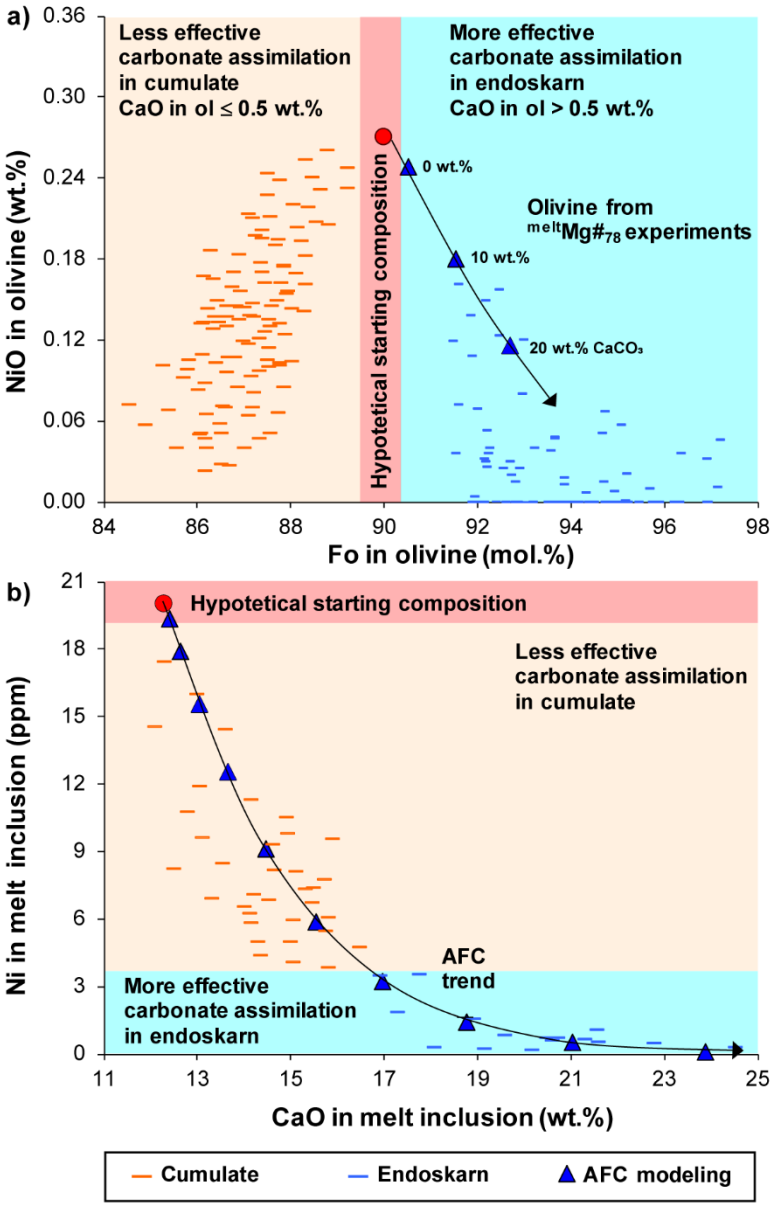
a)
Less effective carbonate assimilation in cumulate CaO in ol ≤ 0.5 wt.%
More effective carbonate assimilation in endoskarn CaO in ol > 0.5 wt.%
Hypotetical starting composition
0 wt.%
10 wt.%
20 wt.% CaCO3
Olivine from meltMg#78 experiments
NiO in olivine (wt.%)
Fo in olivine (mol.%)
b)
Hypotetical starting composition
Less effective carbonate assimilation in cumulate
AFC trend
More effective carbonate assimilation in endoskarn
Ni in melt inclusion (ppm)
CaO in melt inclusion (wt.%)
Cumulate
Endoskarn
AFC modeling

Figure 9

Tables

Table 1. Experimental conditions and phase relations

Run (#)	Mg# melt	$CaCO_3$ (wt.%)	*t* (h)	T (°C)	P (MPa)	log(fO_2)	Gl (wt.%)	Ol (wt.%)	Cpx (wt.%)	Ti-Mt (wt.%)
MM1-A	72	0	72	1250	0.1	-7.7	96.5	3.5	-	-
MM1-C	72	10	72	1250	0.1	-7.7	97.8	2.2	-	-
MM1-D	72	20	72	1250	0.1	-7.7	99.1	0.9	-	-
MM2-A	72	0	72	1200	0.1	-8.2	93.7	6.3	-	-
MM2-C	72	10	72	1200	0.1	-8.2	86.9	4.8	8.3	-
MM2-D	72	20	72	1200	0.1	-8.2	84.2	1.5	14.3	-
MM3-A	72	0	72	1150	0.1	-8.85	79.1	8.0	11.6	1.2
MM3-C	72	10	72	1150	0.1	-8.85	76.7	6.4	15.7	1.2
MM3-D	72	20	72	1150	0.1	-8.85	74.7	4.1	20.2	1.0
MM4-A	75	0	72	1250	0.1	-7.7	95.7	4.3	-	-
MM4-C	75	10	72	1250	0.1	-7.7	96.7	3.3	-	-
MM4-D	75	20	72	1250	0.1	-7.7	98.1	1.9	-	-
MM5-A	75	0	72	1200	0.1	-8.2	92.8	7.2	-	-
MM5-C	75	10	72	1200	0.1	-8.2	94.7	5.3	-	-
MM5-D	75	20	72	1200	0.1	-8.2	95.2	4.8	-	-
MM6-A	75	0	72	1150	0.1	-8.85	90.7	9.3	-	-
MM6-C	75	10	72	1150	0.1	-8.85	87.3	7.7	5.0	-
MM6-D	75	20	72	1150	0.1	-8.85	79.0	6.7	14.3	-
MM7-A	78	0	72	1250	0.1	-7.7	93.3	6.7	-	-
MM7-C	78	10	72	1250	0.1	-7.7	95.0	5.0	-	-
MM7-D	78	20	72	1250	0.1	-7.7	97.2	2.8	-	-
MM8-A	78	0	72	1200	0.1	-8.2	90.1	9.9	-	-
MM8-C	78	10	72	1200	0.1	-8.2	91.7	8.3	-	-
MM8-D	78	20	72	1200	0.1	-8.2	92.2	7.8	-	-
MM9-A	78	0	72	1150	0.1	-8.85	88.0	12.0	-	-
MM9-C	78	10	72	1150	0.1	-8.85	89.5	10.5	-	-
MM9-D	78	20	72	1150	0.1	-8.85	81.4	9.1	9.5	-

Supplementary data to this article can be found online at https://doi.org/10.1016/j.lithos.2018.07.008.

The effect of CaO on the partitioning behavior of REE, Y and Sc between olivine and melt: Implications for basalt-carbonate interaction processes

Flavio Di Stefano[1], Silvio Mollo[1,2,*], Jonathan Blundy[3], Piergiorgio Scarlato[2], Manuela Nazzari[1,2], Olivier Bachmann[4]

[1]Dipartimento di Scienze della Terra, Sapienza-Università di Roma, P.le Aldo Moro 5, 00185 Roma, Italy

[2]Istituto Nazionale di Geofisica e Vulcanologia, Via di Vigna Murata 605, 00143 Rome, Italy

[3]School of Earth Sciences, University of Bristol, Wills Memorial Building, Bristol BS8 1RJ, UK

[4]Department of Earth Sciences, Institute of Geochemistry and Petrology, ETHZ, Clausiusstrasse 25, 8092 Zurich, Switzerland

Abstract

The partitioning of REE, Y and Sc (R^{3+}) between olivine and melt has been investigated experimentally during basalt-carbonate interaction. Three synthetic basalts ($^{melt}Mg\#_{72}$, $^{melt}Mg\#_{75}$ and $^{melt}Mg\#_{78}$) were doped with 0, 10 and 20 wt.% $CaCO_3$ and then equilibrated for 72 h at 1 atm, 1,150, 1,200 and 1,250 °C, and the QFM oxygen buffer. The thermal decomposition of $CaCO_3$ produced CaO contents in the melt up to ~22 wt.%. Regular relationships are found between the ionic radius and the partition coefficient (D_{R3+}), showing typical near-parabolic patterns. D_{R3+} is weakly dependent on temperature, but decreases with increasing $CaCO_3$ in the starting material (e.g., D_{Sc} decreases from 0.20 to 0.13). From the point of view of the lattice strain theory, D_{R3+} is described in terms of the radius of the crystal site (r_0), the Young Modulus (E) due to the elastic response of that site to lattice strain caused by cation insertion, and the strain-free partition coefficient (D_0^{3+}). The value of r_0 decreases as Ca cations are accommodated into the more distorted M2 site of olivine via progressive Ca-Fe substitutions. This mechanism is accompanied by a higher proportion of Mg cations entering into the smaller M1 site, making the optimum ionic radius smaller and favoring the crystallization of more forsteritic olivines from decarbonated melts. The enrichment of Ca in the crystal lattice is also proportional to the number of Si and Ca cations available in the melt. This causes E to be anticorrelated either with Ca in olivine or the activity of CaO in the melt. R^{3+} cations behave as network modifiers and, during basalt-carbonate interaction, the increasing abundance of non-bridging oxygens enhances the solubility of REE, Y and Sc in the melt. As a consequence, D_0^{3+} is negatively correlated with the degree of melt depolymerization. Additionally, the strain of the crystal lattice dominates the D_{R3+} parabolic patterns and D_0^{3+} is strongly controlled by forsterite and aluminium concentrations in olivine. The accommodation of REE, Y and Sc in the crystal lattice

requires maintenance of local charge-balance by the generation of vacancies, in accord with a paired substitution of R^{3+} and a vacancy for Mg in octahedral sites.

1. Introduction

Mafic olivine-bearing cumulates and endoskarns form in primitive skarn environments during the early stage of interaction between basaltic magmas and carbonate rocks (Di Rocco et al., 2012; Gaeta et al., 2009; Wenzel et al., 2002). This open-system process is more effective in the skarn rock shells, generating desilicated (i.e., SiO_2-poor) and decarbonated (CaO-rich) melts, in concert with fractionation and accumulation of Fo-CaO-rich olivine phenocrysts (Dallai et al., 2011; Di Rocco et al., 2012; Dunworth and Wilson, 1998; Fulignati et al., 2004; Gaeta et al., 2009; Gozzi et al., 2014; Redi et al., 2017; Wenzel et al., 2001, 2002). Generally, skarn-bearing dunite rocks result from high temperature decarbonation reactions commencing at 1,200-1,260 °C under redox conditions near the quartz-fayalite-magnetite (QFM) buffer (Di Rocco et al., 2012; Gaeta et al., 2009; Wenzel et al., 2002). The complex association of igneous and skarn rocks may have important repercussions for the origin of economically viable ore mineralizations enriched in rare earth elements (REE) (Allen et al., 1996; Einaudi et al., 1981). The olivine structure consists of two octahedral M1 (0.730 Å) and M2 (0.767 Å) sites with optimum ionic radii too small to incorporate REE cations (0.861-1.032 Å) at significant concentration levels (e.g., Zanetti et al., 2004). Therefore, fractionation and accumulation of olivine in primitive skarn environments can control the concentration and transport of REE in the ore-forming melts, responding to changes in olivine-melt partition coefficients (D_i expressed as ${}^{ol}C_i / {}^{melt}C_i$, where ${}^{ol}C_i$ is the concentration of a cation *i* in olivine and ${}^{melt}C_i$ is the concentration of *i* in the melt).

The purpose of this experimental study is to investigate the partitioning behavior of trivalent cations (R^{3+}) between olivine and melt during interaction of three different basalts (${}^{melt}Mg\#_{72}$, ${}^{melt}Mg\#_{75}$, and ${}^{melt}Mg\#_{78}$) with carbonate ($CaCO_3$) material. Following the previous work of Di

Stefano et al. (2018) on olivine-melt divalent cation partitioning as a function of $CaCO_3$ assimilation, the partition coefficients of REE, Y and Sc (D_{R3+}) have been also quantified and discussed in the framework of the lattice strain model of Blundy and Wood (1994), as well as charge-balancing mechanisms for heterovalent cation substitutions in olivine (Beattie, 1994; Purton et al., 1997; Colson et al., 1988, 1989; Nielsen et al., 1992; Zanetti et al., 2004; Evans et al., 2008; De Hoog et al., 2010; Grant and Wood, 2010; Sun and Liang, 2013). Results indicate that R^{3+} cations are less favorably incorporated into olivine crystallographic site with increasing $CaCO_3$ assimilation. The value of D_{R3+} is weakly dependent on temperature; the major control is exercised by olivine chemistry (forsterite and aluminium), and melt composition (CaO content) and structure (degree of depolymerization).

2. Methods

A detailed description of the experimental and analytical conditions used in this study can be found in Di Stefano et al. (2018). Here we report only the most important features of the experimental approach and analytical conditions.

The starting materials used for the experiments are three synthetic primitive basalts with different molar ratios of Mg to Mg + Fe: $^{melt}Mg\#_{72}$, $^{melt}Mg\#_{75}$, and $^{melt}Mg\#_{78}$ (Table 1S). These compositions were selected to reproduce natural magmas that may potentially assimilate great amounts of carbonate material (cf. Di Rocco et al., 2012; Gaeta et al., 2009). The basaltic powders were doped with 0, 10, and 20 wt.% $CaCO_3$, in order to obtain total CaO contents of ~11, ~16, and ~22 wt.%, respectively. The thermal decomposition of $CaCO_3$ at 1 atm releases all of the CO_2 gas, whereas in nature carbonate assimilation occurs at some pressure where CO_2 can be dissolved. Therefore, the addition of $CaCO_3$ to the starting material only changes the major element, not volatile content of the melts. This assumes that the olivine chemistry is not influenced by the concentration of CO_2 in the melt. However, the comparison between previous magma-$CaCO_3$ interaction experiments (Conte et al., 2009; Freda et al., 2008; Mollo et al., 2010; Mollo and Vona, 2014)

indicates that, under either CO_2-present or CO_2-absent conditions, the effect of volatile on melt and mineral chemistry is greatly minimized by the low solubility of CO_2 at shallow crustal conditions. The doping level of trace elements was designed to be comparable to that used by Grant and Wood (2010), so that total REE = 1,000 × chondritic values, Y = 200 ppm, and Sc = 50 ppm. The experimental olivines were equilibrated for 72 h at 1 atm, 1,150, 1,200 and 1,250 °C, and the QFM oxygen buffer. A sample chandelier has been used for the experiments holding several Pt-loops charged with the powdered starting material. The equilibrium temperature was measured by a Pt-$Pt_{90}Rh_{10}$ thermocouple located within 1 cm of the sample chandelier. The oxygen fugacity was controlled and monitored by two digital thermal mass flow meters for CO and CO_2 and an yttria-doped-zirconia solid electrolyte oxygen sensor ($SIRO_2$, Ceramic Oxide Fabricators, Ltd., Australia).

Major oxide analyses of the experiments were carried out with an electron microprobe, using 15 kV accelerating voltage and 10 nA beam current, 5 μm beam diameter and 20 s counting time, as reported in Di Stefano et al. (2018). For the purpose of this study, a 20 nA beam current has been adopted to analyze the relative low concentration of Al in olivine, following the same analytical approach of Evans et al. (2008). The analyses were standardized with jadeite (Si and Na), corundum (Al), forsterite (Mg), andradite (Fe), rutile (Ti), orthoclase (K), barite (Ba), apatite (P), and spessartine (Mn).

Trace element analyses were performed using a 193 nm excimer laser coupled with a second generation two-volume, constant geometry ablation cell and a high-sensitivity, sector-field inductively-coupled plasma mass spectrometer. Points with a spot size of 13 μm were set on chemically homogeneous portions of the material previously analyzed by electron microprobe, and ablated with a pulse rate of 10 Hz and energy density of 3.5 J/cm^3 for 40 s. Reference glass standards were NIST612 and GSD-1G, whereas ^{29}Si was used as internal standard for data reduction.

3. Results

Phase proportions and major oxide compositions from the experimental runs have been already documented in Di Stefano et al. (2018). The most important results can be summarized as follows (Table 1): 1) the experimental runs contain olivine, clinopyroxene, titanomagnetite, and glass in variable proportions as a function of *T*, ^{melt}Mg#, and $CaCO_3$, 2) olivine is the liquidus phase and its amount (~1-12 wt.%) increases with decreasing *T* and $CaCO_3$, and with increasing ^{melt}Mg#, and 3) olivine nucleates and grows as large and euhedral crystals with the c-axis length ranging from ~0.5 to ~3 mm.

3.1. Glass chemistry

As the experimental *T* is increased, the glass composition remains almost constant in terms of SiO_2, but $Na_2O + K_2O$ increases with the crystal content (Table 2S). In contrast, the assimilation of $CaCO_3$ greatly affects the glass composition, causing remarkable desilication (i.e., SiO_2 decreases from ~52 to ~43 wt.%) and decarbonation (i.e., CaO increases from ~11 to ~22 wt.%) phenomena. In the TAS (total alkali vs. silica; Le Bas et al., 1986) diagram, the glass is classified as basalt-basaltic andesite (from 0 to 10 wt.% $CaCO_3$) and basanite-tephrite (at 20 wt.% $CaCO_3$).

3.2. Olivine chemistry

When both *T* and ^{melt}Mg# decrease, the concentration of MgO in olivine decreases. Additionally, strong CaO enrichments occur with increasing $CaCO_3$ assimilation (Table 2S). Assuming simple solid solution of forsterite (i.e., Fo as Mg_2SiO_4) and fayalite (i.e., Fa as Fe_2SiO_4), the Fo content decreases from 93 to 87 as $CaCO_3$ increases from 0 to 20 wt.% (Table 2S). The maximum Fo_{93} content is measured for crystals formed from the most primitive $^{melt}Mg\#_{78}$ basalt assimilating 20 wt.% $CaCO_3$ at 1,250 °C. The simple structure of olivine and its small crystallographic sites may accommodate only a restricted number of R^{3+} cations that show concentrations from 0.01 to 3.9 ppm with decreasing cation radius (Table 2S). Light rare earth elements (LREE) are less favorably incorporated into the olivine crystal lattice with respect to heavy

rare elements (HREE). This observation extends also to the strong geochemical affinity of Y and Sc with HREE in olivine (Table 2S). The HREE/LREE signature of olivine is characterized by a typical highly fractionated pattern and the Lu/Sm ratio increases from 9 to 140 with increasing $CaCO_3$. Unfortunately, not all the trivalent cations were determined in our experiments. La, Ce, and, sometimes, Pr concentrations were below the detection limit of the LA-ICP-MS analysis (Table 2S).

3.3. Attainment of equilibrium

As documented by Di Stefano et al. (2018), the achievement of equilibrium crystallization is suggested by: 1) the experimental time duration of 72 h that is sufficient for basaltic melts to supply chemical nutrients to the growing crystals at equilibrium proportions (cf. Mollo et al., 2013a, 2013b), 2) the chemical homogeneity of glass and olivine, with a very limited scatter for replicated analyses (Tables 1S and 2S), 3) the Fe-Mg exchange between olivine and melt, yielding values (0.29-0.36) close to the equilibrium condition (0.33±0.04) established by Putirka (2016), and 4) the inter-experimental consistency of the measured partition coefficients, with systematic variations as a function of T, ^{melt}Mg#, and $CaCO_3$ assimilation.

3.4. Partitioning of R^{3+} cations

Partition coefficients of trivalent cations calculated by olivine and glass analyses are listed in Table 3S. Considering the difficulty of measuring very light REE concentrations in olivine, the missing values of D_{La}, D_{Ce}, and D_{Pr} have been extrapolated through the lattice strain equation of Blundy and Wood (1994). These data are also listed in Table 3S with an asterisk.

As a general rule, D_{R3+} decreases from 0.1 to 10^{-4} with cation radius (i.e., from D_{Sc} to D_{La}). D_Y is in between D_{Dy} and D_{Ho}, while D_{Sc} corresponds to the highest D_{R3+} (Table 3S). Our partition coefficients are very similar to those obtained by atmospheric pressure experiments conducted at 1,150-1,400 °C, air to QFM-13 buffering conditions, and using as starting materials either simplified

basaltic systems (e.g., CaO-MgO-Al_2O_3-SiO_2, i.e., CMAS) or basaltic to komatiitic melts (Beattie, 1994; Evans et al., 2008; Grant and Wood, 2010; Mallmann and O'Neill, 2009, 2013).

In Fig. 1, ln D_{R3+} is plotted versus the ionic radius of the trivalent cations assumed in six-fold coordination (data from Shannon, 1976). The regular relationship between the ionic radii of isovalent cations and the partition coefficients depicts a typical near-parabolic Onuma trend (Onuma et al., 1968). The good shape of the parabola evidences that the variation in partition coefficients is controlled by substitutions of R^{3+} onto well-defined crystallographic sites. D_{Sc} is always very close to the peak of the parabola, as its ionic radius matches well with the size of octahedral sites in olivine (Matsui et al., 1977). Notably, Sc is energetically most stable among the trivalent cations (Fig. 1), due to the similarity with Mg ionic radius (Blundy and Wood, 2003a; Evans et al., 2008). Overall, the value of D_{R3+} decreases with increasing $CaCO_3$ and this effect is more evident at lower ionic radii (Fig. 1). For this reason, the values of D_{LREE} sensibly overlap (Fig. 1), a feature likely addressed to the difficulty of measuring LREE concentrations in olivine.

Fig. 2 shows D_{Sc} and D_{Nd} variations as a function of T, ^{melt}Mg# and $CaCO_3$, assuming Sc and Nd as representative of R^{3+} cations with small and large ionic radii, respectively. The partitioning data slightly decrease with increasing T and ^{melt}Mg# (Fig. 2), but the most effective changes are caused by the addiction of $CaCO_3$ to the experimental charges. As a consequence, D_{Sc} and D_{Nd} are strongly anticorrelated with carbonate assimilation. The most important modifications occur for Sc, due to its smaller ionic radius with respect to other trivalent cations (Fig. 2).

4. Discussions

4.1. The lattice strain theory

The near-parabolic variation showed in the Onuma diagrams (Fig. 1) is the direct consequence of the crystal structure control (Matsui et al., 1977) and variation of the elastic strain energy in the crystal (e.g., Beattie, 1994; Nagasawa, 1966). The lattice strain model of Blundy and Wood (1994)

describes the mineral-melt partitioning of a trace element *i* of given ionic radius r_i through the Brice formulation (Brice, 1975):

$$D_i = D_0^{3+} \exp\left[\frac{-4\pi E N_A\left(\frac{r_0}{2}(r_i - r_0)^2 + \frac{1}{3}(r_i - r_0)^3\right)}{RT}\right] \quad (1)$$

Where N_A is Avogadro's number, R is the universal gas constant, and T is the temperature (in Kelvin). The partitioning of a substituent cation onto a structural site is related to the optimum site radius (r_0), its apparent Young modulus (E), and the strain-free (or strain-compensated) partition coefficient (D_0^{3+}) for a fictive cation with optimum radius for the given lattice site. To better understand the control of crystal composition and structure on the partitioning behavior of trivalent cations, D_{R3+} values were regressed according to the lattice strain equation. A Levenberg-Marquardt-type, non-linear least-squares fitting routine (Press et al., 1992) was employed to derive best-fit values of r_0, E and D_0^{3+}. The standard deviations of partition coefficients from Table 3S were used to weight the fits. The best-fit values for the lattice strain model parameters are listed in Table 2. Although olivine has two octahedral sites (M1 and M2), only one generic M site is used for fitting because M1 and M2 are sufficiently close in size and geometry to be fully disordered and to have almost comparable elastic properties (Beattie, 1994; Blundy and Wood, 2003a). According to Blundy and Wood (2003), the lattice strain equation allows prediction of partition coefficients for cations missing on the Onuma parabola (i.e., D_{La}, D_{Ce}, and D_{Pr} from Table 3S and Fig. 1). The method uncertainty is greatly minimized for the partitioning of trivalent cations, due to the fact that D_{REE} + D_Y + D_{Sc} can be treated as a single group in the lattice strain fit for olivine (Evans et al., 2008; Grant and Wood, 2010; Imai et al., 2012; Mallmann and O'Neill, 2013; Mibe et al., 2006; Sun and Liang, 2013, 2014). Non-

linear least squares fits of Eq. (1) show a very good agreement with the parabolic trends described by the partition coefficients (Fig. 1). This suggests that, during basalt-carbonate interaction, the incorporation of R^{3+} cations depends on the elastic response of the olivine crystal to strain, in accord with Eq. (1). However, as we will discuss below, the final value of D_{R3+} is also related to the composition and structure of the more depolymerized CaO-rich melt resulting from the assimilation of carbonate material.

4.1.1. Optimum ionic radius

At constant T and P, r_0 is univocally a property of the crystal and its variation is independent on the composition of the melt (Blundy and Wood, 1994). The optimum radius (0.714-0.727 Å; Table 2) derived by Eq. (1) indicates that R^{3+} are accommodated in the same crystallographic site of Mg (0.72 Å) in olivine (cf. Matsui et al., 1977). Our data are also comparable to those (0.70-0.73 Å) previously calculated by Blundy and Wood (2003a), Mibe et al. (2006) and Evans et al. (2008) under anhydrous and hydrous experimental conditions. The parameterization study of Sun and Liang (2013) reports a narrower range of 0.721-0.729 Å, consistent with r_0 from undoped basaltic experiments. However, basaltic compositions doped with 10 and 20 wt.% $CaCO_3$ deviate from this interval, yielding values (0.714-0.719 Å; Table 2) typical of Fo-rich olivines (Blundy and Wood, 2003a). It must be noted that Sun and Liang (2012, 2013) demonstrated as a broader range of r_0 is likely an artifact of non-linear regression analysis caused by the strong trade-off between E and r_0. Therefore, it has been verified whether the lattice strain parameters are indeed independent or, alternatively, there is multicollinearity between E and r_0. The variance inflation factor (VIF) has been used as statistic test. This parameter indicates how much the variance of a coefficient is inflated due to linear dependence with other predictors. Results from calculations provide VIF = 17.8, greatly exceeding the threshold value of 10 regarded as indicating multicollinearity (Hair Jr. et al., 1995). In Fig. 3a, r_0 is plotted versus Mg, Fe, and Ca cations in olivine. Through multiple regression analysis and the

standardized regression coefficient, it has been determined the statistical influence of Mg, Fe and Ca in the crystal (as independent variables) on r_0 (as dependent variable). The standardized regression coefficient is equal to the original unstandardized regression coefficient of each independent variable, multiplied by the standard deviation of the independent variable and divided by the standard deviation of the dependent variable. Results from calculations highlight that the influence of Fe (18%) and Ca (16%) on r0 is relatively low (Fig. 3a). In contrast, Mg (67%) is the most influencing cation (Fig. 3a) for R^{3+} substitution in octahedral sites, making r_0 smaller (Grant and Wood, 2010; Purton et al., 1997). Variations of r_0 are also quantitatively consistent with changes in cation-oxygen bond lengths in olivine (Bottazzi et al., 1999; Tiepolo et al., 1998; Wood and Blundy, 1997; Zanetti et al., 2004). For example, the cation-oxygen distance in the M site decreases with increasing forsterite (Hazen, 1976; Imai et al., 2012), a feature well reproduced by r_0 variations from this study (Table 2). Similarly, Blundy and Wood (2003a) noted that r_0 slightly increases with increasing Fe in olivine (Fig. 3a), in agreement with the longer cation-oxygen bond distance of fayalite (2.17 Å) relative to forsterite (2.11 Å). Despite the fact that Mg dominates all other divalent cations and is accommodated in both M1 and M2 sites, Fe is preferentially ordered in M2 at magmatic temperatures (Heinemann et al., 1999). This causes distortion of the octahedra as the larger Fe cations substitute for Mg (Papike et al., 2005). Moreover, during assimilation of $CaCO_3$ by basaltic melts, the amount of larger Ca cations in olivine increases (Table 2S). A such incorporation mechanism is restricted to only the larger M2 site and takes place by Ca-Fe substitutions (Adams and Bishop, 1985; Coogan et al., 2005; Warner and Luth, 1973). As a consequence, the accommodation of Ca into the expanded M2 site is essentially counterbalanced by the increasing number of Mg cations entering into the small M1 site (Fig. 3a), also in response to its shorter cation-oxygen bond length (cf. Jurewicz and Watson, 1988; Libourel, 1999; Snyder and Carmichael, 1992). Coherently, at constant temperature, the value of D_{Ca}^{2+} is documented to linearly increase as the amount of Fo in olivine decreases (Di Stefano et al., 2018; Jurewicz and Watson, 1988; Libourel, 1999; Snyder and Carmichael, 1992; Toplis and Carroll, 1995).

4.1.2. Apparent Young modulus

The Young modulus controls the tightness of the partitioning parabola and is a measure of the crystal site elasticity (i.e., the stiffness of the bond between the cation and surrounding anions; Wood and Blundy, 1997). *E* changes as a function of the type of substituting cation and the geometry of the site itself. Values calculated from this study slightly decrease from 438 to 411 GPa (Table 2S) with increasing $CaCO_3$ assimilation. This causes the parabola to become less tight (Fig. 1) and the incorporation of R^{3+} cations in the octahedral site occurs with lower strain (i.e., the elasticity of the polyhedron increases). Our data are higher than the best fitting value (360 GPa) proposed by Wood and Blundy (2003) and lower than the range (513-703 GPa) derived at high pressures (1.4-10 GPa; Zanetti et al., 2004; Mibe et al., 2006; Imai et al., 2012). Generally, we observe a fairly good agreement with the range (429-455 GPa) calculated by Sun and Liang (2013), denoting a more elastic octahedral site at atmospheric pressure. Notably, there is no marked relationship between *E* and Mg or Fe (Fig. 3b), as well as no colinearity ($R^2 = 0.02$) is found between *E* and r_0 when the experimental parameters are regressed against each other. In contrast, *E* is strongly correlated and influenced (87%) by Ca (Fig. 3b), due to a more elastic response of the crystal lattice to large cation incorporation (Zanetti et al., 2004). Additionally, the apparent site elasticity scales with the ratio of Z/d^3 (Wood and Blundy, 2003), where Z is the ionic charge and d is the cation-oxygen bond length at the site of interest, given as r_0 + 1.38 Å (i.e., the radius of O_2- anions in four-fold coordination). Wood and Blundy (2003) modeled the variations in *E* for different minerals (e.g., olivine, clinopyroxene, plagioclase, etc.) as a function of Z/d^3 for binary oxides. In our experiments, Z/d^3 slightly increases from 0.320 to 0.327 Å - 3 with increasing Ca in olivine. This range is higher than the threshold value of 0.3 Å - 3 at which the lattice site is stiffer than binary oxides (Wood and Blundy, 2003). Therefore, it is confirmed that small lattice sites are more resistant to the accommodation of R^{3+} and highly charged cations, even with small size misfits.

During cation partitioning between olivine and melt, Bédard (2005) and Evans et al. (2008) observed that E (and D_0^{3+}) can be modeled as a linear function of MgO and SiO_2 in the melt, respectively. However, these single melt components are weakly correlated with E during basalt-carbonate interaction, accounting for the dominant effect of CaO produced by carbonate thermal decomposition (see below). Bearing this in mind, we have refitted the values of E with the activity of calcium in the melt (i.e., ${}^{melt}a_{CaO} = {}^{melt}X_{CaO} / {}^{melt}X_{SiO2}$, where ${}^{melt}X_i$ is the molar fraction of the element i in the melt; see Di Stefano et al., 2018 for further details). The correlation coefficient (R^2 = 0.85) of the regression fit is very similar to that (R^2 = 0.87) derived for Ca in olivine. Possibly, during basalt-carbonate interaction, the melt and crystal compositions exercise a comparable influence on the Young modulus. Decarbonation and desilication phenomena cause that SiO_2-poor, CaO-rich melts coexist with Ca-bearing olivines (Tables 1S and 2S), as widely documented for primitive skarn systems (Conte et al., 2009; Di Rocco et al., 2012; Gaeta et al., 2009; Gozzi et al., 2014; Mollo et al., 2010; Mollo and Vona, 2014; Wenzel et al., 2002). This is due to the fact that Ca entering olivine is proportional to the number of Si and Ca cations available in the melt structure (Libourel, 1999; Libourel et al., 1989; Shi, 1993; Shi and Libourel, 1991). Under such circumstances, the variation of D_{Ca}^{2+} is approximated as a linear function of Ca in the melt (Di Stefano et al., 2018; Jurewicz and Watson, 1988; Watson, 1979).

4.1.3. Strain-free partition coefficient

According to the lattice strain theory, the peak of the Onuma parabola matches with the strain-free partition coefficient centered at the optimum radius of the lattice site of the host mineral (Fig. 1). Fig. 4 shows that D_0^{3+} is practically independent on 1/T, suggesting negligible effects of the positive entropy of fusion of olivine on R^{3+} partitioning (Blundy and Wood, 1994; Wood and Blundy, 1997). Apparently, the effect of T is more a measure of the bulk chemistry of the system, such as the variations of Fo in olivine and MgO in the melt (Colson et al., 1988, 1989; Nielsen et al., 1992; Evans

et al., 2008; Wang and Gaetani, 2008; Grant and Wood, 2010; Imai et al., 2012; Sun and Liang, 2013). Olivine and melt compositions are inextricably interrelated in our experiments. For example, in terms of the equilibrium Fe-Mg exchange reaction, the Mg/Fe ratio of olivine increases with increasing the MgO/FeO ratio of the melt (see data in Tables 1S and 2S), thus enhancing the amount Fo component in olivine (cf. Roeder and Emslie, 1970).

The effect of melt composition and structure on D_0^{3+} is presented in Fig. 4. Differently from previous observations for uncontaminated basaltic melts (Bédard, 2005), our decarbonation experiments show that MgO in the melt is poorly correlated with D_0^{3+}, exercising a minimum influence of 4% on R^{3+} partitioning (Fig. 4). As reported in Di Stefano et al. (2018), the effect of Mg on the melt structure is always subordinate to that of Ca during basalt-carbonate interaction. The content of MgO in the melt changes by only ~20% with increasing $CaCO_3$, whereas CaO shows a marked increase of ~50% (Table 1S). In a simplified CMAS system, Evans et al. (2008) found a strong inverse correlation between D_0^{3+} and ${}^{melt}X_{SiO2}$ (where the mole fraction is calculated on a single cation basis), denoting that the effects of *P*, *T* and olivine chemistry may be secondary or implicitly incorporated in the melt composition. Intriguingly, in our decarbonation experiments, D_0^{3+} increases as a function of ${}^{melt}X_{SiO2}$ (Fig. 4), depicting an opposite trajectory relative to that found by Evans et al. (2008). This effect is attributed to the strong increase of ${}^{melt}a_{CaO}$ with CaCO3 assimilation, implying that the control of ${}^{melt}a_{SiO2}$ on D_0^{3+} is subordinate to the increasing amount of Ca in the melt (Di Stefano et al., 2018; Ferguson, 1978; Libourel, 1999). Moreover, Sun and Liang (2013) noted that the abundance of Al in olivine is proportional to the Al content of the melt, so that D_0^{3+} can be parameterized by using ${}^{melt}X_{Al2O3}$ (Fig. 4). Since both SiO_2 and Al_2O_3 in the melt decrease by the same magnitude (~18%) during $CaCO_3$ assimilation, the influence imparted by either ${}^{melt}X_{SiO2}$ (14%) or ${}^{melt}X_{Al2O3}$ (13%) on the strain-free partition coefficient is almost the same. This feature is very similar to the observation that the Al~~2~~O~~3~~/SiO~~2~~ ratio of the melt is proportional to the incorporation

of Al in clinopyroxene during assimilation of either carbonate (Mollo and Vona, 2014) and siliceous (Mollo et al., 2017) crust by basaltic magmas.

From the point of view of the melt structure, the assimilation of $CaCO_3$ lowers the number of bridging oxygens (i.e., BO, oxygens bonded to two tetrahedrally coordinated cations) relative to that of non-bridging oxygens (i.e., NBO, oxygens bonded to a tetrahedrally coordinated cation and to a different cation in another coordination state). As a consequence, the silica network of BO (Si-O-Si) bonds is disrupted by Ca addition, forming NBO (Si-O-Ca) bonds in more depolymerized melts (Kohn and Schofield, 1994; Lee and Stebbins, 2003; Leeman, 1978; Libourel, 1999; Shi and Libourel, 1991). The value of NBO/T (i.e., the number of NBO per tetrahedrally coordinated cations T) is a fairly good expression of the melt structure (Mysen et al., 1985). Fig. 4 shows that both ${}^{melt}X_{CaO}$ and NBO/T exercise a similar influence (33-34%) on D_0^{3+}. The strong depolymerizing effect of Ca increases remarkably the proportion of octahedral relative to tetrahedral sites in the melt, as well as the number of structural sites critically important to accommodating large cations in the structure (O'Neill and Eggins, 2002). In analogy with clinopyroxene, the melt structure may control the mineral/melt cation partitioning, especially when NBO/T is less than the threshold value of 0.4 (Gaetani, 2004; Huang et al., 2006; Mollo et al., 2016; Qian et al., 2015). In the case of olivine, Wang and Gaetani (2008) noted that the dependence of cation partitioning on melt composition becomes more effective at NBO/T < 0.6. Despite our melt compositions yield NBO/T values comprised between ~0.7 and ~1.4, it is apparent from Fig. 4 that D_0^{3+} cannot be interpreted as independent of melt structure under open-system conditions (e.g., magma-carbonate interaction). Rationally, changes of D_0^{3+} reflect the combined effects of crystal chemistry (Fig. 1) and melt structure (Fig. 4) on the partitioning of trivalent cations. This also agrees with the close interplay found between major and trace element cation proportions in olivine and the concentration of SiO_2 (Evans et al., 2008; Longhi et al., 1978; Toplis, 2005), MgO (Beattie, 1993; Kohn and Schofield, 1994; Bédard 2005; Putirka et al., 2007; Pu et al., 2017), CaO (Di Stefano et al., 2018; Leeman, 1978; Libourel, 1999; Libourel et

al., 1989; Shi, 1993; Shi and Libourel, 1991) and Al_2O_3 (Beattie, 1994; De Hoog et al., 2010; Sun and Liang, 2013) in the melt. Most major and trace elements are network-modifiers in silicate melts, forming NBO in the Q_n-species (i.e., individual structure of oxygen tetrahedra surrounding a central, tetrahedrally-coordinated cation; Mysen et al., 1982). The distribution of Q_n-species in the melt is governed by the equilibrium reaction: $2Q_n = Q_{n-1} + Q_{n+1}$ (where n is the number of BO). The reaction shifts to the right as the charge density (i.e., the ratio between the cation charge and ionic radius) of the network modifying cations increases (Maekawa et al., 1991; Mysen, 2004). For cations with high charge density (i.e., REE, Y, and Sc), there is an increasing availability of NBO to form the cation-oxygen polyhedra in the silicate melt (Ryerson and Hess, 1978; Watson, 1976). Thus, the solubility of R^{3+} cations in the melt increases with increasing $CaCO_3$ assimilation (Di Stefano, 2018), in concert with the enhanced activity of NBO (Mysen and Virgo, 1980; Ryerson and Hess, 1978; Watson, 1976). Under such circumstances, the concentration of Q_n-species roughly scales with NBO/T (Fig. 4), influencing remarkably the value of D_0^{3+} (cf. Kohn and Schofield, 1994; Mysen, 2004; Mysen et al., 1982; Mysen and Virgo, 1980; Putirka et al., 2007; Wang and Gaetani, 2008; Watson, 1977).

4.2. Substitution mechanisms for trivalent cations in olivine

The systematic alignment of D_{R3+} along the Onuma parabola (Fig. 1) is a clear indication that the substitution of R^{3+} into the octahedral crystal site is controlled by olivine composition (cf. Brice, 1975). Sun and Liang (2013) have demonstrated that Fo and Al contents in olivine are the primary compositional variables in determining the strain-free partition coefficient. To evaluate and quantify the control of these variables on D_0^{3+} during basalt-carbonate interaction, data from these studies have been compared with those from the parameterized lattice strain model of Sun and Liang (2013). In Fig. 5a, values of D_0^{3+} predicted by the model are plotted versus those measured during basalt-carbonate interaction. As a first approximation, all data from this study fall between the 1:2 and 2:1 correlation lines constraining the calibration error of the model. The regression analysis of measured

vs. predicted values of D_0^{3+} yields a high correlation coefficient ($R^2 = 0.93$) and a relative low standard error of estimate (SEE = 0.009). The value of SEE also decreases down to 0.007, by excluding the experiments assimilating 20 wt.% $CaCO_3$ and outside the calibration dataset of Sun and Liang (2013). Due to the trade-offs among D_0^{3+}, E and r_0 a more appropriate comparison is D_{Sc} from this study vs. D_{Sc} model of Sun and Liang (2013), by assuming Sc as a proxy for the overall incorporation of REE in olivine. Results still indicate very good regression statistics ($R^2 = 0.87$ and SEE = 0.008), also confirming that Fo (Fig. 5b) and Al (Fig. 5c) contents in olivine are an excellent proxy for the partitioning behavior of trivalent cations. Moreover, the parameterized lattice strain model of Sun and Liang (2013) can be realistically extrapolated to a broad range of olivine and melt compositions, such as those resulting from magma decarbonation phenomena. Notably, uncontaminated basaltic compositions closely align along the 1:1 line, whereas moderate deviations occur as a function of carbonate assimilation. As a whole, D_0^{3+} is always negatively correlated with Fo (Fig. 5b) and positively correlated with Al (Fig. 5c) in olivine, in agreement with the calibration dataset used by Sun and Liang, 2013.With increasing CaO in the melt, the incorporation of large Ca cations into olivine crystal structure increases via progressive Ca-Fe substitutions (Adams and Bishop, 1985; Jurewicz and Watson, 1988; Libourel, 1999; Snyder and Carmichael, 1992; Toplis and Carroll, 1995; Warner and Luth, 1973). As a consequence, the amount of Fo increases during basalt-carbonate interaction, thus controlling the value of D_0^{3+} (Fig. 5b). On the other hand, the strong influence (61%) exercised by Al in olivine on D_0^{3+} (Fig. 5c) is addressed to more complex and still debated substitution mechanisms (cf. Beattie, 1993; Colson et al., 1988, 1989; Nielsen et al., 1992; Suzuki and Akaogi, 1995; Purton et al., 1997; Taura et al., 1998; Evans et al., 2008; Wan et al., 2008; De Hoog et al., 2010; Grant and Wood, 2010; Imai et al., 2012). The comparative studies of Taura et al. (1998) and Grant and Wood (2010) have demonstrated that substitution of Al with Na is not important for the incorporation of Al into olivine at low pressure conditions. The composition of natural olivines can be likely explained by the uptake of Al through a Tschermak-style substitution of the type (^{M}Mg, ^{T}Si)

↔ (^{M}Al, ^{T}Al) (De Hoog et al., 2010; Grant and Wood, 2010). This mechanism is also facilitated by the ionic radius of Al, being roughly in-between those of Si and Mg. Evans et al. (2008) quantified the Tschermak-style substitution through the stoichiometric reaction: $^{melt}(AlO_{1.5}) + {}^{ol}(0.25Mg_2SiO_4) = {}^{ol}(0.5MgAl_2O_4) + {}^{melt}(0.25SiO_2)$. Following the same approach used by Evans et al. (2008), we have tested the proportionality between $^{ol}[(Al)^{0.5}]$ expressed in ppm and $^{melt}[X_{AlO1.5}/(X_{SiO2}{}^{0.25})]$. In particular, the regression fit (R^2 = 0.90) denotes a fairly good stoichiometric control of melt components on the incorporation of Al in olivine (Fig. 6a). Moreover, the calibration data of Sun and Liang (2013), including also the experiments of Evans et al. (2008), reproduce well the trend depicted by our experiments, although more scatter is evident (Fig. 6a). This provides also an explanation for the fact that D_0^{3+} can be reliably estimated by both Al-in-melt or Al-in-olivine models, in agreement with the parameterization approach proposed by Sun and Liang (2013). Notably, for the case of Al-in-melt model, the regression analysis of measured vs. predicted values of D_0^{3+} recovers a standard error of estimate (SEE = 0.007) very close to that measured by the Al-in-olivine parameterization. During (^{M}Mg, ^{T}Si) ↔ (^{M}Al, ^{T}Al) substitution, it is also possible that Al occupancy occurs prevalently (but not exclusively) at the M site rather than T site. Suzuki and Akaogi (1995) have illustrated that most of the Al cations are placed in the octahedral site of olivine structure during crystallization from more depolymerized melts. Blundy and Wood (2003a) observed that the total content of Al may be included in the fitting of R^{3+} in the octahedral site to better resolve the lattice strain parameters at low ionic radii. Similarly, Sun and Liang (2013) noted that D_{Al} frequently lies on the same Onuma parabola of D_{R3+}. This may reflect some poorly studied charge-balance mechanisms that account for the effect of other cations in olivine structure. For example, modeling data from Zanetti et al. (2004) have evidenced some important Al and Ti site preferences in olivine, showing ^{M}Al occupancies of 79-90% and 89-100% when Ti is ordered at M and T sites, respectively.

During olivine crystallization, the isolated effect of crystal or melt composition on D_{R3+} is difficult to identify when both these parameters change at the same time and are convoluted with the

effect of temperature (e.g., Sun and Liang, 2013). This is especially true for the complex charge-balance mechanisms that control the incorporation and substitution of trace elements in olivine. Generally, R^{3+} cations replace Mg in olivine by 1) cation vacancies [i.e., ($3^{M}Mg$) ↔ ($2^{M}Mg$, ^{M}V)], 2) coupled substitution of Al for Si in tetrahedral site [i.e., (^{M}Mg, ^{T}Si) ↔ ($^{M}R^{3+}$, ^{T}Al)], and 3) coupled substitution of Na or Li for Mg in octahedral sites [i.e., (^{M}Mg, ^{M}Mg) ↔ ($^{M}R^{3+}$, ^{M}Na or ^{M}Li)] (Beattie, 1994; Purton et al., 1997; Colson et al., 1988, 1989; Nielsen et al., 1992; Zanetti et al., 2004; Evans et al., 2008; De Hoog et al., 2010; Grant and Wood, 2010). As demonstrated by Grant and Wood (2010), the charge-compensating mechanisms that govern the incorporation of R^{3+} in olivine can be effectively understood only by experiments conducted at fixed *T* and *P*, and fixed major element compositions of olivine and melt. According to this premise, it is apparent that decarbonation experiments from this study were not designed to unequivocally isolate the effect of olivine and melt compositions on D_{R3+}. However, assuming Sc as a proxy for the partitioning behavior of all R^{3+} cations, some potential substitution mechanisms can be tested (cf. Colson et al., 1988, 1989). In fact, Sc occupies a site in the crystal and melt similar to Mg, so that all cations with different charges need to be balanced by coupled substitution of other cations or vacancies (De Hoog et al., 2010). At relative high pressure conditions (i.e., 3-14 GPa), Na incorporates into olivine in association with Sc (Imai et al., 2012; Taura et al., 1998). Conversely, in Li-bearing melts, Li is the charge-balancing alkali metal cation at atmospheric pressure (Grant and Wood, 2010; Purton et al., 1997; Suzuki and Akaogi, 1995). Since natural olivines have sufficient Al to charge-balance Sc, Beattie (1994) postulated that maintenance of local charge-balance can be preserved by the coupled substitution (^{M}Mg, ^{T}Si) ↔ ($^{M}R^{3+}$, ^{T}Al). However, a great number of further studies have demonstrated that this charge-balance reaction does not effectively control the incorporation of Sc in the octahedral site (Colson et al., 1988, 1989; Nielsen et al., 1992; Evans et al., 2008; De Hoog et al., 2010; Grant and Wood, 2010). While Al enters the crystal lattice by a Tschermak-style substitution (Fig. 6a), the charge balance for R^{3+} cations is maintained by vacancies in the octahedral sites, with complete occupancy of the tetrahedral site by Si. The vacancy reaction ($3^{M}Mg$) ↔ ($2^{M}Mg$, ^{M}V) applies well either to Al-poor olivines (Al_2O_3

≤ 0.1 wt.%) where the concentration of Al is too low to charge-balance Sc (Colson et al., 1988, 1989; Nielsen et al., 1992), or to Al-rich olivines (Al_2O_3 > 0.1 wt.%) where Sc replaces Mg by compensating vacancy (Evans et al., 2008; Grant and Wood, 2010). In terms of cation molar fractions, the total R^{3+} ($X_{\Sigma R3+}$) and Al (X_{Al}) contents in experimental olivines from this study do not change at the same rate as a function of $CaCO_3$ assimilation. Within the investigated temperature (1,150-1,250 °C) and melt compositional ranges ($^{melt}Mg\#_{72\text{-}78}$), $X_{\Sigma R3+}$ decreases by 9-21% as $CaCO_3$ increases from 0 to 20 wt.%, whereas X_{Al} dramatically decreases by 75-81% (Table 2S). The substantial decrease of Al points towards a mechanism independent of the simple charge balance (^{M}Mg, ^{T}Si) ↔ ($^{M}R^{3+}$, ^{T}Al) but, rather, related to the Tschermak-style substitution (Fig. 6a). More specifically, Grant and Wood (2010) designed a set of experiments to investigate this phenomenon using a simplified diopside-forsterite (Di_{75}-Fo_{25}) melt doped with similar concentrations of Sc, but concentrations of Al spanning several orders of magnitude (from 0 to 70,000 ppm). It was observed that, at 1,390 °C and 1 atm, differences between D_{Sc} in Al-rich and Al-poor forsterite crystals are negligible, indicating that the charge balance (^{M}Mg, ^{T}Si) ↔ (MR^{3+}, ^{T}Al) is unimportant as a mechanism for Sc incorporation. Furthermore, Grant and Wood (2010) derived several thermodynamic equations describing how charge neutrality-maintaining defects take place when R^{3+} cations are incorporated into pure forsterite. By solving the vacancy reaction ($3^{M}Mg$) ↔ ($2^{M}R^{3+}$, ^{M}V), it was found that DSc scales with $^{melt}[1/(Sc)0.33]$ expressed in ppm, for a paired substitution of Sc and a vacancy for Mg in octahedral sites (Fig. 6b). When D_{Sc} values from Grant and Wood (2010) are compared with those from this study, two distinct trajectories are observed accounting for the different bulk compositions of the experiments. However, in both cases, $\ln D_{Sc}$ is highly correlated (R^2 = 0.97) with $^{melt}[1/(Sc)0.33]$, attesting that the incorporation of R^{3+} cations is preferentially controlled by charge-balancing Mg vacancies (Fig. 6b). Indeed, during magma-carbonate interaction, the accommodation of Ca in M2 site is counterbalanced by the increasing number of Mg cations in M1 site (Adams and Bishop, 1985; Di Stefano et al., 2018; Jurewicz and Watson, 1988; Libourel, 1999; Snyder and Carmichael, 1992;

Warner and Luth, 1973). This cation exchange leads to the crystallization of Fo-CaO-rich olivine phenocrysts from more depolymerized melts by 1) lowering the number of coupled substitutions (^{M}Mg, ^{T}Si) ↔ (^{M}Al, ^{T}Al) for the uptake of Al in excess (De Hoog et al., 2010; Evans et al., 2008) and 2) limiting the efficacy of the vacancy reaction (3^{M}Mg) ↔ (2^{M}Mg, ^{M}V) for the entry of R^{3+} cations in M sites (Colson et al., 1988, 1989; Nielsen et al., 1992; Grant and Wood, 2010). Therefore, the overall positive correlation between D_0^{3+} and Al (Fig. 5c) reflects an apparent relationship due to the concurrent incorporation of R^{3+} and Al cations in olivine with decreasing Fo and CaO (Colson et al., 1988, 1989; Nielsen et al., 1992; Evans et al., 2008; De Hoog et al., 2010; Grant and Wood, 2010). Given this correlation, either the concentration of Al_2O_3 in olivine or the concentration Al_2O_3 in the melt can be successfully used in the parameterization of D_0^{3+} (cf. Sun and Liang, 2013).

If natural olivines have sufficient Al to charge-balance Sc, maintenance of local charge-balance is apparently preserved by the reaction (Beattie, 1994):

$$^{ol}[MgMgSiO_4]+^{melt}[Sc]+^{melt}[Al]\leftrightarrow^{ol}[MgScAlO_4]+^{melt}[Si] \quad (2)$$

In contrast, the exchange reactions for the vacancy-coupled substitution can be written as (Colson et al., 1989):

$$^{ol}[5/4(MgMgSiO_4)]+^{melt}[Sc]\leftrightarrow^{ol}[5/4(Mg_{4/5}Sc_{4/5}V_{2/5}SiO_4)]+^{melt}[3/2(Mg)] \quad (3)$$

The charge-balanced reaction (3) can be further modified in two vacancy reactions for the M1 and M2 sites (cf. Evans et al., 2008):

$$^{ol}[MgMgSiO_4]+^{melt}[Sc]\leftrightarrow^{ol}[Mg_{1/2}ScV_{1/2}SiO_4]+^{melt}[1/2(Mg)] \quad (4)$$

and

$$^{ol}[3/2(MgMgSiO_4)]+^{melt}[Sc]\leftrightarrow{}^{ol}[3/2(MgSc_{2/3}V_{1/2}SiO_4)]+^{melt}[3/2(Mg)] \quad (5)$$

The activities of crystal components are defined by the following expressions (Kerrick and Darken, 1975; Colson et al., 1988, 1989):

$$^{ol}a_{MgMgSiO4} = {}^{ol}[(Fo)^2] \quad (6)$$

$$^{ol}a_{MgScAlO4} = {}^{ol}[Fo] \times {}^{ol}[X_{Sc}/(X_{Mg}+X_{Fe}+X_{Sc})] \quad (7)$$

$$^{ol}a_{Mg4/5Sc4/5V2/5SiO4} = {}^{ol}[(Fo)^{4/5}]\times{}^{ol}[(X_{Sc}/(X_{Mg}+X_{Fe}+X_{Sc}))^{4/5}] \quad (8)$$

$$^{ol}a_{Mg1/2ScV1/2SiO4} = {}^{ol}[(Fo)^{1/2}]\times{}^{ol}[X_{Sc}/(X_{Mg}+X_{Fe}+X_{Sc})] \quad (9)$$

$$^{ol}a_{MgSc2/3V1/2SiO4} = {}^{ol}[Fo]\times{}^{ol}[(X_{Sc}/(X_{Mg}+X_{Fe}+X_{Sc}))^{2/3}] \quad (10)$$

To solve Eqs. (2), (3), (4), and (5), the activity of Sc in the melt is calculated according to the two-lattice melt model of Nielsen and Drake (1979) and Nielsen and Dungan (1983):

$$^{melt}a_{Sc} = {}^{melt}[X_{Sc}]/{}^{melt}[\sum X_{NM}] \quad (11)$$

The melt is assumed as two-independent quasi-lattices formed by Si, NaAl, and KAl as network-formers (NF), and Ca, Mg, Fe, excess of Al, Cr, and Ti as network-modifiers (NM). ΣX_{NM} is the sum of the network-modifiers (i.e., X_{Al2O3}, X_{CaO}, X_{MgO}, X_{FeO}, X_{TiO2}) minus a portion of the network-formers (i.e., X_{Na2O} and X_{K2O}). In Fig. 7, ${}^{melt}a_{Sc2O3}$ is plotted versus ${}^{ol}a_{Mg4/5Sc4/5V2/5SiO4}$, ${}^{ol}a_{Mg1/2ScV1/2SiO4}$, ${}^{ol}a_{MgSc2/3V1/2SiO4}$, and ${}^{ol}a_{MgScAlO4}$ from vacancy and charge-balance exchange reactions. According to multiple regression analysis, Eq. (3) greatly influences (49%) the accommodation of Sc in olivine (Fig. 7), in agreement with what was demonstrated by Grant and Wood (2010). The same applies to the cumulative influence (50%) exercised by Eqs. (4) and (5), accounting for Mg vacancies ordered in M1 and M2 sites, respectively (cf. Evans et al., 2008). In contrast, Sc incorporation in octahedral sites is not charge-balanced by substitution of Al for Si (Fig. 7), due to the negligible control (1%) of Eq. (2). For the sake of completeness, multiple regression analyses for Sc have been also extended to REE and Y activities in olivine and melt. As illustrated in the histogram showed in Fig. 8, the coupled substitution (^{M}Mg, ^{T}Si) ↔ ($^{M}R^{3+}$, ^{T}Al) is always unimportant with respect to the vacancy reaction (3^{M}Mg) ↔ (2^{M}Mg, ^{M}V). This matches the observation that the defect energies in M1 and M2 sites show unfavorable solution energies for Al compensation (Purton et al., 1997) and maintenance of local charge-balance requires formation of magnesium vacancies or some other defects (Colson et al., 1989; Evans et al., 2008; Grant and Wood, 2010). It is also not excluded that the olivine crystal lattice may become more distorted as the number of Sc cations and vacancies increases, thus allowing more Sc and vacancies to be accommodated (cf. Nielsen et al., 1992).

5. Implications for the geochemical evolution of magmas at the Colli Albani Volcanic District

The Colli Albani Volcanic District (central Italy) is characterized by silica-undersaturated ultrapotassic compositions ranging from tephrite to foidite (leucitite) and tephriphonolite (Dallai et al., 2004; Gaeta et al., 2006, 2011; Gozzi et al., 2014). The occurrence of skarn ejecta in the pyroclastic products testifies to strong interaction of magmas with carbonate host rocks (Di Rocco et

al., 2012; Gaeta et al., 2009). This contamination process is more effective at the periphery of magma chamber, with formation of endoskarns (or magmatic skarns) and cumulates of olivine and clinopyroxene. In Fig. 9, the Sc vs. CaO diagram shows the evolutionary path of melt inclusions in olivine phenocrysts from endoskarns and cumulates (cf. Di Rocco et al., 2012; Gaeta et al., 2009). Using a primitive melt inclusion (Sc = 12.09 ppm and CaO = 12.28 wt.%) as starting composition, assimilation and fractional crystallization (AFC) paths are modeled. The partition coefficients selected for the calculations are $D_{Sc}^{ol-melt}$ = 0.11 (i.e., 20 wt.% $CaCO_3$ assimilation from this study) and $D_{Sc}^{cpx-melt}$ = 12.24 estimated with the lattice strain model of Wood and Blundy (1997), using as input data clinopyroxene-melt pairs from Di Rocco et al. (2012). The CaO content of the assimilant is set to 45 wt.%, in agreement with the thermal decomposition of $CaCO_3$ (Mollo et al., 2013a). The AFC1 trajectory is derived by fractionating only ~15% of olivine. Conversely, the AFC2 trajectory accounts for olivine and clinopyroxene fractionation in 76:24 relative proportions, for ~13% of total solid amount. The ratio of the assimilation rate to the crystallization rate ranges from 0.01 to 0.2 (see Di Stefano et al., 2018 for further details). The AFC1 trajectory shows that the trace element content in melt inclusions from cumulates is controlled by olivine segregation, causing strong Sc enrichments in the more differentiated melts. The effect of carbonate assimilation on melt composition is generally weak and associated with an increase of CaO from ~12 to ~17 wt.% (Di Stefano et al., 2018). In contrast, the AFC2 trajectory indicates that endoskarns are greatly influenced by carbonate assimilation, leading to CaO enrichments in melt inclusions up to ~25 wt.%. The assimilation of carbonate by magmas enlarges the stability field of clinopyroxene (Carter and Dasgupta, 2015, 2018; Mollo et al., 2010; Mollo and Vona, 2014) that, in turn, determines the formation of residual melts dramatically depleted in Sc. This finding points out that cumulate rocks are typical of high-temperature, primitive systems where olivine is energetically more favored than clinopyroxene, whereas endoskarns represent low-temperature, highly decarbonated natural environments dominated by clinopyroxene crystallization. According to Gaeta et al. (2009) and Di Rocco et al. (2012), the

accumulation of olivine is determined by the development of a high-temperature solidification front at the carbonate wall-rocks. This phenomenon takes places at the very beginning of magma-carbonate interaction, just before the endoskarn formation. Subsequently, the migration of CaO-rich melts from the endoskarn domain favors the crystallization of clinopyroxene, thus depleting the REE from the melt and limiting further enrichments of these trace elements (Di Rocco et al., 2012; Gaeta et al., 2009). As a consequence, in primitive systems contaminated by carbonate material, the remobilization of crystal cumulates or crystal slurries have potential important implications in the genesis of REE-bearing deposits (e.g., Hayes et al., 2015 and references therein).

6. Conclusions

The partitioning behavior of REE, Y and Sc between olivine and melt has been investigated through basalt-carbonate interaction experiments. Results have been interpreted in the framework of the lattice strain theory (i.e., r_0, E, and D_0^{3+}) and the following conclusions have been reached:

1) changes in r_0 are determined by the accommodation of Ca into the more distorted M2 site of olivine, counterbalanced by the increasing number of Mg cations entering into the smaller M1 site;
2) the value of E is anticorrelated with either Ca in olivine or the activity of CaO in the melt, in accord with the finding that Ca entering olivine is proportional to the number of Ca atoms available in the melt structure;
3) ${}^{melt}X_{CaO}$ and NBO/T significantly influence D_0^{3+}, due to the increased solubility of network-modifying trivalent cations in more depolymerized SiO_2-poor, CaO-rich melts;
4) the strain of the crystal lattice dominates the parabolic patterns of REE, Y and Sc partition coefficients, consequently, forsterite and aluminium concentrations in olivine are a proxy for D_0^{3+};

5) however, the partitioning of trivalent cations requires maintenance of local charge-balance in olivine crystal structure by formation of magnesium vacancies;
6) AFC modeling conducted with partitioning data from this study indicates that, during magma-carbonate interaction, the melt entrapped in olivine from cumulates becomes enriched in REE, whereas the abundant crystallization of clinopyroxene in endoskarn environments lowers dramatically this enrichment effect.

Acknowledgments

This study benefited of the valuable comments and suggestions by Y. Liang and P. Sossi as reviewers. Their efforts were greatly appreciated, together with the meritorious editorial work of A. Kerr as Editor in-chief of this journal. We are also grateful to Marcel Guillong for his support with laser ablation analyses. Special thanks go to C. Sun and Y. Liang for the kind help provided by sharing the calibration dataset of their Al-in-olivine model for the REE partitioning between olivine and melt.

References

Allen, R.L., Lundström, I., Ripa, M., Simeonov, A., Christofferson, H., (1996), Facies analysis of a 1.9 Ga, continental margin, back-arc felsic caldera province with diverse Zn-Pb-Ag-(Cu-Au) sulphide and Fe oxide deposits, Bergslagen region, Sweden. Econ. Geol., 91, 979-1008

Adams, G.E., Bishop, F.C., 1985. An experimental investigation of thermodynamic mixing properties and unit-cell parameters of forsterite-monticellite solid solution. Am. Mineral. 70, 714-722

Beattie, P., 1993. Olivine-melt and orthopyroxene-melt equilibria. Contrib. Mineral. Petrol. 115, 103-111

Beattie, P., 1994. Systematics and energetics of trace-element partitioning between olivine and silicate melts: Implications for the nature of mineral / melt partitioning. Chem. Geol. 117, 57-71

Bédard, J.H., 2005. Partitioning coefficients between olivine and silicate melts. Lithos 83, 394-419

Blundy, J., Wood, B., 1994. Prediction of crystal-melt partition coefficients from elastic moduli. Nature 372, 452-454

Blundy, J., Wood, B., 2003a. Mineral-Melt Partitioning of Uranium, Thorium and Their Daughters. In: Bourdon, B., et al., (Eds.), Uranium-Series Geochemistry. Rev. Mineral. Geochem. 52, 59-118.

Blundy, J.D., Wood, B.J., 2003b. Partitioning of trace elements between crystals and melts. Earth Planet. Sci. Lett. 210, 383-397

Bottazzi, P., Tiepolo, M., Vannucci, R., Zanetti, A., Brumm, R.C., Foley, S.F., Oberti, R., 1999. Distinct site preference for heavy and light REE in amphibole and the prediction of $^{Amph/L}D_{REE}$. Contrib. Mineral. Petrol. 137, 36-45

Brice, J.C., 1975. Some thermodynamic aspects of the growth of strained crystals. J. Cryst. Growth 28, 249-253

Colson, R.O., McKay, G.A., Taylor, L.A., 1988. Temperature and composition dependencies of trace element partitioning. Olivine/melt and low-Ca pyroxene/melt. Geochim. Cosmochim. Acta 52, 539-553.

Colson, R.O., McKay, G.A., Taylor, L.A., 1989. Charge balancing of trivalent trace elements in olivine and low-Ca pyroxene: a test using experimental partitioning data. Geochim. Cosmochim. Acta 53, 643-648.

Conte, A.M., Dolfi, D., Gaeta, M., Misiti, V., Mollo, S., Perinelli, C., 2009. Experimental constraints on evolution of leucite–basanite magma at 1 and 10^{-4} GPa: implications for parental compositions of Roman high-potassium magmas. Eur. J. Mineral. 21, 763-782.

Coogan, L.A., Hain, A., Stahl, S., Chakraborty, S., 2005. Experimental determination of the diffusion coefficient for calcium in olivine between 900°C and 1500°C. Geochim. Cosmochim. Acta 69, 3683-3694

Dallai, L., Cioni, R., Boschi, C., D'Oriano, C., 2011. Carbonate-derived CO_2 purging magma at depth: Influence on the eruptive activity of Somma-Vesuvius, Italy. Earth Planet. Sci. Lett. 310, 84-95

De Hoog, J.C.M., Gall, L., Cornell, D.H., 2010. Trace-element geochemistry of mantle olivine and application to mantle petrogenesis and geothermobarometry. Chem. Geol. 270, 196-215.

Di Rocco, T., Freda, C., Gaeta, M., Mollo, S., Dallai, L., 2012. Magma chambers emplaced in carbonate substrate: Petrogenesis of skarn and cumulate rocks and implications for CO_2 degassing in volcanic areas. J. Petrol. 53, 2307-2332

Di Stefano, F., Mollo, S., Scarlato, P., Nazzari, M., Bachmann, O., Caruso, M., 2018. Olivine compositional changes in primitive skarn environments: A reassessment of divalent cation partitioning models to quantify the effect of carbonate assimilation. Lithos 316-317, 104-121

Dunworth, E.A., Wilson, M., 1998. Olivine melilitites of the SW German Tertiary volcanic province: Mineralogy and petrogenesis. J. Petrol. 39, 1805-1836

Einaudi, M.T., Meinert, L.D., Newberry, R.J., 1981. Skarn deposits. Econ. Geol., 75th Anniversary Volume, 317-391

Evans, T.M., O'Neill, C., St, H., Tuff, J., 2008. The influence of melt composition on the partitioning of REEs, Y, Sc, Zr and Al between forsterite and melt in the system CMAS. Geochim. Cosmochim. Acta 72, 5708-5721

Ferguson, A.K., 1978. Ca-enrichment in olivines from volcanic rocks. Lithos 11, 189-194

Fulignati, P., Marianelli, P., Santacroce, R., Sbrana, A., 2004. Probing the Vesuvius magma chamber-host rock interface through xenoliths. Geol. Mag. 141, 417-428

Gaeta, M., Di Rocco, T., Freda, C., 2009. Carbonate assimilation in open magmatic systems: The role of melt-bearing skarns and cumulate-forming processes. J. Petrol. 50, 361-385

Gaetani, G.A., 2004. The influence of melt structure on trace element partitioning near the peridotite solidus. Contrib. to Mineral. Petrol. 147, 511-527

Gozzi, F., Gaeta, M., Freda, C., Mollo, S., Di Rocco, T., Marra, F., Dallai, L., Pack, A., 2014. Primary magmatic calcite reveals origin from crustal carbonate. Lithos 190-191, 191-203

Grant, K.J., Wood, B.J., 2010. Experimental study of the incorporation of Li, Sc, Al and other trace elements into olivine. Geochim. Cosmochim. Acta 74, 2412-2428

Hazen, R.M., 1976. Effects of temperature and pressure on the crystal structure of forsterite. Am. Mineral. 61, 1280-1293.

Heinemann, R., Staack, V., Fischer, A., Kroll, H., Vad, T., Kirfel, A., 1999. Temperature dependence of Fe, Mg partitioning in Acapulco olivine. Am. Mineral. 84, 1400-1405.

Huang, F., Lundstrom, C.C., McDonough, W.F., 2006. Effect of melt structure on trace-element partitioning between clinopyroxene and silicic, alkaline, aluminous melts. Am. Mineral. 91, 1385-1400

Imai, T., Takahashi, E., Suzuki, T., Hirata, T., 2012. Element partitioning between olivine and melt up to 10 GPa: Implications for the effect of pressure. Phys. Earth Planet. Inter. 212-213, 64-75

Jurewicz, A.J.G., Watson, E.B., 1988. Cations in olivine, Part 2: Diffusion in olivine xenocrysts, with applications to petrology and mineral physics. Contrib. to Mineral. Petrol. 99, 186-201

Kerrick D.M., Darken, L.S., 1975. Statistical thermodynamic models for ideal oxide and silicate solid solutions, with application to plagioclase. Geochim. Cosmochim. Acta 39, I1443-I1442

Kohn, S.C., Schofield, P.F., 1994. The importance of melt composition in controlling trace-element behaviour: an experimental study of Mn and Zn partitioning between forsterite and silicate melts. Chem. Geol. 117, 73-87

Le Bas, M., Maitre, R.L., Streckeisen, A., Zanettin, B., 1986. A chemical classification of volcanic rocks based on the total alkali silica diagram. J. Petrol. 27, 745-750.

Lee, S.K., Stebbins, J.F., 2003. The distribution of sodium ions in aluminosilicate glasses: a high field Na-23 MAS and 3Q MAS NMR study. Geochim. Cosmochim. Acta 67, 1699-1709.

Leeman, W.P., 1978. Distribution of Mg2+ between olivine and silicate melt, and its implications regarding melt structure. Geochim. Cosmochim. Acta 42, 789-800.

Libourel, G., 1999. Systematics of calcium partitioning between olivine and silicate melt: Implications for melt structure and calcium content of magmatic olivines. Contrib. to Mineral. Petrol. 136, 63-80

Libourel, G., Boivin, P., Biggar, G.M., 1989. The univariant curve liquid = forsterite + anorthite + diopside in the system CMAS at 1 bar: solid solutions and melt structure. Contrib. to Mineral. Petrol. 102, 406-421

Longhi, J., Walker, D., Hays, J.F., 1978. The distribution of Fe and Mg between olivine and lunar basaltic liquids. Geochim. Cosmochim. Acta 42, 1545-1558

Maekawa, H., Maekawa, T., Kawamura, K., Yokokawa, T., 1991. The structural groups of alkali silicate glasses determined from 29Si MAS-NMR. J. Non-Cryst. Solids 127, 53-64

Mallmann, G., O'Neill, H.ST.C., 2009. The Crystal / Melt Partitioning of V during Mantle Melting as a Function of Oxygen Fugacity Compared with some other Elements (Al, P, Ca, Sc, Ti, Cr, Fe, Ga, Y, Zr and Nb). J. Petrol. 50, 1765-1794

Mallmann, G., O'Neill, H.ST.C, 2013. Calibration of an Empirical Thermometer and Oxybarometer based on the Partitioning of Sc, Y and V between olivine and silicate melt J. Petrol. 0, 1-17

Matsui, Y., Onuma, N., Nagasawa, H., Higuchi, H., Banno, S., 1977. Crystal structure control in trace element partition between crystal and magma. Bull. Soc. Fr. Minéral. Cristallogr. 100, 317-324

Mibe, K., Orihashi, Y., Nakai, S., Fuji, T., 2006. Element partitioning between transition-zone minerals and ultramafic melt under hydrous conditions. Geophys. Res. Lett. 33, 1-6

Mollo, S., Vona, A., 2014. Lithos The geochemical evolution of clinopyroxene in the Roman Province: A window on decarbonation from wall-rocks to magma. Lithos 192-195, 1-7

Mollo, S., Del, P., Ventura, G., Iezzi, G., Scarlato, P., 2010. Lithos Dependence of clinopyroxene composition on cooling rate in basaltic magmas: Implications for thermobarometry. Lithos 118, 302-312

Mollo, S., Heap, M.J., Dingwell, D.B., Hess, K.U., Iezzi, G., Masotta, M., Scarlato, P., Vinciguerra, S., 2013a. Decarbonation and thermal microcracking under magmatic *P-T-*f_{CO2} conditions: the role of skarn substrata in promoting volcanic instability, Geophys. J. Intern. 195, 369-380

Mollo, S., Blundy, J.D., Scarlato, P., Iezzi, G., Langone, A., 2013b. The partitioning of trace elements between clinopyroxene and trachybasaltic melt during rapid cooling and crystal growth, Contrib. to Mineral. Petrol. 166, 1633-1654

Mollo, S., Forni F., Bachmann, O., Blundy, J.D., De Astis, G., Scarlato, P., 2016. Trace element partitioning between clinopyroxene and trachy-phonolitic melts: A case study from the Campanian ignimbrite (Campi Flegrei, Italy), Lithos 252-253, 160-172

Mollo, S., Blundy, J.D., Giacomoni, P.P., Nazzari, M., Scarlato, P., Coltorti, M., Langone, A., Andronico, D., 2017. Clinopyroxene-melt element partitioning during interaction between trachybasaltic magma and siliceous crust: clues from quartzite enclaves at Mt. Etna volcano. Lithos 284-285, 447-461

Mysen, B.O., 2004. Element partitioning between minerals and melt, melt composition, and melt structure. Chem. Geol. 213, 1-16

Mysen, B.O., Virgo, D., 1980. Trace element partitioning and melt structure: An experimental study at 1 atm pressure. Geochim. Cosmochim. Acta 44, 1917-1930

Mysen, B.O., Virgo, D., Seifert, F.A., 1982. The structure of silicate melts: implications for chemical and physical properties of natural magma. Rev. Geophys. 20, 353-383

Mysen, B.O., Carmichael, I.S.E., Virgo, D., 1985. A comparison of iron redox ratios in silicate glasses determined by wet-chemical and 57 Fe Mössbauer resonant absorption methods. Contrib. to Mineral. Petrol. 90, 101-106

Nagasawa, H., 1966. Trace element partition coefficients in ionic crystals. Science 152, 767-769

Nielsen, R.L., Drake, M.J., 1979. Pyroxene -melt equilibria. Geochim. Cosmochim. Acta 43, 1259-1272

Nielsen, R.L., Dungan, M.A., 1983. Low pressure mineral-melt equilibria in natural anhydrous mafic systems. Contrib. to Mineral. Petrol. 84, 310-326

Nielsen, R.L., Gallahan, W.E., Newberger, F., 1992. Experimentally determined mineral-melt partition coefficients for Sc, Y and REE for olivine, orthopyroxene, pigeonite, magnetite and ilmenite. Contrib. to Mineral. Petrol. 110, 488-499

O'Neill H.ST.C., Eggins S.M., 2002. The effect of melt composition on trace element partitioning: an experimental investigation of the activity coefficients of FeO, NiO, CoO, MoO_2 and MoO_3 in silicate melts. Chem. Geol. 186, 151-181

Onuma, N., Higuchi, H., Wakita, H., Nagasawa, H., 1968. Trace element partitioning between two pyroxenes and the host lava. Earth Planet. Sci. Lett. 5, 47-51

Papike, J.J., Karner, J.M., Shearer, C.K., 2005. Comparative planetary mineralogy: Valence state partitioning of Cr, Fe, Ti, and V among crystallographic sites in olivine, pyroxene, and spinel from planetary basalts. Am. Mineral. 90, 277-290

Press, W.H., Teukolsky, S.A., Vetterling, W.T., Flannery, B.P., 1992. Numerical recipes in C, 2nd edn. Cambridge University Press, London

Pu, X., Lange, R.A., Moore, G., 2017. A comparison of olivine-melt thermometers based on D_{Mg} and D_{Ni}: The effects of melt composition, temperature, and pressure with applications to MORBs and hydrous arc basalts. Am. Mineral. 102, 750-765

Purton, J.A., Allan, N.L., Blundy, J.D., 1997. Calculated solution energies of heterovalent cations in forsterite and diopside: Implications for trace element partitioning. Geochim. Cosmochim. Acta 61, 3927-3936

Putirka, K.D., 2016. Rates and styles of planetary cooling on Earth, Moon, Mars, and Vesta, using new models for oxygen fugacity, ferric-ferrous ratios, olivine-liquid Fe-Mg exchange, and mantle potential temperature. Am. Mineral. 101, 819-840

Putirka, K.D., Perfit, M., Ryerson, F.J., Jackson, M.G., 2007. Ambient and excess mantle temperatures, olivine thermometry, and active vs. passive upwelling. Chem. Geol. 241, 177-206

Qian, Q., Hermann, J., Wang, Y., Guo, J., Liu, F., Wang, L., 2015. Variations of clinopyroxene/melt element partitioning during assimilation of olivine/peridotite by low-Mg diorite magma. Chem. Geol. 419, 36-54

Redi, D., Cannatelli, C., Esposito, R., Lima, A., Petrosino, P., De Vivo, B., 2017. Somma-Vesuvius' activity: a mineral chemistry database. Mineral. Petrol. 111, 43-67

Roeder, P.L., Emslie, R.F., 1970. Olivine-Liquid Equilibrium. Contrib. to Mineral. Petrol. 29, 275-289.

Ryerson, F.J., Hess, P.C., 1978. Implications of liquid-liquid distribution coefficients to mineral-liquid partitioning. Geochim. Cosmochim. Acta 42, 921-932

Shannon, R.D., 1976. Revised effective ionic radii in oxides and fluorides. Acta Cryst. A32, 751-757

Shi, P., 1993. Low pressure phase relationships in the system Na_2O-CaO-FeO-MgO-Al_2O_3-SiO_2 at 1100 °C, with implications for the differentiation of basaltic magmas. J. Petrol. 34, 743-762

Shi, P., Libourel, G., 1991. The effects of FeO on the system CMAS at low pressure and implications for basalt crystallization processes. Contrib. to Mineral. Petrol. 108, 129-145

Snyder, D.A., Carmichael, I.S.E., 1992. Olivine-liquid equilibria and the chemical activities of FeO, NiO, Fe_2O_3, and MgO in natural basic melts. Geochim. Cosmochim. Acta 56, 303-318

Sun, C., Liang, Y., 2013. The importance of crystal chemistry on REE partitioning between mantle minerals (garnet, clinopyroxene, orthopyroxene, and olivine) and basaltic melts. Chem. Geol. 358, 23-36

Sun, C., Liang, Y., 2014. An assessment of subsolidus re-equilibration on REE distribution among mantle minerals olivine, orthopyroxene, clinopyroxene, and garnet in peridotites. Chem. Geol. 372, 80-91

Suzuki, T., Akaogi, M., 1995. Element Partitioning between Olivine and Silicate Melt under High Pressure. Phys. Chem. Miner. 22, 411-418

Taura, H., Yurimoto, H., Kurita, K., Sueno, S., 1998. Pressure dependence on partition coefficients for trace elements between olivine and coexisting melts. Phys. Chem. Miner. 25, 469-484

Tiepolo, M., Vannucci, R., Zanetti, A., Brumm, R., Foley, S.F., Bottazzi, P., Oberti, R., 1998. Fine-scale structural control of REE site-preference: the case of amphibole. Mineral Mag. 62A, 1517-1518.

Toplis, M.J., 2005. The thermodynamics of iron and magnesium partitioning between olivine and liquid: Criteria for assessing and predicting equilibrium in natural and experimental systems. Contrib. to Mineral. Petrol. 149, 22-39

Toplis, M.J., Carroll, M.R., 1995. An experimental study of the influence of oxygen fugacity on Fe-Ti oxide stability, phase relations, and mineral-melt equilibria in ferro-basaltic systems. J. Petrol. 36, 1137-1170

Van Westrenen, W., Allan, N.L., Blundy, J.D., Purton, J.A., Wood, B.J., 2000. Atomistic simulation of trace element incorporation into garnets-comparison with experimental garnet-melt partitioning data. Geochim. Cosmochim. Acta 64, 1629-1639

Wan, Z., Coogan, L.A., Canil, D., 2008. Experimental calibration of aluminum partitioning between olivine and spinel as a geothermometer. Am. Mineral. 93, 1142-1147

Wang, Z., Gaetani, G.A., 2008. Partitioning of Ni between olivine and siliceous eclogite partial melt: Experimental constraints on the mantle source of Hawaiian basalts. Contrib. to Mineral. Petrol. 156, 661-678

Warner, R.D., Luth, W.C., 1973. Data for the Join Monticellite ($CaMgSiO_4$) - Forsterite (Mg_2SiO_4): Experimental Results and Numerical Analysis. Am. Mineral. 58, 998-1008

Watson, E.B., 1976. Two-liquid partition coefficients: experimental data and geochemical implications. Contrib. to Mineral. Petrol. 56, 119-134

Watson, E.B., 1977. Partitioning of manganese between forsterite and silicate liquid. Geochim. Cosmochim. Acta 41, 1363-1374

Watson, E.B., 1979. Calcium content of forsterite coexisting with silicate liquid in the system Na_2O-CaO-MgO-$A1_2O_3$-SiO_2. Am. Mineral. 64, 824-829

Wenzel, T., Baumgartner, L.P., Brügmann, G.E., Konnikov, E.G., Kislov, E. V., Orsoev, D.A., 2001. Contamination of mafic magma by partial melting of dolomitic xenoliths. Terra Nov. 13, 197-202

Wenzel, T., Baumgartner, L.P., Konnikov, E.G., Bru, G.E., Kislov, E. V, 2002. Partial Melting and Assimilation of Dolomitic Xenoliths by Mafic Magma: the Ioko-Dovyren Intrusion (North Baikal Region, Russia). J. Petrol. 43, 2049-2074

Wood, B.J., Blundy, J.D., 1997. A predictive model for rare earth element partitioning between clinopyroxene and anhydrous silicate melt. Contrib. to Mineral. Petrol. 129, 166-181

Wood, B.J., Blundy, J.D., 2003a. Trace element partitioning under crustal and uppermost mantle conditions: the influences of ionic radius, cation charge, pressure and temperature. In: Carlson, R.W. (Ed.), The mantle and core. Treatise on Geochemistry 2. Elsevier, Amsterdam, pp. 395-424

Zanetti, A., Tiepolo, M., Oberti, R., Vannucci, R., 2004. Trace-element partitioning in olivine: modelling of a complete data set from a synthetic hydrous basanite melt. Lithos 75, 39-54

Figure captions

Fig. 1. Onuma diagram (Onuma et al., 1968) where $\ln D_{R3+}$ is plotted versus the ionic radius of REE, Y and Sc assumed in six-fold coordination (data from Shannon, 1976). Trivalent cations are grouped according to ionic charge and arranged from largest to smallest ionic radii (i.e., from 0.745 to 1.032 Å moving from Sc to La).

Fig. 2. Variations of D_{Sc} and D_{Nd} as a function of T, ^{melt}Mg# and $CaCO_3$. D_{Sc} and D_{Nd} are selected as representative of trivalent cations with small and large ionic radii, respectively

Fig. 3. The optimum cation radius, r_0 (a), and the apparent Young modulus, E (b), of REE, Y and Sc are plotted versus Mg, Fe, and Ca cations in olivine. Through the multiple regression analysis and the standardized regression coefficient, the statistical influence of Mg, Fe and Ca (as independent variables) on the values of r_0 and E (as dependent variables) has been also determined and showed in figure.

Fig. 4. Relationship between the strain-free partition coefficient, D_0^{3+}, and $1/T$, ${}^{melt}MgO$, ${}^{melt}X_{SiO2}$, ${}^{melt}X_{Al2O3}$, ${}^{melt}X_{CaO}$ and NBO/T (i.e., the number of NBO per tetrahedrally coordinated cations T).

Fig. 5. Values of D_0^{3+} predicted by the Al-in-olivine model of Sun and Liang (2013) are plotted versus those measured from our decarbonation experiments (a). The 1:2 and 2:1 dotted lines constrain the calibration error of the model. D_0^{3+} is negatively correlated with Fo (b) and positively correlated with Al (c) in olivine. The grey circles represent the calibration data of the model of Sun and Liang (2013), by selecting only olivine and melt compositions similar to those obtained in this study.

Fig. 6. Comparison between ${}^{ol}Al^{0.5}$ and melt $X_{Al}/(X_{Si}^{0.25})$ assumed as proxies for the activities of $AlO_{1.5}$ and SiO_2 in the melt (a). This plot comes from the stoichiometric substitution reaction proposed by Evans el al. (2008): ${}^{melt}(AlO_{1.5}) + {}^{ol}(0.25Mg_2SiO_4) = {}^{ol}(0.5MgAl_2O_4) + {}^{melt}(0.25SiO_2)$. $\ln D_{Sc}$ vs. ${}^{melt}[1/(Sc)^{0.33}]$ plot in which data from Grant and Wood (2010) are compared with those from this study (b). By solving the vacancy reaction $(3^{M}Mg) \leftrightarrow (2^{M}R^{3+}, {}^{M}V)$, Grant and Wood (2010) found that D_{Sc} scales with ${}^{melt}[1/(Sc)^{0.33}]$ expressed in ppm, for a paired substitution of Sc and a vacancy for Mg in octahedral sites.

Fig. 7. ${}^{melt}a_{Sc}$ is plotted versus ${}^{ol}a_{Mg4/5Sc4/5V2/5SiO4}$, ${}^{ol}a_{Mg1/2ScV1/2SiO4}$, ${}^{ol}a_{MgSc2/3V1/2SiO4}$, and ${}^{ol}a_{MgScAlO4}$, as representative of different incorporation mechanisms of Sc in olivine crystallographic site. See the text for further details.

Fig. 8. Histogram diagram showing the influence that substitution mechanisms involving ${}^{ol}a_{Mg4/5Sc4/5V2/5SiO4}$, ${}^{ol}a_{Mg1/2ScV1/2SiO4}$, ${}^{ol}a_{MgSc2/3V1/2SiO4}$, and ${}^{ol}a_{MgScAlO4}$ exercise on the incorporation of REE, Y and Sc in olivine crystallographic site. See the text for further details.

Fig. 9. AFC modeling of melt inclusion compositions in olivine phenocrysts from cumulates and endoskarns belonging to the Colli Albani Volcanic District (CAVD) in central Italy (Di Rocco et al., 2012; Gaeta et al., 2009). The AFC1 trajectory for cumulates indicates a maximum amount of olivine fractionation of ~15%. The AFC2 trajectory for endoskarns accounts for olivine and clinopyroxene fractionation in 76:24 relative proportions and a total solid amount of ~13%.

Figures

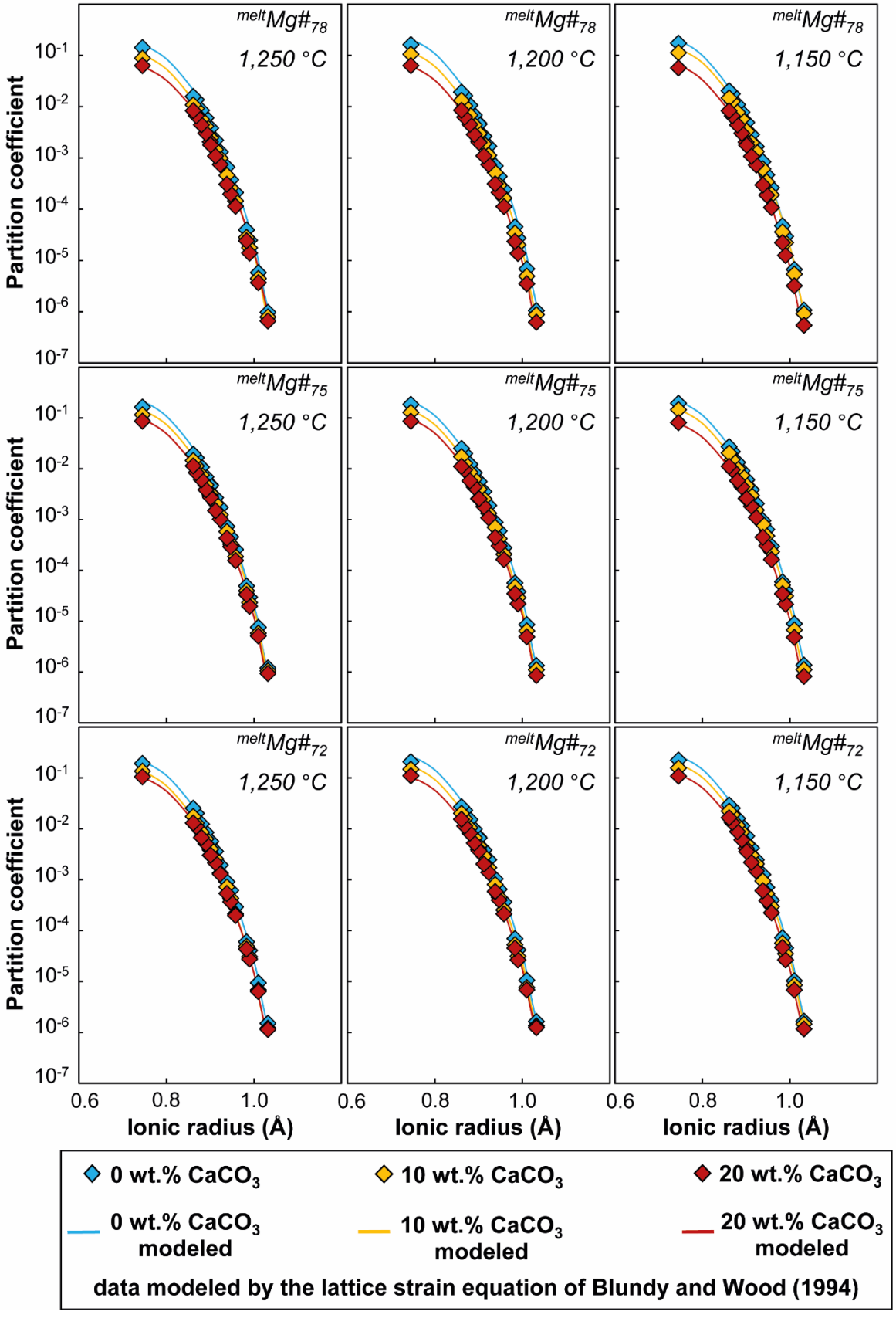

Figure 1

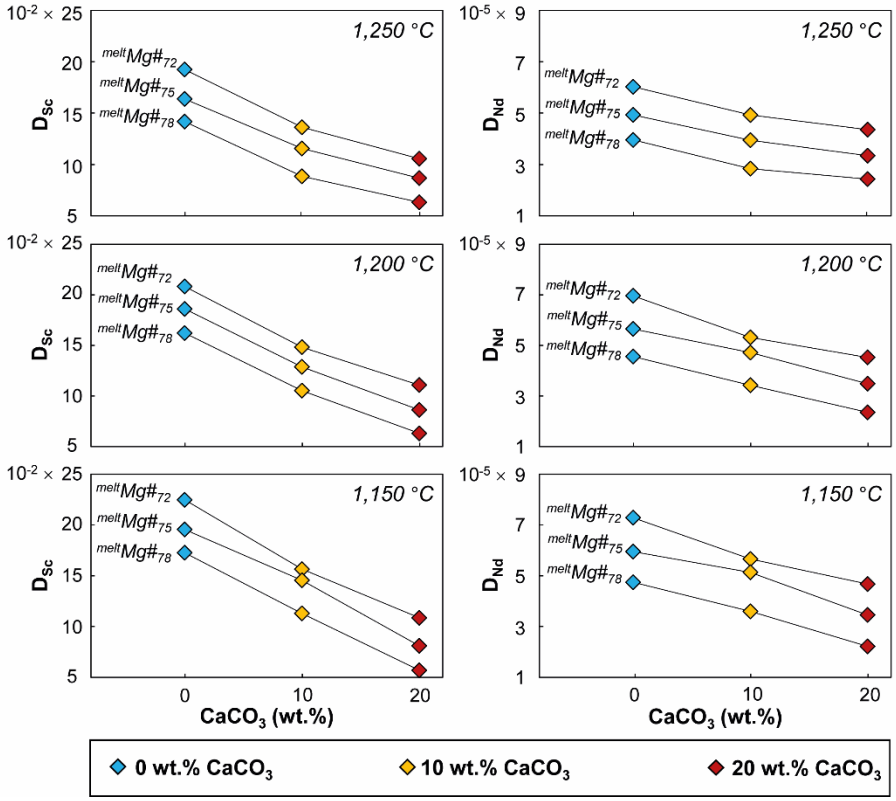

Figure 2

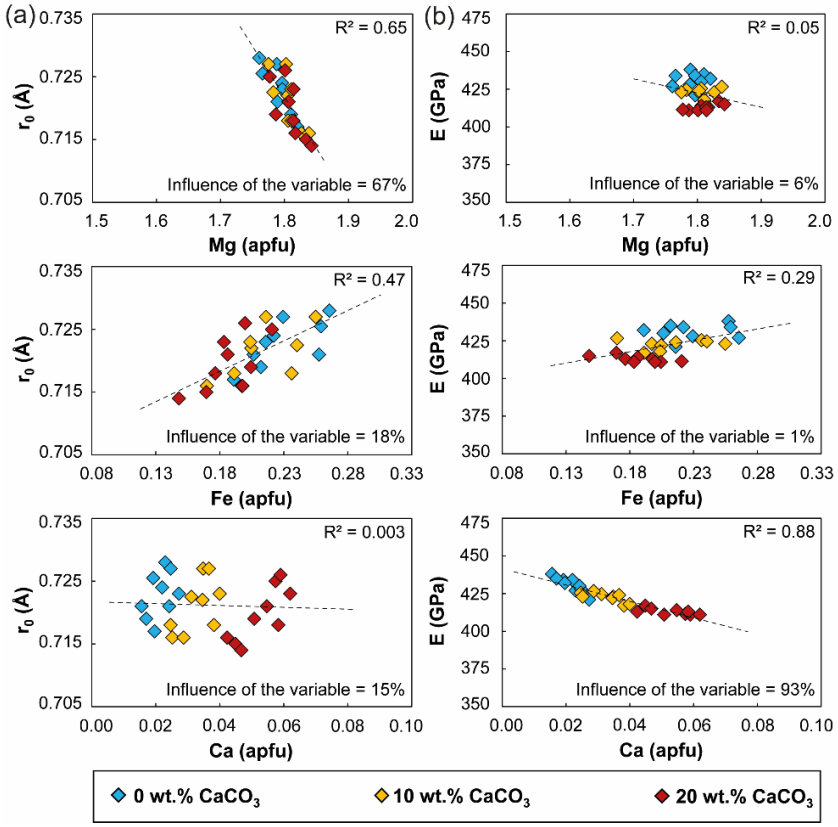

Figure 3

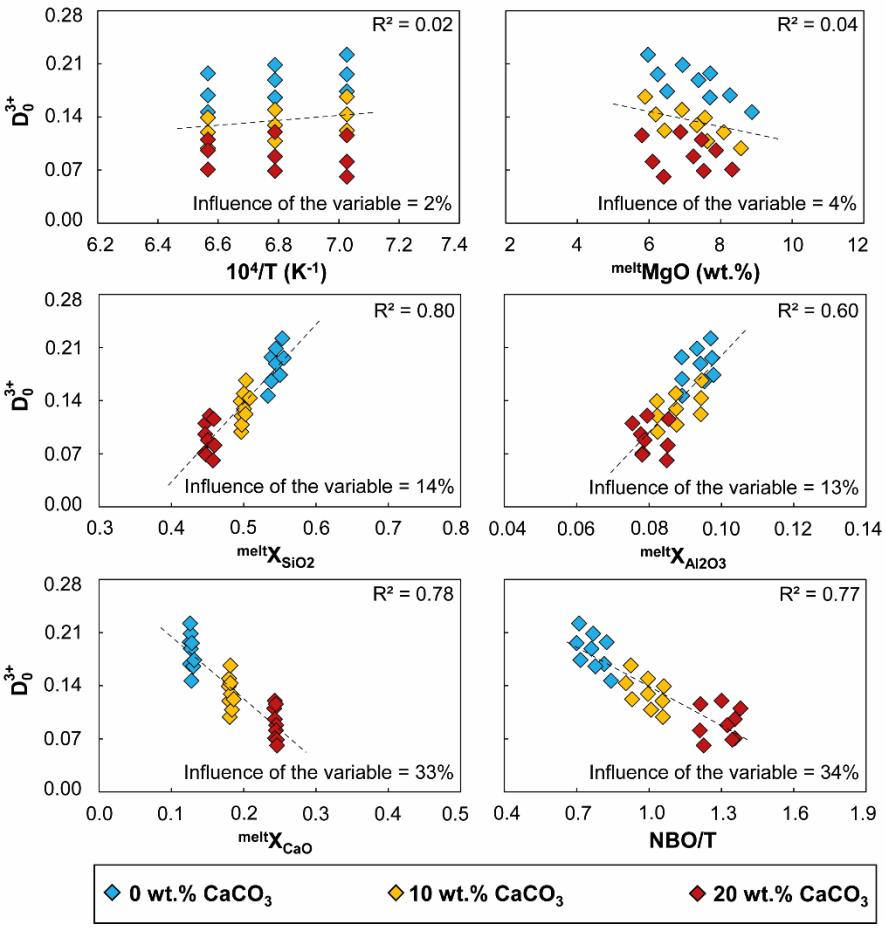

Figure 4

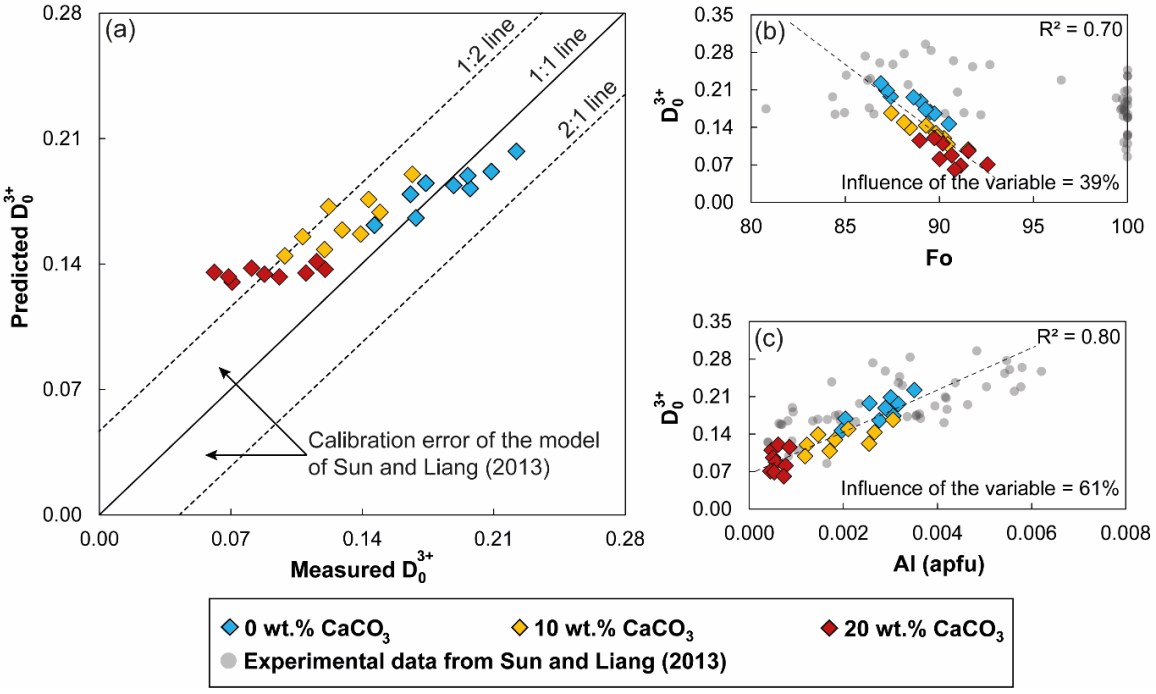

Figure 5

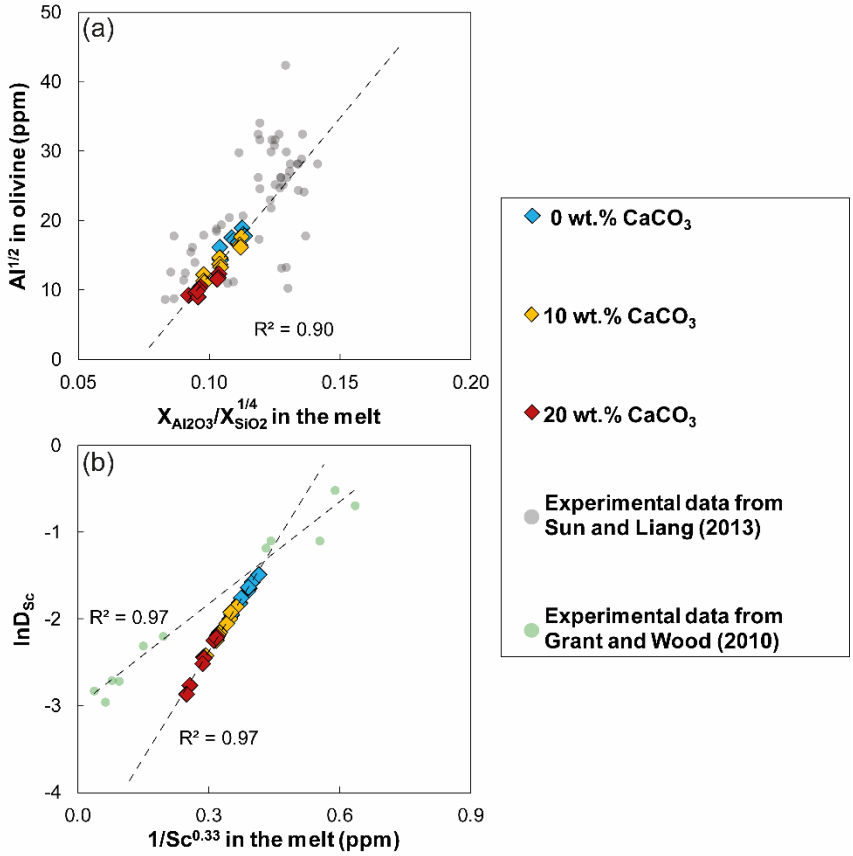

Figure 6

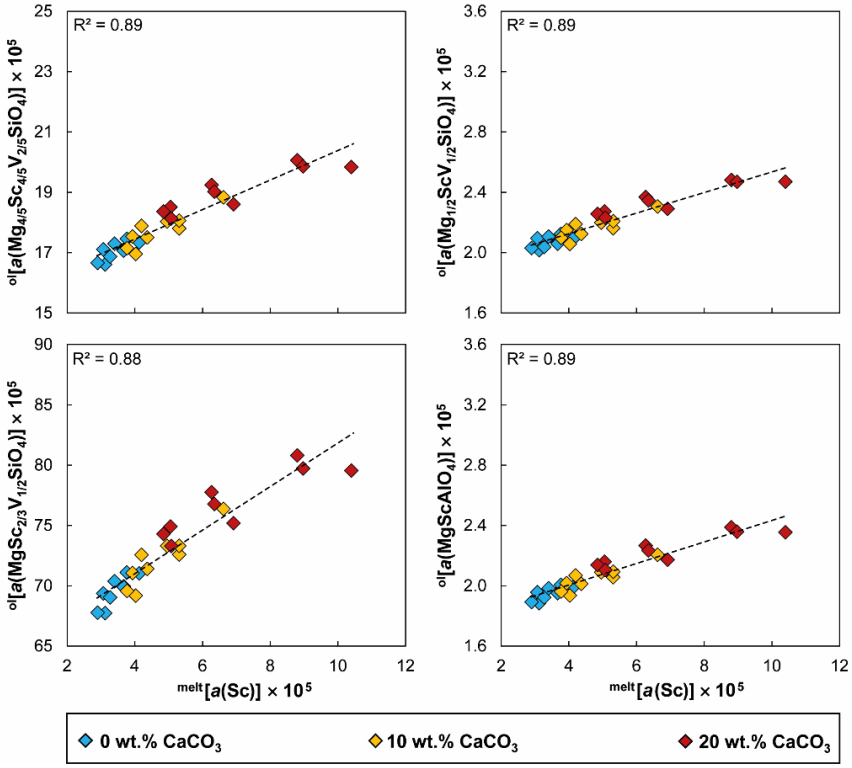

Figure 7

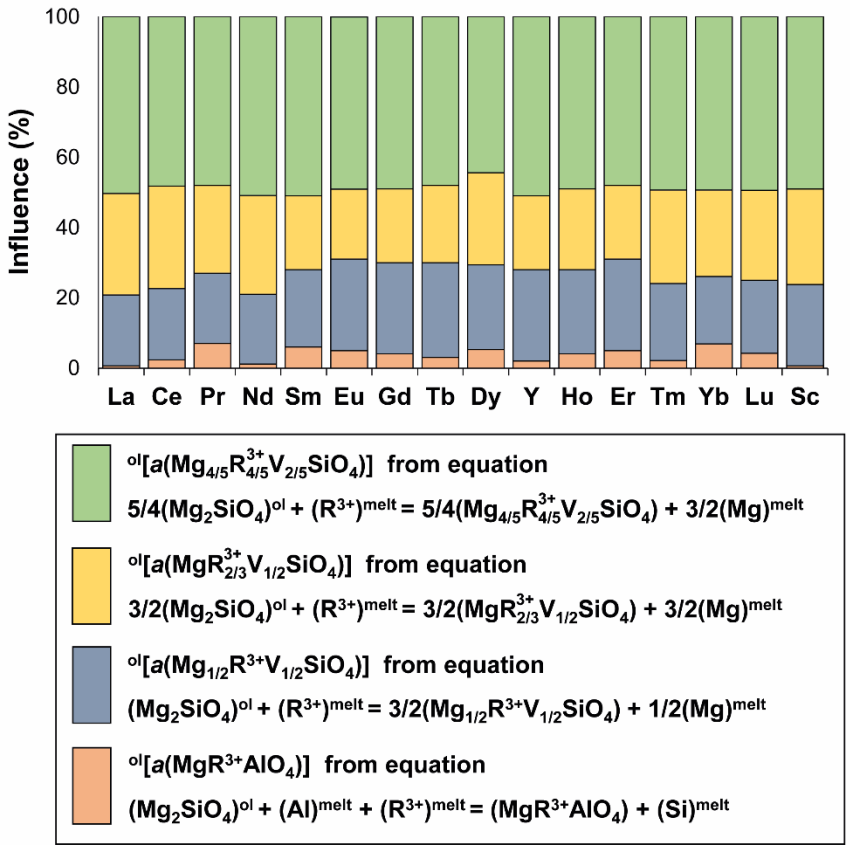

Figure 8

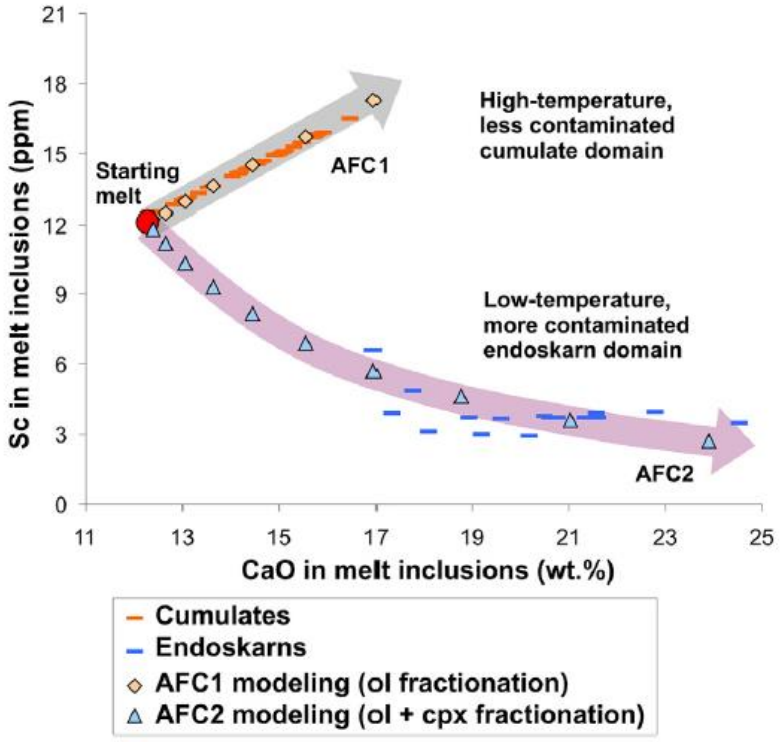

Figure 9

Tables

Table 1. Experimental conditions and phase relations

Run (#)	Mg# melt	$CaCO_3$ (wt.%)	*t* (h)	T (°C)	P (MPa)	log(fO_2)	Gl (wt.%)	Ol (wt.%)	Cpx (wt.%)	Ti-Mt (wt.%)
MM1-A	72	0	72	1250	0.1	-7.7	96.5	3.5	-	-
MM1-C	72	10	72	1250	0.1	-7.7	97.8	2.2	-	-
MM1-D	72	20	72	1250	0.1	-7.7	99.1	0.9	-	-
MM2-A	72	0	72	1200	0.1	-8.2	93.7	6.3	-	-
MM2-C	72	10	72	1200	0.1	-8.2	86.9	4.8	8.3	-
MM2-D	72	20	72	1200	0.1	-8.2	84.2	1.5	14.3	-
MM3-A	72	0	72	1150	0.1	-8.85	79.1	8.0	11.6	1.2
MM3-C	72	10	72	1150	0.1	-8.85	76.7	6.4	15.7	1.2
MM3-D	72	20	72	1150	0.1	-8.85	74.7	4.1	20.2	1.0
MM4-A	75	0	72	1250	0.1	-7.7	95.7	4.3	-	-
MM4-C	75	10	72	1250	0.1	-7.7	96.7	3.3	-	-
MM4-D	75	20	72	1250	0.1	-7.7	98.1	1.9	-	-
MM5-A	75	0	72	1200	0.1	-8.2	92.8	7.2	-	-
MM5-C	75	10	72	1200	0.1	-8.2	94.7	5.3	-	-
MM5-D	75	20	72	1200	0.1	-8.2	95.2	4.8	-	-
MM6-A	75	0	72	1150	0.1	-8.85	90.7	9.3	-	-
MM6-C	75	10	72	1150	0.1	-8.85	87.3	7.7	5.0	-
MM6-D	75	20	72	1150	0.1	-8.85	79.0	6.7	14.3	-
MM7-A	78	0	72	1250	0.1	-7.7	93.3	6.7	-	-
MM7-C	78	10	72	1250	0.1	-7.7	95.0	5.0	-	-
MM7-D	78	20	72	1250	0.1	-7.7	97.2	2.8	-	-
MM8-A	78	0	72	1200	0.1	-8.2	90.1	9.9	-	-
MM8-C	78	10	72	1200	0.1	-8.2	91.7	8.3	-	-
MM8-D	78	20	72	1200	0.1	-8.2	92.2	7.8	-	-
MM9-A	78	0	72	1150	0.1	-8.85	88.0	12.0	-	-
MM9-C	78	10	72	1150	0.1	-8.85	89.5	10.5	-	-
MM9-D	78	20	72	1150	0.1	-8.85	81.4	9.1	9.5	-

Table 2. Lattice strain parameters

	D_0	σ(10)	r_0 (Å)	σ(10)	E (GPa)	σ(10)
MM1-A	0.197	0.018	0.721	0.005	438	26
MM1-C	0.139	0.018	0.718	0.004	425	26
MM1-D	0.110	0.016	0.716	0.003	413	21
MM2-A	0.209	0.019	0.726	0.005	434	26
MM2-C	0.149	0.016	0.723	0.005	425	25
MM2-D	0.120	0.016	0.719	0.003	411	29
MM3-A	0.222	0.023	0.728	0.006	427	26
MM3-C	0.167	0.019	0.727	0.005	423	34
MM3-D	0.116	0.014	0.725	0.004	411	25
MM4-A	0.169	0.016	0.719	0.005	435	30
MM4-C	0.120	0.017	0.716	0.002	423	25
MM4-D	0.096	0.015	0.715	0.003	417	29
MM5-A	0.189	0.018	0.724	0.003	434	26
MM5-C	0.129	0.015	0.722	0.005	422	25
MM5-D	0.088	0.015	0.721	0.005	414	33
MM6-A	0.196	0.021	0.727	0.006	428	26
MM6-C	0.143	0.018	0.727	0.005	424	25
MM6-D	0.081	0.014	0.726	0.004	411	29
MM7-A	0.146	0.016	0.717	0.004	432	26
MM7-C	0.099	0.016	0.716	0.005	427	26
MM7-D	0.071	0.015	0.714	0.005	415	33
MM8-A	0.166	0.017	0.721	0.006	430	26
MM8-C	0.108	0.015	0.718	0.002	417	25
MM8-D	0.069	0.015	0.718	0.005	413	29
MM9-A	0.174	0.021	0.723	0.006	421	25
MM9-C	0.122	0.017	0.723	0.005	418	33
MM9-D	0.061	0.013	0.723	0.005	411	25

Supplementary data to this article can be found online at https://doi.org/10.1016/j.lithos.2018.12.019.

Mush cannibalism and disruption recorded by clinopyroxene phenocrysts at Stromboli volcano: new insights from recent 2003-2017 activity

Flavio Di Stefano[1,*]

[1]Dipartimento di Scienze della Terra, Sapienza-Università di Roma, P.le Aldo Moro 5, 00185 Roma, Italy

Abstract

The Present-day (<1.2 kyr) activity of Stromboli (Aeolian Islands, Southern Italy) is fed by a vertically-extended mush column with an open-conduit configuration. The eruptive products are the result of periodic supply of mafic magma (low porphyritic or *lp*-magma) from depth into a homogeneous shallow reservoir (highly porphyritic or *hp*-magma). Clinopyroxene phenocrysts from the 2003-2017 activity exhibit marked diopside-augite heterogeneities caused by continuous *lp*-*hp* magma mixing and antecryst recycling. Diopsidic bands record *lp*-recharges injected into the shallow *hp*-reservoir, whereas resorbed diopsidic cores testify to the continuous disruption and cannibalism of relic antecrysts from the mush. The transition between diopside (~1,175 °C) and augite (~1,130 °C) takes place at comparable *P* (~190 MPa) and H_2O (0.5-2.4 wt.%) conditions. Shorter timescales (~1 year) for diopsidic bands from the 2003 paroxysm document restricted temporal intervals between mafic injection, magma mixing and homogenization in the *hp*-reservoir. Longer timescales (~4-182 years) for diopsidic cores indicate increasingly antecryst remobilization times. By comparing clinopyroxenes from the Present-day and Post-Pizzo eruptions, we argue a distinct phase in the life of Stromboli volcano commenced at least after the 2003 paroxysm. More efficient mechanisms of mush disruption and cannibalism involve diopsidic antecrysts remobilized and transported by *lp*-magmas permeating the mush, in concert with gravitational instability of the solidification front and melt migration within the shallow *hp*-reservoir. Magmatic injections feeding the persistent Present-day activity are more intensively mixed and homogenized prior to eruption, reflecting small recharge volumes and/or a more mafic system in which the mafic inputs are less evident.

1. Introduction

Unravelling the pre-eruptive history of magmas encompasses innumerable ongoing challenges in modern volcanology and petrology. The quantitative assessment of the intensive parameters, rates, and timescales of the processes that modulate the plumbing systems beneath active

volcanoes (e.g., magma storage and ascent, mixing and mingling, fractional crystallization) is today essential to gain insights into the interpretation of monitoring signs (e.g., McNutt, 2005; Petrone et al., 2016; White and McCausland, 2016; Biggs and Pritchard, 2017; Cashman et al., 2017; Putirka, 2017; Ubide and Kamber, 2018).

Steady-state volcanic systems, such as Stromboli (Francalanci et al., 1999; Petrone et al., 2018) and Mt. Etna (Bonaccorso and Calvari, 2013; Mollo et al., 2018; Ubide et al., 2019a) are modulated by a state of equilibrium between the rate of magma recharge and persistent eruptive activity (e.g., O'Hara, 1977; Wadge, 1982), in concert with the compositional homogeneity of erupted magmas (Armienti et al., 2007). It is widely accepted that steady-state conditions reflect the dynamics of an open conduit system undergoing continuous recharge, crystallization and eruption (e.g., Giberti et al., 1992; Sheehan and Barclay, 2016). The Present-day activity of Stromboli volcano (<1.2 kyr; Rosi et al., 2000; Petrone et al., 2018) is fed by a shallow magmatic reservoir continuously refilled with mafic magmas and undergoing mixing and crystallization processes before eruption (e.g., Francalanci et al., 1999, 2004; Landi et al., 2004; Armienti et al., 2007).

Typical 'Strombolian' activity consists of frequent mild explosions (up to 10 per hour; e.g., Ripepe et al., 2002) ejecting shoshonitic black scoriae, lapilli and ash. This activity is periodically interrupted by lava flows and more violent explosions (so-called major explosions and paroxysms) producing small volumes of light pumice (~10% in volume of the erupted magma; Francalanci et al., 2012). According to the early study of Barberi et al. (1993), major explosions and paroxysms were discriminated on the basis of hazard criteria. Major explosions do not affect the settled areas, occurring as single and/or multiple blasts with intervals of few seconds to minutes. Conversely, paroxysms represent a treat for the inhabitants and villages, with higher volumes of erupted juvenile material. Although numerous works have accurately investigated the behavior of the Present-day activity and the physico-chemical conditions of the Stromboli plumbing system (e.g., Giberti et al., 1992; Allard et al., 1994, 2000; Harris and Stevenson, 1997; Francalanci et al., 2004, 2005, 2012; Métrich et al., 2001, 2010; Bertagnini et al., 2003, 2008; Petrone et al., 2018; Scarlato et al., 2019;

Ubide et al., 2019b), some aspects regarding the pre-eruptive magma dynamics remain overlooked. The mechanisms controlling the temporal variations from normal activity to violent explosions are not well defined and quantified. Many studies report very rapid timescales (from hours to a few months) for the last injection of mafic magma prior to eruption from the Post-Pizzo (~1.7-1.5 kyr) to the Present-day eruptive periods, by measuring the compositional changes in olivine (Bertagnini et al., 2003), clinopyroxene (Petrone et al., 2018; Ubide et al., 2019b) and plagioclase (Agostini et al., 2013). Crystal residence time of pre-eruptive magmatic processes, recorded by Fe-Mg elemental diffusion in clinopyroxene, are in the order of 1 to ~50 years (up to ~150 years) during the Post-Pizzo and Early Paroxysm (~0.35 kyr) of the Present-day periods (Petrone et al., 2018). Bulk rocks dated with U-series disequilibria provide residence times of ~5 years (2-10 years) in the shallow reservoir and longer residence times (up to ~55 years) in the deeper reservoir for the products erupted during the Present-day activity (Bragagni et al., 2014). As pointed out by Petrone et al. (2018), despite the good agreement between diffusion-based residence times and those calculated via radiogenic isotopes, a more complex heterogeneity is recorded by phenocrysts. Indeed, minerals record more convoluted magmatic histories in which crystals can be recycled by fresh inputs of magma into shallower reservoirs (e.g., Francalanci et al., 2005, 2012; Métrich et al., 2010; Petrone et al., 2018). Syn-eruptive mixing and mush cannibalism are also indicated by the compositional variations in plagioclase and clinopyroxene cargoes (Landi et al., 2004; Armienti et al., 2007; Petrone et al., 2018; Ubide et al., 2019b), and isotopic disequilibria of plagioclase phenocrysts (Francalanci et al., 2005, 2012).

Clinopyroxene is a common igneous mineral stable over a wide range of depths, from the upper mantle to the upper crust. Its low chemical diffusivity offers the potential to trace 1) the physico-chemical state of the plumbing system under variable *P*-*T*-H_2O conditions (e.g., Putirka et al., 1996, 2003; Putirka, 1999, 2008, 2017; Mollo et al., 2010, 2013, 2018; Armienti et al., 2013; Masotta et al., 2013; Mollo and Masotta, 2014; Perinelli et al., 2016; Neave and Putirka, 2017), 2) the kinetic effects related to magma undercooling and reservoir dynamics (e.g., Scarlato et al., 2019;

Ubide et al., 2019a, 2019b) and 3) the timescales of magmatic processes and eruption triggers (e.g., Petrone et al., 2016, 2018; Ubide and Kamber, 2018). On this basis, we have investigated the normal, major and paroxysmal activity during the period 2003-2017, starting with the largest paroxysm of the last 50 years. Detailed textural analysis of clinopyroxene phenocrysts, major and trace element data and elemental mapping, combined with results from thermobarometry, diffusion chronometry, geochemical and numerical modeling, provide novel quantitative constrains on the architecture of the plumbing system and the temporal evolution of magmas prior to eruption. The close interplay between magma reservoirs, mush and inputs of fresh magmas typical of the highly dynamic regime at Stromboli, is dominated by extensive mush cannibalization through a vertically-extended mush column.

2. Petrological and volcanological background

Stromboli Island is the northernmost stratovolcano of the Aeolian volcanic arc, in the southern Tyrrhenian Sea (Fig. 1a). It rises from a depth of ~2,000 m below sea level to an elevation of 924 m above sea level (Morelli et al., 1975) with a total volume of ~300 km^3. Its persistent activity started ~1.2 kyr ago (Rosi et al., 2013) and consists of periodic mild explosions (i.e., normal Strombolian activity) alternating with episodic lava effusion and violent explosions (i.e., paroxysms; Barberi et al., 1993). The oldest subaerial rocks (204 ± 25 kyr) form the Strombolicchio neck, located 1.7 km NE of Stromboli Island as part of the same submarine edifice (Gillot and Keller, 1993). The subaerial portion of Stromboli is the result of six subsequent epochs marked by distinctive magma compositions (Francalanci et al., 2013 and references therein): Paleostromboli I (~85 kyr), Paleostromboli II (~60 kyr), Paleostromboli III (~35 kyr), Vancori (~26 kyr), Neostromboli (~13 kyr) and Recent (~2.4 kyr). These periods were characterized by eight edifice collapses (Francalanci et al., 1993; Hornig-Kjarsgaard et al., 1993). The youngest collapse sequence generated the Sciara del Fuoco scar on the NW flank of the volcano (Fig.1a) and hosts a significant volume of recent material (Rosi, 1980; Pasquarè et al., 1993; Kokelaar and Romagnoli, 1995; Tibaldi, 2001; Tibaldi et al., 2003; Francalanci

et al., 2005, 2013; Lucchi et al., 2013). The Strombolicchio neck and Paleostromboli II are represented by calc-alkaline lava flows, whereas Paleostromboli I and III activities are characterized by high-K calc-alkaline pyroclastic deposits and lavas. Subsequently, shoshonitic and K-alkaline lavas were erupted from central and eccentric vents during Vancori and Neostromboli periods, respectively. The Recent epoch 6 is divided into three shorter periods (Francalanci et al., 2013; Lucchi et al., 2013): epoch 6a (2.4-1.2 kyr; Francalanci et al., 2013) started with shoshonitic ('Pizzo Sopra la Fossa' formation) and high-K calc-alkaline ('San Bartolo' formation) basalts (Francalanci et al., 2014) and continued with shoshonitic pyroclastic deposits (Post-Pizzo formation; Petrone et al., 2006, Chiappe Lisce formation; Francalanci et al., 2013; Lucchi et al., 2013) and lavas (Bastimento formation); epoch 6b (< 1.2 kyr; Rosi et al., 2013) was characterized by a strong SE-dipping lateral collapse and pyroclastic cones related to a more persistent activity; and epoch 6c (< 0.35 kyr; Arrighi et al., 2004; Speranza et al., 2008) marked by the last relevant lateral collapse and the onset of the typical Present-day activity.

The Present-day activity is focused within four vents inside the Sciara del Fuoco depression and topographically beneath the Pizzo Sopra la Fossa peak (Fig. 1a). In this region, the explosive activity occurs from multiple vents that are focused within three main regions named SW, NE and Central area, respectively. During 'normal' Strombolian activity, shoshonitic black scoria bombs, lapilli and ash are ejected with an interval of about five to ten events per hour and generally accumulate around the craters at the base of the Sciara del Fuoco scar. This activity is also accompanied by continuous emissions of H_2O, CO_2 and SO_2 (Allard et al., 1994, 2000). The normal mild activity is sometimes interrupted by voluminous shoshonitic lavas flowing within the Sciara del Fuoco scar (every 4 years, on average; Barberi et al., 1993; Aiuppa et al., 2010). Approximatively two times per year (Barberi et al., 1993; Rosi et al., 2013), more violent 'major explosions' eject meter-sized scoriaceous bombs and blocks over the Pizzo Sopra la Fossa peak and lapilli and ash reach coastal zones (e.g., Barberi et al., 1993). Rare and more violent events significantly interrupt the normal activity, erupting lavas and small volumes of shoshonitic light pumices (~10% in volume)

mingled with black scoriae (~90% in volume) (Francalanci et al., 2005). During these 'paroxysms', meter-size blocks and bombs reach the coast around the island. Sometimes, these violent explosions accompany a general instability phase of the volcano during which lava flows and landslides along the Sciara del Fuoco scar can be generated, sometimes leading to the occurrence of and tsunamis (Bonaccorso et al., 2003). The black scoriae and lavas represent degassed, highly porphyritic (*hp*) magma with highly radiogenic Sr, whereas light pumices are ejected only during paroxysm and represent a more mafic, less Sr-radiogenic, volatile-rich and low porphyritic (*lp*) magma (Francalanci et al., 1999, 2004). The *lp*-magma is a mantle-derived basalt stored in a deep ponding zone (≥ 240 MPa; Métrich et al., 2005). This mafic magma persistently feeds the plumbing system and interacts with the crystal mush before mixing and homogenization with the shallow *hp*-magma (~3 km depth; Francalanci et al., 1999; Bragagni et al., 2014). Minerals in scoriae and lavas are characterized by strong chemical, isotopic and textural heterogeneities, testifying to repeated *lp*-injections into the shallow *hp*-system. During normal and major activities, the mixing process consists of low volumes of mafic *lp*-magmas (undegassed and poorly crystallized) arriving into the *hp*-reservoir (Francalanci et al., 2012). In contrast, light pumices (*lp*-magmas) are erupted only during the more energetic major explosions and paroxysms, during which rapid mafic injections erupt without complete homogenization within the shallow *hp*-reservoir (Bertagnini et al., 1999; Andronico and Pistolesi, 2010; Francalanci et al., 2013).

2.1. Eruption chronology

In the present work, we have analyzed and investigated a suite of light pumice (*lp*-magma) and black scoria (*hp*-magma) samples which represent the different eruptive styles typical of the Present-day activity from 2003 to 2017. The samples span normal (24/05/2013 and 15/12/2017), major (08/11/2009, 24/11/2009, 23/10/2017, 01/11/2017 and 01/12/2017) and paroxysm (05/04/2003 and 15/03/2007) events (Fig. 1b-c).

The 5 April 2003 paroxysm was one of the most powerful of the last 50 years. Following a prolonged period of activity that started on 28 December 2002 with an abrupt interruption of the normal mild activity at the summit craters and the consequent emission of lavas flowing along the Sciara del Fuoco scar, the violent paroxysm of 5 April 2003 caused the fallout of bombs, lithic blocks and ash over the upper part of the edifice. A fallout deposit of light pumice along the southern flanks of the cone was followed by the ejection of ballistics on Ginostra village and the emplacement of thick pyroclastic flow deposits in the uppermost part of the Sciara del Fuoco scar (Rosi et al., 2006; Francalanci et al., 2008; Pistolesi et al., 2008; Harris et al., 2008). From 20 June 2003 (Calvari et al., 2005), the explosive activity in the crater terrace resumed in concert with the quasi-instantaneous rise of magma in the central conduit and the increment of the normal Strombolian activity in all craters (Puglisi et al., 2005; Ripepe et al., 2005; Landi et al., 2006, 2008). The outpouring of lava flows ended on 22 July, with a total 2002-2003 volume of 1.3×10^7 m^3 of lava and an average effusion rate of ~0.7 m^3/s (Marsella et al. 2008).

On 27 February 2007, the NE external flank of the NE-crater was affected by an eruptive fissure with three intense lava emissions flowing on the Sciara del Fuoco scar (Barberi et al., 2009; Landi et al., 2009). In the following days, Strombolian explosions ceased and the -crater terrace retreated to the SE after episodic gravitational failures (Calvari et al. 2010; Andronico et al., 2013). On 15 March 2007, a paroxysmal explosion from the NE crater ejected ballistic blocks towards Stromboli village producing an eruptive plume which deposited ash, lapilli and bombs in the SW sector. The total volume of emitted lavas was similar to that erupted during the 2002-2003 paroxysm (~10^7 m^3), but the effusion rate of the 2007 paroxysm was one order of magnitude greater (Landi et al., 2009).

On the 8th and 24th November 2009, two energetic major events ejected large volumes of juvenile products (Andronico and Pistolesi, 2010). The 8th November event was preceded by mild explosions at the central sector with discontinuous fountaining, strong spattering and lavas flowing within the crater. The tephra related to the eruption column covered an area of ~10,000 m^2. On 24th

November, two main explosions produced a more energetic plume associated with tephra that covered an area of ~15,000 m^2.

After November 2009, several episodes of spattering, lava fountains and lava flows occurred within the crater terrace and along the Sciara del Fuoco scar. The last sequence of this activity started in December 2012 and ended in May 2013 with the normal event of 24th May 2013 which was also associated with very small lava flows supplied for a few hours or days.

During the period from October to December 2017, activity strongly increased in the central and southern sectors leading to major explosions on 23rd October, 1st November, and 1st December. Voluminous spatter deposited along the Sciara del Fuoco scar and on the Pizzo area, as well as high ash columns, were dispersed on the southern side of the island. On the morning of 15th December, the northern crater was affected by spattering activity and lava flows which poured downward the Sciara del Fuoco scar, afterward the activity started to go back to 'normal' explosive levels.

3. Analytical methods

Bulk rock analyses for major and trace elements were conducted at Actlabs (Activation Laboratories Ltd.). Results are reported in the Supplementary material (Table 1S), together with certified analyses of international reference materials used as quality control. Major elements were analyzed by lithium metaborate/tetraborate fusion - ICP-OES (inductively coupled plasma optical emission spectrometry). Sample washing was performed to remove any organic, loosely adhered, and cementing material. Washing included soaking in a mixture of HCl and H_2O_2 as well as cleaning in acetone using an ultrasonic bath. The analyses were performed in a batch system. Each batch contained a method reagent blank and certified reference materials. Samples were mixed with a flux of lithium metaborate and lithium tetraborate and fused in an induction furnace. The molten material was immediately poured into a solution of 5% nitric acid containing an internal standard, and mixed continuously until completely dissolved (about 30 min). The samples were run on a Thermo Jarrell-Ash ENVIRO II ICP. Calibration was performed using 7 prepared USGS and CANMET certified

reference materials. FeO was determined through titration, using a cold acid digestion of ammonium metavanadate, and hydrofluoric acid in an open system. Ferrous ammonium sulphate was added after digestion and potassium dichromate was the titrating agent. This cold digestion dissolved silicates and some sulphides. Trace elements were measured by lithium metaborate/tetraborate fusion - ICP-MS (inductively coupled plasma mass spectrometry). Fused samples were diluted and analyzed using a Perkin Elmer Sciex ELAN 6,000, 6,100 or 9,000 instrument. Three blanks and five controls (three before sample group and two after) were analyzed with each group of samples. All reaction steps are quantitative.

Clinopyroxene major element compositions were determined by electron probe microanalysis (EMP) at the HP-HT Laboratory of Experimental Volcanology and Geophysics of the Istituto Nazionale di Geofisica e Vulcanologia (INGV) in Rome (Italy), using a JEOL JXA-8200 instrument equipped with five wavelength dispersive spectrometers. Analyses were performed on carbon-coated thin sections under high vacuum conditions using an accelerating voltage of 15 kV and an electron beam current of 7.5 nA, with a beam diameter of 2.5 µm. Elemental counting times were 10 s on the peak and 5 s on each of two background positions, except for chromium, which was measured for 20 s on the peak and 10 s on each background position. Corrections for inter-elemental effects were made using a ZAF (Z: atomic number; A: absorption; F: fluorescence) procedure. Calibration used a range of standards from Micro-Analysis Consultants (MAC; http://www.macstandards.co.uk): albite (Si-PET, Al-TAP, Na-TAP), forsterite (Mg-TAP), augite (Fe-LIF), apatite (Ca-PET), orthoclase (K-PET), rutile (Ti-PET), rhodonite (Mn-LIF) and JEOL Cr metal (Cr-PET). Spot analyses defined transects across the crystals with constant spot separation, typically of 5 µm. Results were screened based on stoichiometry and analytical totals, and the final dataset comprises 4,351 analyses (Table 2S). Smithsonian augite (Jarosewich et al., 1980) and MAC augite were used as quality monitor standards and for the calculation of accuracy and precision. Accuracy was better than 1-5% for the more abundant elements and better than 5-10% for elements with abundances below 1 wt.%. Precision was typically better than 1-5% for all analyzed elements. For mapping, we used 1.5-3.0 µm

pixel size and 50-60 ms dwell time per pixel, measuring up to 5 elements per analysis (one per diffracting crystal). Mapped areas varied in size from 1,536×1,536 µm to 3072×2560 µm, with total experiment times of 15-18 h.

Clinopyroxene trace element compositions and zoning were investigated using laser ablation inductively coupled plasma mass spectrometry (LA-ICP-MS) mapping (Table 3S), following the rastering technique described in Ubide et al. (2015). Experiments were carried out at The University of Queensland Centre for Geoanalytical Mass Spectrometry, Radiogenic Isotope Facility (UQ RIF-lab). We used an ASI RESOlution 193 µm excimer UV ArF laser ablation system with a dual-volume Laurin Technic ablation cell and GeoStar Norris software, coupled with a Thermo iCap RQ quadruple mass spectrometer operated by the Qtegra software (see Ubide et al., 2019a for further details on analytical set up and procedures). Ablation was performed in ultrapure He to which Ar make-up gas with a trace amount of N_2 was added for efficient transport and to aid ionization. Two experiments were run per crystal with identical laser parameters and different analyte menus to obtain maps for a large number of trace elements without compromising spatial resolution (see Ubide et al., 2015, 2019a). The instruments were tuned with scans on NIST612 glass reference material. Elemental maps were built with Iolite (Paton et al., 2011) v2.5 in quantitative mode, using NIST610 glass reference material as the calibration standard and calcium concentrations previously obtained by electron microprobe (21.1 ± 0.5 wt.% CaO; n = 4,351) as internal standard. Accuracy and precision were monitored using BHVO-2G, BCR-2G and BIR-1G glass reference materials as secondary standards (http://georem.mpch-mainz.gwdg.de/). Precision was better than 5% and accuracy was better than 5-15%. Limits of detection (Longerich et al., 1996) were typically at the sub-ppm level for most analyzed elements and below 5 ppm for Al and Cr.

4. Results

4.1. Textural features and geochemistry of erupted magmas

Black scoriae show highly porphyritic seriate textures (~45-60 vol.% of pheno- and micro-phenocrysts) with a microcrystalline groundmass and low vesicularity (~10-20 vol.%; Fig. 2a-c) with no difference between products erupted during normal, major and paroxysmal activities. In contrast, light pumices exhibit weakly porphyritic seriate textures (<10 vol.% of phenocrysts, typically ~5 vol.%) with a glassy groundmass and high vesicularity (~30-40 vol.%; Fig. 2d). The paragenesis is identical in all samples and consists of olivine (≤ 5 vol.%) and clinopyroxene (~10-15 vol.%) phenocrysts (up to ~10 mm in sizes), associated with plagioclase (~20-30 vol.%) micro-phenocrysts and microlite-bearing glassy groundmass (Fig. 2).

According to the TAS diagram (Total Alkali vs. Silica; Le Bas et al., 1986; Fig. 1b), the samples are classified as basalts, with a restricted compositional range (SiO_2 = 49.82-51.33 wt.%; Table 1S). Normal activity products (24 May 2013 and 15 December 2017) are very close to the basalt-trachybasalt boundary (Fig. 1b). On the K_2O vs. SiO_2 diagram (Peccerillo and Taylor, 1976; Fig. 1b), sample compositions are intermediate between high-K and shoshonitic basalts, as typically observed for the Active Craters activity (cf. Scarlato et al., 2019; Fig. 1b). The chondrite-normalized pattern of REE (Rare Earth Elements) (Fig. 2S) is typical of arc-type settings (Peccerillo et al., 2013), showing preferential enrichments LREE (Light Rare Earth Elements) relative to HREE (Heavy Rare Earth Elements) with a mild negative Eu anomaly (Eu/Eu* = 0.28-0.32). Variations in major and trace elements through 2003-2017 eruptive events (Fig. 1c) define cyclic paths with a gradual decrease of Mg# [molar Mg/(Mg + Fe) where Fe is total iron], Al_2O_3/CaO and Cr and increase of Ce, Zr and Sr that follow two peaks that correspond to the paroxysm of 2003 and the major event of November 2017. The light pumice erupted in 2003 shows the highest values of $Mg\#_{58}$, Al_2O_3/CaO = 0.75 and Cr = 60 ppm. It is also worth stressing that the paroxysm of 2003 records a wide compositional gap between light pumice and black scoria, which shows values of $Mg\#_{54}$, Al_2O_3/CaO = 0.63 and Cr = 40 ppm. This gap decreases in the subsequent paroxysm of March 2007 in terms of both major and trace elements, with the exception of Cr that remains constant in both pumices and scoriae (Fig. 1c). The studied eruptive activity points towards minima of $Mg\#_{49}$ and Cr = 30 ppm for

the major eruption of October 2017 (Fig. 1c). Immediately after the end of October 2017, more mafic products (i.e., $Mg\#_{56}$, Cr = 50 ppm, Zr = 125 ppm and Sr = 649 ppm) are evident. However, in only 1.5 months, the composition of magma rapidly evolved until the eruption of 15th December 2017 (i.e., $Mg\#_{50}$, Cr = 40 ppm, Zr = 149 ppm, Sr = 765 ppm).

4.2. Textural and compositional features of clinopyroxene phenocrysts

Clinopyroxene phenocrysts are euhedral with complex zoning patterns (Figs. 3 and 1S). According to Morimoto (1988), diopsidic ($Mg\#_{93-88}$) resorbed cores (i.e., antecrysts; Francalanci et al., 2012) and bands are overgrown by augitic ($Mg\#_{79-74}$) mantles and rims (Figs. 3 and 1S), in which sector and oscillatory zoning typically develop. As a general rule, the antecrysts and diopsidic bands are compositionally distinct from mantles and rims in terms of diopside (Di) and hedenbergite (Hd) components (Fig. 4), whereas only minor variations are observable for jadeite (Jd) and the sum of Tschermak components (ΣTs = CaTs + CaFeTs + CaTiTs). No marked differences are evident between the major element contents of prism (i.e., {1 0 0}, {1 1 0}, {0 1 0}) and hourglass (i.e., {-1 1 1}) sectors in mantles and rims (Fig 4). The concentration of incompatible trace elements (i.e., REE, Zr, Yb) and Sc increases in mantle and rim portions with respect to antecryst cores and diopsidic bands (Fig. 5). However, the latter display higher Cr contents, reaching maximum values of ~2,200 and ~11,000 ppm (in the diopsidic cores and bands, respectively; Fig. 5). Compared to major elements, the concentrations of trace elements vary significantly as a function of crystallographic direction, with slightly higher levels in prism relative to hourglass sectors.

On the basis of textural and chemical features, two main groups of clinopyroxene can be recognized (Fig. 3): Group A consists of diopsidic antecrysts with augitic overgrowths, whereas Group B refers to phenocrysts in which diopsidic cores are always absent. These two groups can be further divided into sub-groups depending on the presence (Sub-group A1 or B1) or absence (Sub-group A2 or B2) of diopsidic bands (Fig. 3), following the classification scheme proposed by Petrone et al. (2018) for the Post-Pizzo eruptions and the Early Paroxysms of the Present-day activity at

Stromboli. However, we emphasize that the estimated occurrence (volume fraction) of each single sub-group is remarkably different for the recent 2003-2017 period. Sub-groups A1 and B1 are the least common in all samples (~4 vol.% and ~3 vol.%, respectively) and usually have only one single well-defined diopsidic band, forming a sharp boundary within the crystal mantle. In contrast, for the Post-Pizzo activity and Early Paroxysms of the Present-day activity, Petrone et al. (2018) document that the most abundant clinopyroxenes contain both single and multiple bands, either within the mantle or at the rim. Clinopyroxenes with mafic rims are absent in the 2003-2017 period, in marked contrast with Post-Pizzo phenocrysts (cf. Petrone et al., 2018). The Sub-group A2 refers to diopsidic cores with sharp and discontinuous boundaries and is more common (~29 vol.%) than Sub-groups A1 and B1. Finally, Sub-group B2 is recognized as the most abundant in all samples (~64 vol.%), with clinopyroxene phenocrysts characterized by more homogeneous augitic compositions, despite the presence of both sector and oscillatory zoning.

5. Discussion

5.1. *P*-*T*-H_2O crystallization conditions

Clinopyroxene is commonly used as a *P*-*T*-H_2O-sensitive phase to estimate the crystallization conditions of magmas on account of its enlarged saturation surface and low intra-crystal cation diffusivity (Putirka et al., 1996, 2003; Putirka, 1999, 2008; Nimis and Taylor, 2000; France et al., 2010; Mollo et al., 2010, 2013, 2018; Armienti et al., 2013; Masotta et al., 2013; Mollo and Masotta, 2014; Perinelli et al., 2016; Neave and Putirka, 2017). Sector zoning in clinopyroxene phenocrysts may also represent a valuable indicator for the effect of undercooling during magma chamber processes and eruptive dynamics (Ubide et al., 2019a, 2019b). In order to minimize the error associated with estimates of clinopyroxene-based thermometers, barometers and hygrometers, we tested for equilibrium between diopsidic/augitic crystal portions and bulk rock/matrix glass. The bulk composition of the light pumice erupted during the paroxysm of 05/04/2003 ($Mg\#_{58}$) is in equilibrium with diopsidic antecrysts and bands because of its mafic characteristics, whilst the averaged matrix

glass composition ($Mg\#_{40}$) is matched with mantles and rims as the most evolved domains. Under such circumstances, the Fe-Mg exchange between clinopyroxene and melt yields values of 0.20-0.27 by modulating the Fe^{2+}/Fe^{3+} ratio in the melt (Kress and Carmichael, 1991) as a function of the buffering conditions ($-1.66 \leq \Delta NNO \leq 1.27$) estimated for shoshonite magmas at Stromboli (Scarlato et al., 2019 and references therein). Generally, the accepted equilibrium range of $K_D(Fe\text{-}Mg)^{cpx\text{-}melt} = 0.28 \pm 0.08$ (Putirka, 2008) is the weighted arithmetic mean of a much broader equilibrium range (0.04-0.68) obtained by linear regression analysis of experimental clinopyroxene-melt compositions (Putirka, 2008). According to Putirka (1999) and Mollo et al. (2013), this oversimplified approach does not account for kinetic effects related to variable crystal growth conditions caused by magma undercooling (Mollo et al., 2013; Mollo and Hammer, 2017). Hence, we applied more robust equilibrium tests relying on 1) the difference between measured vs. predicted diopside + hedenbergite components (ΔDiHd from Putirka et al., 1996 and Mollo et al., 2013) and 2) the modeling of clinopyroxene-melt partition coefficients (ΔD_{Na} and ΔD_{Ti}) by the lattice strain equation (Blundy et al., 1995; Hill et al., 2011; Mollo et al., 2018) (see also Ubide et al., 2019a, 2019b). Within the calibration uncertainty of each model, we found close agreement between measured and predicted values (Fig. 6), demonstrating the attainment of near-equilibrium crystallization between clinopyroxene and feeding melt.

By integrating barometry (Putirka et al., 1996; error of ± 136 MPa), thermometry (Scarlato et al., 2019; error of ± 6 °C) and hygrometry (Perinelli et al., 2016; error of ± 0.5 wt.%), we have calculated the probability density function for each magmatic variable. Gaussian distribution plots (Fig. 7a) show that the augitic mantles and rims peak at relatively low-*T* (~1,130 °C), whereas diopsidic cores and bands equilibrate at comparable high-*T* (~1,175 and ~1,165 °C, respectively). H_2O estimates (0.5-2.4 wt.%; Figs. 7a and 3S) always overlap within the hygrometer uncertainty of ± 0.5 wt.%. When pairing the more evolved compositions of the matrix glass with clinopyroxene mantles/rims, the estimated H_2O contents peak at a slightly higher value (~1.5 wt.%), possibly due to the increased amount of solid fraction at the late stage of the phenocryst growth, before magma

degassing and micro-phenocryst/microlite crystallization. Similarly, pressure does not change significantly (160-190 MPa) among the different crystal portions (Figs. 7a and 3S), in agreement with the lack of substantial changes for the *P*-sensitive jadeite component in clinopyroxene (e.g., Blundy et al., 1995; Fig. 4). The comparison between *P*-*T*-H_2O estimates and eruption dates (Fig. 7b) highlights an almost stable crystallization path over the fourteen years of investigated volcanic activity. The physico-chemical conditions of the system remain constant and the variance of our pressure estimates encompasses the two main reservoirs recognized at Stromboli (e.g., Bertagnini et al., 2003; Landi et al., 2004; Aiuppa et al., 2010; Métrich et al., 2010). According to P_{CO2} and P_{H2O} measurements based on basaltic melt inclusions in olivine (Métrich et al., 2010), the *lp*-magma is stored at 190-260 MPa (~7-10 km depth for an average crustal density of 2,700 kg/m^3; Fig. 7a; Allard, 2010) where the original concentration of H_2O dissolved in the primitive, undegassed magma may be up to 3.5 wt.%. Conversely, extensive H_2O degassing takes place at 50-100 MPa (~2-4 km depth) by increasing the liquidus temperature of the melt (Métrich et al., 2001, 2010), promoting further crystallization of clinopyroxene and plagioclase micro-phenocrysts/microlites within the *hp*-reservoir (Fig. 7a). Deflation measurements conducted in 2007 and the source inferred from the inversion of the GPS and tilt data suggest the presence of an elongated shallow-intermediate plumbing system positioned in between the *lp*- and *hp*-storage (Bonaccorso et al., 2008). Seismic signals also point to very shallow crustal processes (< 1 km; Chouet et al., 2003; Bonaccorso et al., 2008) where gas slugs rising from a maximum depth of 3 km expand in the final part of the open conduit (Burton et al., 2007; Bonaccorso et al., 2008).

5.2. Reconstruction of magma dynamics by clinopyroxene zoning

The Present-day activity at the summit craters of Stromboli is persistently fed by a vertically-extended mush column, encompassing both the shallow and deeper reservoirs (e.g., Métrich et al., 2010; Aiuppa et al., 2010) or extending through the shallow one toward the deeper one (e.g., Francalanci et al., 2011; Bragagni et al., 2014), with an open-conduit configuration. The periodic

supply of fresh magma in the uppermost section of the plumbing system, in combination with efficient mixing and crystallization, ensures bulk compositional uniformity (i.e., shoshonitic basalt; Fig. 1b) of erupted products through time. On the other hand, clinopyroxene and plagioclase phenocrysts exhibit marked chemical heterogeneities and complex textures caused by continuous *lp-hp* magma mixing, together with antecryst recycling from different mush portions (Francalanci et al., 2005, 2012, 2014; Bragagni et al., 2014; Petrone et al., 2018). The growth of plagioclase is mostly driven by magma degassing and cooling in the shallow part of the mush column (from ~130 MPa to eruption) by long-standing replenishments within the *hp*-magma reservoir (Francalanci et al., 2013). In contrast, the crystallization of clinopyroxene starts at ~400 MPa (Figs. 7 and 3S) recording, via diopsidic-augitic transition (Fig. 4), the entire differentiation path of mantle-derived basalts rising through the mush column (e.g., Métrich et al., 2010). Due to successive influxes of primitive melts, the magmatic composition becomes progressively more mafic from the Pizzo activity (2.4-1.8 ka) to Post-Pizzo (~1.7-1.5 kyr) and Early Paroxysms (~0.35 kyr) of the Present-day activity (Francalanci et al., 2005, 2012; Petrone et al., 2018; Ubide et al., 2019b). This compositional trend is also confirmed by the increased Mg# of both augitic ($Mg\#_{70-80}$) and diopsidic ($Mg\#_{81-93}$) clinopyroxene portions from Post-Pizzo to Early Paroxysms (Petrone et al., 2018) and 2003-2017 eruptions. Textural characteristics and compositional zoning in clinopyroxene phenocrysts indicate multi-stage crystallization across the *lp-hp*-reservoirs, where diopsidic antecrysts and bands are markers of more primitive, high-*T* magmas injecting into the shallow, low-*T* domains (Figs. 7 and 3S). *Lp*-pumices are erupted only during the more energetic major and paroxysm explosions, but normal and mild major events still carry diopsidic antecrysts from the pre-existing crystal mush which is periodically disrupted by the ascent of *lp*-magmas (Francalanci et al., 2005, 2012). Such cannibalism is consistent with highly dynamic regimes within the magmatic mush column of mafic alkaline systems (e.g., Albarède et al., 1997; Armienti et al., 2007) and is very common for extremely active volcanoes like Stromboli (Francalanci et al., 2005, 2012; Petrone et al., 2018; Ubide et al., 2019b) and Mt. Etna (e.g., Armienti et al., 2013; Mollo et al., 2015; Ubide and Kamber, 2018). It has also been documented that

resorbed cores of plagioclase and clinopyroxene (0.70630-0.70635 $^{87}Sr/^{86}Sr$) from the Present-day activity are in isotopic disequilibrium with both *lp* (0.706097-0.706113 $^{87}Sr/^{86}Sr$) and *hp* (0.706157-0.706248 $^{87}Sr/^{86}Sr$) compositions erupted from 1900 CE to 2007 (Sr isotope data from Francalanci et al., 2005, 2012). This observation indicates that clinopyroxene antecrysts belong to a pre-1900 CE crystal mush that may have developed during a period of reduced magma recharge and increased crystal fractionation (Francalanci et al., 2005). On the basis of these observations, Francalanci et al. (2005) suggest that the old crystal mush zone may represent the feeding reservoir of the San Bartolo products (~2.4 kyr; Francalanci et al., 1988, 1989; Ubide et al., 2019b). In agreement with this theory, Landi et al. (2006) and Francalanci et al. (2012) report a systematic decrease in Sr-isotope ratio of bulk rock and groundmass samples from the beginning of the 2002-2003 eruptive crisis. The authors link the isotope variations to magma mixing (20% *lp* + 80% *hp*) via injections of fresh, volatile-rich *lp*-magma into the volatile-poor *hp*-reservoir feeding lava flows associated with paroxysm activity. From the 5th April 2003 eruption, the difference between groundmass and bulk rock Sr-isotope ratios increases, accounting for the increased number of radiogenic Sr antecrysts estimated at a modal content of ~8 vol.%. After the violent paroxysm, these antecrysts are transported into the shallow system by the arrival of recurrent *lp*-magmas passing through the crystal mush zone (Francalanci et al. 2005, 2012). The frequency of ~ 33% of Group A clinopyroxenes (Fig. 3) in the 2003-2017 products testify the importance of mush remobilization and cannibalization processes during the 14 years of activity subsequent to the 2003 paroxysm.

To better understand the geochemical changes characterizing the 2003-2017 Present-day activity, we quantify the evolutionary path of trace element systematics in the plumbing system via the Rayleigh fractional crystallization (*FC*) equation:

$$C_l = C_0 \times F^{(D-1)} \quad (1)$$

where C_l is the trace element concentration in the residual melt, C_0 is the concentration in the starting composition, F is the fraction of the melt remaining in the system, and D is the clinopyroxene-melt partition coefficient. The compatible and mildly incompatible behavior of Cr and Zr cations, respectively (e.g., D'Orazio et al., 1998), were examined for the diopsidic antecrysts and recharge bands in relation to the augitic overgrowths. These elements have been showed to be robust recorders of magmatic histories in clinopyroxene (Ubide and Kamber, 2018). In order to effectively address the bulk composition of the system (i.e., the overall crystal and melt chemistry), D_{Cr} (80) and D_{Zr} (0.12) were estimated as the ratio between the averaged core-to-rim concentration of clinopyroxenes and the averaged bulk rock analysis for 2003-2017 products. C_0 was assumed as the bulk rock composition of 2003 light pumice (lp_05/04/2003; Fig. 1), whereas D_{Zr} and D_{Cr} were used to invert the trace element concentrations in clinopyroxene from the C_l melt chemistry throughout the fractionation process. Fig. 8 shows that the *FC* vector (red line) does not fully replicate the clinopyroxene analyses for values of F ranging from 1 to 0.79. The concentration of Zr remains almost constant during the very early stages of fractionation (F = 0.98; Table 4S). In contrast, Cr content abruptly decreases following a much sharper trajectory than the internal Cr-Zr variability described by the natural clinopyroxenes (Fig. 8; Table 4S). Therefore, the *FC* equation fails to reproduce the observed smooth, gradual trace element trajectories defined by clinopyroxene zones. Indeed, the development of a crystal mush upon magma solidification is one of the most effective mechanisms to explain the textural and compositional characteristics of the erupted phenocrysts. If a crystal mush is present, there is a general consensus that magmatic differentiation is directly connected with the development of a solidification front (Marsh, 1996, 2002), and that the interplay between magma differentiation and crystal-melt separation ultimately controls the compositional and textural variability of erupted products (e.g., Hildreth and Wilson, 2007; Masotta et al., 2010, 2016; Jackson et al., 2018). The inability to reproduce our data using the simple Rayleigh *FC* equation suggests that at the solidification front developing at the interface between the crystal mush and free melt, differentiated interstitial melts are produced, extracted and mixed with the reservoir melt (cf. Bachmann and

Bergantz, 2004; Huber et al., 2009; Dufek and Bachmann, 2010; Cashman and Blundy 2013). Moreover, the almost constant major element composition of the erupted shoshonitic basalts precludes a pure Rayleigh *FC* process (White, 2013 and references therein). To overcome this limitation, we apply the *in situ* crystallization equation proposed by Langmuir (1989), which accounts for the contribution of residual melts trapped/extracted from the crystal mush, leading to modulated enrichments/depletions of incompatible/compatible trace elements:

$$C_l = C_0 \times F^{\left[\frac{f(D-1)}{D(1-f)+f}\right]} \quad (2)$$

For a given degree of crystallization (1 - F), f is the fraction of residual melt returned from the solidification front to the magmatic reservoir. If f = 0, no interstitial melt migrates from the solidification front towards the free melt and the entire crystallization occurs within the solidification front. In contrast, if f = 1 all the interstitial melt returns to the free melt and Eqn. (2) reduces to the simple form of Eqn. (1) corresponding to the Rayleigh *FC* trajectory showed in Fig. 8. The trace element variability observed for the diopsidic-augitic clinopyroxene portions is most closely reproduced for f values between 0.8 and 0.5 (Fig. 8; Table 5S; cf. Jackson et al., 2018). This modeling approach is corroborated by the increase in incompatible trace elements with increasing proportion of interstitial melt from the solidification front (Fig. 8; Table 5S).

The geochemical evolution of clinopyroxene is therefore governed by open-system phenomena due to frequent mafic magma recharge (i.e., diopsidic bands) and mixing plus fractional crystallization (i.e., augitic overgrowths) intimately related to mush dynamics involving remobilization and recycling of early-formed phenocrysts (i.e., diopsidic antecrysts). Continuous *lp*-replenishment of the shallow plumbing system keeps the concentration of incompatible trace elements in the augitic mantles in the range of ~30-70 ppm Zr (Fig. 8). Diopsidic antecrysts from the 2003 paroxysm show maximum Cr levels (~11,000 pm), while the trace element composition of

recharge bands is intermediate between that of cores and mantles (Fig. 8). This confirms that the mafic *lp*-basalts injected into the shallow *hp*-reservoir carried primitive early cores and underwent partial hybridization with interstitial melts from the solidification front during upward migration of the magma through the mush column (Fig. 8; Francalanci et al., 2005, 2012; Petrone et al., 2018). These geochemical features are supported by the textures of phenocrysts from 2003 paroxysm showing Cr-rich diopsidic bands systematically enclosed within augitic mantles (Fig. 8). In contrast, no Cr-rich bands are found in clinopyroxenes erupted during the 2007 paroxysm, despite the bulk rock data showing Mg# and Cr peaks (Fig. 1c) caused by a further recharge event, as documented by Landi et al. (2009). The concentration of Cr in 2007 resorbed cores is also about two-three times lower than that measured in the 2003 antecrysts (Fig. 8), pinpointing protracted magma homogenization which lasted for 4 years until the less energetic paroxysm of 2007. This is also consistent with the decreasing difference in bulk rock compositions between light pumice and black scoria erupted from 2003 to 2007 (Fig. 1c). Similarly, over a much shorter temporal scale of 45 days, chemical homogenization effects are observed for both bulk rocks (Fig. 1c) and antecrysts (Fig. 8) from the 01/11/2017 major eruption to the normal activity of 15/12/2017. Phenocrysts with diopsidic bands are found in 05/04/2003 paroxysm, 24/05/2013 normal and 01/11/2017 major eruptions (Fig. 8), but their bulk rock data show clear recharge events only in 2003 and 2017 (Fig. 1c). In addition, the recharge texture of 2003 clinopyroxenes is rather different from that of 2013 and 2017 phenocrysts, showing diopsidic recharge bands systematically surrounding antecrysts, but never present within phenocryst mantles (Fig. 8). Thus, it is apparent that the diopsidic bands were fed by an antecryst-bearing mafic magma rising from depth, whereas thick augitic overgrowths developed over prolonged periods of crystallization within the homogeneous *hp*-reservoir. It is worth noting that both textures characterize the erupted products of the Early Paroxysm of the Present-day activity, but less frequent during the previous Post-Pizzo period (Petrone et al., 2018).

5.3. Crystal residence timescales via diffusion modelling of diopsidic-augitic boundaries

Antecryst recycling and diopsidic band formation constrain the temporal evolution of pre-eruptive magma dynamics over recurrent episodes of mafic magma replenishment and mush cannibalization (Petrone et al., 2016, 2018; Ubide and Kamber, 2018; Ubide et al., 2019b). In this context, Fe-Mg compositional zoning profiles in clinopyroxene phenocrysts from 2003-2017 eruptions were examined to quantify crystal residence times (Table 6S) via elemental diffusion chronometry (e.g., Morgan et al., 2004; Costa and Morgan, 2011) using the NIDIS (Non-Isothermal Diffusion Incremental Step) model of Petrone et al. (2016). The NIDIS model allows to calculate the total clinopyroxene residence time (Δt) by estimating the temporal interval between the formation of the diopsidic band (or the entrapment of the diopsidic antecryst) and the eruption. $\Delta t = \Delta t_1 + \Delta t_2$, where Δt_1 is the partial diffusive time after the early formed compositional boundary (i.e., internal mantle-diopsidic band) at the higher T of the diopsidic band, whereas Δt_2 is the diffusive time, at the lower T, after the last formed compositional boundary (i.e., diopsidic band-external mantle, or resorbed core-mantle in the case of antecrysts) until eruption (see Petrone et al., 2016 for further details). According to the NIDIS model, Δt is calculated by a backward approach from the last-formed compositional boundary (Δt_2) inward (i.e., Δt_1). Following this reasoning, we have adapted the NIDIS model to resolve the different zoning patterns of the 2003-2017 clinopyroxenes and calculate pre-eruptive crystal residence times. The greyscale level of clinopyroxene from BSE-microphotographs is deconvoluted by NIDIS in a Fe-Mg compositional zoning profile (Petrone et al., 2016). Greyscale values were recovered along transects normal to the {1 0 0} sector, perpendicular to the *c*-axis (Fig. 4S). Fe-Mg diffusion coefficients were calculated at 1,130 and 1,165 °C for mantle and diopsidic band, respectively, following thermometry results (Fig. 7 and 3S) and using the pre-exponential factor and the activation energy reported in Dimanov and Sautter (2000).

Diopsidic bands surrounding patchy cores in Sub-group A1 can be modeled only for a partial residence time corresponding to Δt_2, from the last recharge event to eruption (Fig. 8), due to the lack of clear patchy core-diopsidic band boundaries (Fig. 4S). Phenocrysts erupted in 2003 do not show

diopsidic bands surrounding resorbed cores, but sometimes they show a diopsidic band in the augitic mantle testifying a further input of mafic magma subsequent to the remobilization of the antecryst core (Fig. 8). Therefore, it should be possible to calculate timescales either at the resorbed core-inner mantle interface (Δt_2) or across the diopsidic band (Δt). However, in our specific case, the diopsidic band is extremely thin (< 35 µm) and cannot be modeled. As a consequence, only the timescales of the resorbed core-inner mantle interface can be calculated. This correspond to a partial timescale determined at the low-*T* of the augitic mantle. Considering the dynamics of Stromboli where inputs of mafic magma are quickly stirred into the *hp*-resident magma (Petrone et al., 2018), we can assume that the diffusive time of a thin diopsidic band is negligible in respect with the diffusive time of the antecryst-mantle boundary. Therefore, also in this case we can calculate Δt_2 which represents the minimum remobilization time of antecrysts (i.e., the shortest travel time from the *lp*- to *hp*-reservoirs) before eruption (Fig. 8).

Correspondingly, because of the lack of recharge bands within the mantle, the Sub-group A2 provides information on the remobilization time Δt_2 of diopsidic antecrysts only (Fig. 8), but in this case there was any further recharge event before the eruption and the Δt_2 correspond with the total residence time. Clinopyroxenes from Sub-group B1 (Fig. 4S) are characterized by a steeper greyscale gradient on the left-hand side of the diopsidic band (i.e., toward the core) which cannot be explained by Fe-Mg diffusion. In fact, in a pure diffusion profile the internal compositional boundary should be smoother than the external having experienced diffusion for longer time. This case is similar to the 'anomalous' profile showed by a limited number of clinopyroxenes from the Post-Pizzo and Early Paroxysm and described by Petrone et al. (2018). Compositional profiles of this type can still provide some valuable timescale information. Adapting the NIDIS model (Petrone et al., 2016) and following the reasoning of Petrone et al. (2018), we calculated a pseudo-timescale (i.e., Δt_4 rather than Δt_1, see Petrone et al., 2016, 2018) to reproduce the core-diopsidic band boundary assuming that it formed entirely at the high-T of the diopsidic band. This partial timescale clearly represents a minimum

timescale from the injection of the mafic magma in the *hp*-reservoir to eruption. Clinopyroxenes from Sub-group B2 cannot be modelled since no Fe-Mg compositional boundaries (i.e., no timescales) are found (Fig. 8).

Crystal residence times were calculated on eleven phenocrysts representative of the 2003-2017 populations (Table 6S) and appear to reflect the textural features of the clinopyroxenes. Specifically, very short timescales of <1 year (minimum timescale of 6 months) are measured for the injection of diopsidic *lp*-magma for the 2003 paroxysm (Fig. 8), documenting restricted temporal intervals between mafic injection in the *hp*-reservoir and subsequent eruption. In contrast, longer timescales on the order of ~11-32 years are calculated for diopsidic recharge bands surrounding the resorbed antecrysts of the 2017 major event (Fig. 8). These timescales are also within the range of ~4-182 years measured for the remobilization of diopsidic antecrysts (Fig. 8). In general, the remobilization time of antecrysts appear to increase from the 2003 (i.e., years-decades) violent paroxysm to 2017 (decades-hundreds years) eruptions. From a statistical point of view, the rapid injection of abundant mafic magmas before or during the 2003 paroxysm involved antecrysts that were transported rapidly from the *lp*- to *hp*-reservoirs (Fig. 8). The connection between these two reservoirs has been observed by a temporal decrease of Sr isotope ratios in products erupted starting from 1980 CE, in response to the injections of less radiogenic *lp*-magmas into the shallow *hp*-reservoir (Francalanci et al., 1999). This trend is also accompanied by high Sr isotope ratios of antecrysts (0.70630-0.70635 $^{87}Sr/^{86}Sr$), even with respect to the groundmass (0.706157-0.706248 $^{87}Sr/^{86}Sr$). According to Francalanci et al. (2005), the disequilibrium between antecrysts and melts suggests the presence of a crystal mush close to the Pizzo activity (~2.4 kyr; Francalanci et al., 1988, 1989; Ubide et al., 2019b). The subsequent Post-Pizzo period is characterized by rapid *lp*-*hp* homogenization (Petrone et al., 2018), with the occurrence of abundant diopsidic bands (i.e., mafic recharge events) and sporadic diopsidic antecrysts (i.e., mush recycling). As showed by Petrone et al. (2008), crystal residence times from mafic injections to eruptions are systematically higher than *lp*-*hp* homogenization processes, thus attesting to (since the age of Post-Pizzo) efficient mixing regime

and steady-state magma dynamics within the vertically-developed plumbing system (Fig. 9a). In detail, the efficiency of *lp-hp* mixing increases from the base (1 day-9 years) to the top of the Post-Pizzo sequence (1 day-8 months), possibly due to a decrease in the volume of injected magma (Fig. 9a). Clinopyroxenes from the Early Paroxysms of the Present-day activity record *lp-hp* homogenization timescales of 6 months-2 years (cf. Petrone et al., 2018). As discussed above, it was impossible to calculate homogenization timescales for the 2003-2017 activity. However, considering the presence of thin diopsidic bands in 2003 Sub-group A1 clinopyroxene and the minimum timescale of the internal portions of 2003 Sub-group B1 diopsidic bands (i.e., 0.5 years), we can suggest similar short timescales (Fig. 9b). The increasing amount of resorbed antecrysts over time, coupled with the lower proportion of diopsidic bands, suggest that the volume of magma injections from the *lp*-reservoir decreases, while increasing the remobilization of older portion of the crystal mush. Therefore, the minimum remobilization time provided by the resorbed antecrysts is always longer than the temporal interval between mafic injections triggering the studied eruptive sequence (Figs. 8 and 9).

During the Post-Pizzo period (Fig. 9a), the occurrence of abundant diopsidic bands is directly related to quasi-instantaneous timescales (<1 day to 4 months) caused by rapid injections of fresh *lp*-magmas triggering the eruption (Petrone et al., 2018). This means that mafic *lp*-magmas do not stall within the crystal mush over prolonged times and a limited amount of antecrysts are transported into the shallow *hp*-reservoir (Fig. 9a). In contrast, during the Early Paroxysm recycled antecrysts are common whereas clinopyroxenes with diopsidic rims are extremely rare (Petrone et al. 2018). As already illustrated by Landi et al. (2009) and Francalanci et al. (2012), recycled antecrysts are almost ubiquitous in the Present-day products and periodically transferred into the *hp*-reservoir by *lp*-magmas permeating the old crystal mush. In fact, the increased occurrence of resorbed antecrysts from 2003 to 2017 seems to couple with a progressive disappearance of diopsidic bands and a total absence of diopsidic rims, independent of the eruptive style (Fig. 8). This suggests that the 2003-2017 activity represents a new phase in the life evolution of Stromboli volcano (Fig. 9b), characterized by

more efficient mechanisms of mush disruption and cannibalization, in which the old diopsidic antecrysts are continuously remobilized and transported by the *lp*-magmas permeating the mush (Fig. 9b). At the same time, the disappearance of diopsidic recharge bands (Fig. 8) suggests that injections feeding the persistent Present-day activity (Taddeucci et al., 2013) are efficiently mixed and homogenized. This is further supported by the gradual variation in Cr contents in augitic mantles and rims (Figs. 3 and 1S) as well as at the bulk rock scale (Fig. 1), owing to ongoing magma mixing phenomena.

5.4. Dynamics of mush formation and remobilization

The ubiquitous occurrence of sector zoned phenocrysts within the 2003-2017 products implies that clinopyroxene growth is strongly controlled by kinetic effects imposed by the degree of undercooling ($\Delta T = T_{liquidus} - T_{crystallization}$) in the plumbing system (Mollo and Hammer, 2017; Ubide et al., 2019a, 2019b). In this regard, several natural and experimental studies document that partitioning kinetics may produce compositional contrasts between the hourglass {-1 1 1} and prism {1 0 0} sectors (e.g., Hollister and Gancarz, 1971; Ferguson, 1973; Downes, 1974; Leung, 1974; Dowty, 1976; Duncan and Preston, 1980; Shimizu, 1981; Watson and Liang, 1995; Brophy et al., 1999; Hammer et al., 2016; Welsch et al., 2016; Ubide et al., 2019a, 2019b). According to the experimental work of Kouchi et al. (1983), the magnitude of {-1 1 1}/{1 0 0} ratio for major cations scales with the degree of undercooling, providing that the exchange $[Si + Mg]_{-111} \leftrightarrow [Al + Ti]_{100}$ is controlled by ΔT = 13-25 °C. At Stromboli, magmas residing within the shallow *hp*-reservoir undergo prolonged periods of passive (non-explosive) degassing (Allard et al., 1994; Lautze and Houghton, 2005, 2007), which could induce reservoir convection and hence sluggish kinetic effects favoring crystallization (e.g., Métrich et al., 2001, 2005, 2010; Bertagnini et al., 2003, 2008) with sector zoning (Ubide et al., 2019b; Fig. 9b). Clinopyroxene growth under near-equilibrium conditions is supported by mineral-melt modeling of ΔDiHd, ΔD_{Na} and ΔD_{Ti} (Fig. 6). Similarly, low degrees of undercooling

and analogous equilibrium cation exchanges were recorded by sector-zoned clinopyroxene megacrysts erupted during the Pizzo activity (Ubide et al., 2019b) and sector-zoned phenocrysts from 1974, 2002 and 2003 products at Mt. Etna volcano (Ubide et al., 2019a).

Although abundant crystallization and accumulation of clinopyroxene phenocrysts are texturally and isotopically envisaged at shallow depths (Francalanci et al., 2005, 2012), crystal-rich enclaves typical of thick cumulate horizons (e.g., Tecchiato et al., 2018a, 2018b) are not found in the studied products. The absence of a textural maturation (i.e., porphyritic-holocrystalline transition) excludes crystal settling as the principal deposition mechanism and strengthens the *in situ* crystallization scenario (Fig. 8) during the early growth stage of the solidification front (cf. Bachmann and Bergantz, 2004; Masotta et al., 2016). We propose that continuous injections of mafic *lp*-magmas mix with the more differentiated mush melts migrating into the shallow reservoir (~2-4 km depth; e.g., Métrich et al., 2010), thus preserving the shoshonitic uniformity of the *hp*-magma (Fig. 9b). According to textural features (Figs. 3 and 1S) and isotopic compositions of phenocrysts (Francalanci et al., 2005, 2012), the old diopsidic antecrysts represent relics of the remobilized portions of the crystal mush caused by forceful inputs of *lp*-magmas from depth (Fig. 9b). On this basis, we have employed the equation of Bachmann and Bergantz (2004) to constrain the spatial distribution and physical state of the solidification front in terms of thickness and compaction:

$$t_h = \frac{Z_0}{W_0(1-\Phi)} \quad (3)$$

where t_h (s) is the time required to segregate melts via mush compaction, Z_0 is the thickness of the solidification front, W_0 (m/s) is the relative velocity between the segregated melt and the crystalline mush (i.e., the melt migration velocity), and Φ corresponds to the porosity of the crystal mush. In the case of highly porous mushy bodies, for W_0 changes of approximately one order of magnitude from 10^{-10} to 10^{-9} m/s due to compaction, Φ is within the range 0.4-0.5 (McKenzie, 1984, 1985; Shirley,

1986; Bachmann and Bergantz, 2004) and t_h may be approximated as the lifetime of the mush complex (~2.4 kyr; Francalanci et al., 1988). Consistent with this logic, we calculate that the maximum value of Z_0 is ~400 m (Fig. 10a; Table 7S), in accordance with the thin solidification fronts typical of shallow reservoirs characterized by an intricate architecture of magma ponding zones (Scandone and Acocella, 2007; Masotta et al., 2016).

It is broadly accepted that the upward extraction of interstitial melts may also be related to the failure and detachment of the growing crystal structure at the roof of the solidification front (Humphreys and Holness, 2010; Marsh, 1996, 2002, 2007; Masotta et al., 2012, 2016; Shibano et al., 2012). This process depends on the balance between the increasing weight and strength of the crystalline network during the advancement of the solidification front. According to Marsh (2002), the counterbalancing effects of these two opposite forces can be quantified as:

$$\frac{\Delta\rho g z_0}{\sigma_c} = \frac{ln(\varphi/\varphi_0)}{z_p} \quad (5)$$

where σ_c (bar) is the local strength, $\Delta\rho$ (kg/m^3) is the density contrast between the crystal mush and magma at any point along the solidification front z_p (z/z_0), φ is the crystal fraction and φ_0 is the initial crystallinity, which is ~0.25 for basaltic compositions (Philpotts et al., 1996). By rearranging equation (5), it is possible to calculate the threshold value of σ_c required to prevent gravitational instability and tearing of the crystal mush at any point (z_p) along the solidification front. It is worth stressing that z_p is proportional to the crystal fraction φ_{zp} (φ/φ_0), as a function of the temperature gradient along the solidification front. In this regard, the experimental study of Masotta et al. (2012) quantitatively describes the relationship between these two parameters as follows:

$$\varphi_{zp} = 0.75 \times z_p + 0.25 \quad (6)$$

If φ is lower than φ_0 (0.25), the magmatic system can be considered in a suspension state in which crystal settling is the sole gravitational mechanism. Conversely, if φ ranges from 0.25 to 0.50, the system moves towards a mush state where compaction becomes the main gravitational process. Further increments of crystallinity (φ > 0.50) give more strength to the mush and exacerbate the density contrast between residual melt and solid. This causes gravitational instability of the crystal network with tearing or collapse of the overlying crystalline roof (cf. Marsh, 2002; Masotta et al. 2012, 2016). According to the model of Marsh (2002), redrawn in Fig. 10b, values of $Z_0 \leq 400$ m and $\varphi \leq 0.6$ yield a characteristic strength of 0.3-2 bars (Table 7S), denoting tearing and disruption phenomena of the solidification front within the shallow *hp*-reservoir. The validity of this instability model is corroborated by the modest but persistent seismicity ascribed to the shear-failure of the mush (Falsaperla and Spampinato, 1999; Burton et al., 2007; Bonaccorso et al., 2008). Detachment of the growing crystal structure at the roof of the solidification front provides a mechanism for the extraction of voluminous mush melts (Humphreys and Holness, 2010; Marsh, 1996, 2002, 2007; Masotta et al., 2012, 2016; Shibano et al., 2012), in agreement with the *in situ* crystallization model (i.e., f = 0.5-0.8; Fig.8) estimating that ~50-80% of the total interstitial melt migrates from the crystal mush towards the free magma. Generally, strength calculations from this study are found for shallow sill-shaped magmatic reservoirs in which the rate of tear opening is related to local cooling paths (Marsh, 1996, 2002; Masotta et al., 2012, 2016). Conductive cooling models for sill-shaped magmatic reservoirs (e.g., Ubide et al., 2012; Rodríguez et al., 2015) together with MELTS crystallinity modeling (Masotta, 2012) highlight that thin solidification fronts (200-400 m) experiencing failure and instability phenomena are associated with cooling timescales of 10^3-10^4 years, consistent with mush residence time estimates at Stromboli (Francalanci et al., 1988, 1989; Ubide et al., 2019b).

6. Concluding remarks

We have investigated the textural and chemical complexities of the 2003-2017 eruptions at Stromboli volcano by combining bulk rock compositions with quantitative analyses and mapping of

major and trace elements in clinopyroxene phenocrysts. Our novel analytical data, together with crystal residence timescales estimated through Fe-Mg diffusion and physical modeling of the crystal mush, are used to better define the temporal evolution of the plumbing system and the crystallization conditions of magma ascending into a vertically-extended mush column. Our results open new petrological and volcanological perspectives into the investigation of pre-eruptive magma dynamics at Stromboli and other steady-state volcanoes. We summarize the following conclusions:

1) Clinopyroxene phenocrysts show complex zoning patterns with diopsidic antecryst cores and diopsidic bands overgrown by augitic mantles and rims, in which both sector and oscillatory zoning develop. The concentrations of incompatible trace elements (i.e., REE, Zr, Yb) and Sc are higher in mantle and rim portions with respect to antecryst cores and diopsidic bands. Appreciable trace element changes are also observed in relation to prism vs. hourglass sectors;
2) Textural characteristics and compositional zoning in clinopyroxene phenocrysts indicate multi-stage crystallization across the Stromboli *lp*-*hp*-reservoirs, where diopsidic antecrysts and bands are markers of more primitive, high-*T* magma injections into the shallow, low-*T* plumbing system. Resorbed diopsidic cores testify to the continuous disruption and cannibalization of the old crystal mush at different depths. The concentrations of low charged trace metals (e.g., Cr, Ni) increase in diopsidic bands and cores, accounting for mafic recharge events and magma mixing processes. Conversely, high charged cations (e.g., Al, REE) track the kinetic growth of sector zoned crystals under conditions of low magma undercooling;
3) *P*-*T*-H_2O estimates provide an almost constant crystallization path over fourteen years of volcanic activity. The augitic mantles and rims form at low-*T* (~1,130 °C), whereas diopsidic cores and bands equilibrate at high-*T* (~1,175 and ~1,165 °C, respectively). Overall, these different crystal portions developed at the same *P* (160-190 MPa) and H_2O

(0.5-2.4 wt.%) conditions; crystallization depths agree, within error, with the depths of the *lp*-*hp*-reservoirs and the intermediate segment of the plumbing system;

4) By assuming that Cr and Zr concentrations in clinopyroxene reflect compatible and incompatible behavior during *in situ* crystallization phenomena, we have estimated that 80-50% of residual melts are extracted from the solidification front of the crystal mush and return to the magma reservoir;
5) Very short timescales (~1 year) are estimated for the diffusive re-equilibration of compositional zoning across diopsidic bands from the 2003 paroxysm, documenting restricted temporal intervals between mafic injections in the *hp*-reservoir and subsequent eruption. Longer timescales (~11-32 years) are calculated for diopsidic recharge bands surrounding the resorbed antecrysts and are within the range of ~4-182 years measured for the diopsidic antecrysts. The remobilization time of antecrysts increases from the 2003 (years-decades) paroxysm to the 2017 (decades-hundred years) eruptions, indicating that these relic crystals were transported within the mush column over longer periods of time and/or remobilized older portion of the mush;
6) Injections of mafic *lp*-magmas persistently mix with the more differentiated mush melts migrating into the shallow reservoir, thus preserving the shoshonitic uniformity of the *hp*-magma. By interpolating spatial distribution and physical state parameters, we have calculated a maximum thickness of 400 m for the solidification front, in close agreement with those measured for shallow and relative young reservoirs. Upward extraction of interstitial melts is also related to failure and detachment of the growing crystal structure at the roof of the solidification front, alongside modest but persistent seismicity ascribed to the shear-failure of crystalline bodies.

7. Acknowledgements

We acknowledge funding from The University of Queensland (ECR grant UQECR1717581 and MRFF grant RM2016000555 to TU), the Australian Geoscience Council and the Australian Academy of Science (34th IGC Travel Grant to TU), and PRIN MIUR (grant # 2017J277S9_004 to EDB and FDS) “Time scales of solidification in magmas: Applications to Volcanic Eruptions, Silicate Melts, Glasses, Glass-Ceramics”. We thank the HP-HT laboratory of Experimental Geophysics and Volcanology (INGV Rome) and EPOS TCS MSL for access to electron microprobe analysis. S. Brizzi is acknowledged for providing help with the Matlab code.

References

Agostini, C., Fortunati, A., Arzilli, F., Landi, P., Carroll, M.R., 2013. Kinetics evolution as a probe to magmatism at Stromboli (Aeolian Archipelago, Italy). Geochim. Cosmochim. Acta, 110, 135-151.

Aiuppa, A., Burton, M., Caltabiano, T., Giudice, G., Guerrieri, S., Liuzzo, M., Murè, F., Salerno, G., 2010. Unusually large magmatic CO_2 gas emissions prior to a basaltic paroxysm. Geophys. Res. Lett., 37, L17303.

Albarède, F., Luais, B., Fitton, G., Semet, M., Kaminski, E., Upton, B.G.J., Bachèlery, P., Cheminée, J.L., 1997. The geochemical regimes of Piton de la Fournaise volcano (Réunion) during the last 530,000 years. J. Petrol., 38, 171-201.

Allard, P., Aiuppa, A., Loyer, H., Carrot, F., Gaudry, A., Pinte, G., Michel, A., Dongarrà, G., 2000. Acid gas and metal emission rates during long-lived basalt degassing at Stromboli volcano. Geophys. Res. Lett., 27, 1207-1210.

Allard, P., Carbonnelle, J., Métrich, N., Loyer, H., Zettwoog, P., 1994. Sulphur output and magma degassing budget of Stromboli volcano. Nature, 368, 326-330.

Andronico, D., Pistolesi, M., 2010. The November 2009 paroxysmal explosions at Stromboli. J. Volcanol. Geotherm. Res. 196, 120-125

Andronico, D., Taddeucci, J., Cristaldi, A., Miraglia, L., Scarlato, P., Gaeta, M., 2013. The 15 March 2007 paroxysm of Stromboli: video-image analysis, and textural and compositional features of the erupted deposit. Bull. Volcanol. 75, 733

Armienti, P., Perinelli, C., Putirka, K.D., 2013. A new model to estimate deep-level magma ascent rates, with applications to Mt. Etna (Sicily, Italy). J. Petrol. 54, 795-813

Armienti, P., Francalanci, L., Landi, P., 2007. Textural effects of steady state behaviour of the Stromboli feeding system. J. Volcanol. Geotherm. Res. 160, 86–98.

Arrighi, S., Rosi, M., Tanguy, J.C., Courtillot, V., 2004. Recent eruptive history of Stromboli (Aeolian Islands, Italy) determined from high-accuracy archeomagnetic dating. Geophys. Res. Lett., 31, L19603.

Bachmann, O., Bergantz, G.W., 2008. Deciphering magma chamber dynamics from styles of compositional zoning in large silicic ash flow sheets. Rev. Mineral. Geochem., 69, 651-674.

Bachmann, O., Bergantz, G.W., 2004. On the origin of crystal-poor rhyolites: extracted from batholithic crystal mushes. J. Petrol., 45, 1565-1582.

Bachmann, O., Dungan, M.A., Lipman, P.W., 2002. The Fish Canyon magma body, San Juan volcanic field, Colorado: rejuvenation and eruption of an upper crustal batholith. J. Petrol., 43, 1469-1503.

Barberi, F., Civetta, L., Rosi, M., Scandone, R., 2009. Chronology of the 2007 eruption of Stromboli and the activity of the Scientific Synthesis Group. J. Volcanol. Geotherm. Res. 182,123-130.

Barberi, F., Rosi, M., Sodi, A., 1993. Volcanic hazard assessment at Stromboli based on a review of historical data. Acta Volcanol., 3, 173-187.

Bertagnini, A., Métrich, N., Francalanci, L., Landi, P., Tommasini, S., Conticelli, S., 2008. Volcanology and Magma Geochemistry of the Present-day Activity: Constraints on the Feeding System. In: “Learning from Stromboli and its 2002-2003 Eruptive Crisis”, Calvari, S., Rosi, M., and Ripepe, M. (eds). American Geophysical Union-Geophysical Monograph volume.

Bertagnini, A., Métrich, N., Landi, P., Rosi, M., 2003. Stromboli volcano (Aeolian Archipelago, Italy): an open window on the deep-feeding system of a steady state basaltic volcano. J. Geophys. Res., 108, 2326.

Bertagnini, A., Coltelli, M., Landi, P., Pompilio, M., Rosi, M., 1999. Violent explosions yield new insights into dynamics of Stromboli volcano. Eos, Transactions American Geophysical Union 80, 633-636.

Biggs, J., Pritchard, M.E., 2017. Global volcano monitoring: what does it mean when volcanoes deform? Elements, 13, 17-22.

Blundy, J.D., Falloon, T.J., Wood, B.J., Dalton, J.A., 1995. Sodium partitioning between clinopyroxene and silicate melts. J. Geophys. Res. Solid Earth 100, 15501-15515.

Bonaccorso, A., Calvari, S., 2013. Major effusive eruptions and recent lava fountains: balance between expected and erupted magma volumes at Etna volcano. Geophys. Res. Lett.40, 6069-6073.

Bonaccorso, A., Gambino, S., Guglielmino, F., Mattia, M., Pugliesi, G., Boschi, E., 2008. Stromboli 2007 eruption: deflection modeling to infer shallow-intermediate plumbing system. Geophys. Res. Lett., 35, L06311.

Bonaccorso, A., Calvari, S., Garfi, G., Lodato, L., Patane, D., 2003. Dynamics of the December 2002 flank failure and tsunami at Stromboli volcano inferred by volcanological and geophysical observations. Geophys. Res. Lett., 30, 1941.

Bragagni, A., Avanzinelli, R., Freymuth, H., Francalanci, L., 2014. Recycling of crystal mush-derived melts and short magma residence times revealed by U-series disequilibria at Stromboli volcano. Earth Planet. Sci. Lett., 404, 206-219.

Brophy, J.G., Whittington, C.S., Park, Y.R., 1999. Sector zoned augite megacrysts in Aleutian high alumina basalts: implications for the conditions of basalt crystallization and the generation of calc-alkaline series magmas. Contrib. Mineral. Petrol., 135, 277-290.

Burgisser, A., Bergantz, G.W., 2011. A rapid mechanism to remobilize and homogenize highly crystalline magma bodies. Nature, 471, 212.

Burton, M.R., Mader, H.M., Polacci, M., 2007. The role of gas percolation in quiescent degassing of persistently active basaltic volcanoes. Earth Planet. Sci. Lett., 264, 46-60.

Calvari, S., Spampinato, L., Lodato, L., Harris, A.J.L., Patrick, M.R., Dehn, J., Burton, M.R., Andronico, D., 2005. Chronology and complex volcanic processes during the 2002–2003 flank eruption at Stromboli volcano (Italy) reconstructed from direct observations and surveys with a handheld thermal camera. J. Geophys. Res. 110, B02201.

Calvari, S., Lodato, L., Steffke, A., Cristaldi, A., Harris, A.J.L., Spampinato, L., Boschi, E., 2010. The 2007 Stromboli eruption: event chronology and effusion rates using thermal infrared data. J. Geophys. Res. 115, B04201.

Cashman, K., Blundy, J.D., 2013. Petrological cannibalism: the chemical and textural consequences of incremental magma body growth. Contrib. Mineral. Petrol., 166, 703-729.

Cashman, K.V., Sparks, R.S.J., Blundy, J.D., 2017. Vertically extensive and unstable crystals mushes: a unifying view of igneous processes associated with volcanoes. Science, 355, 6331-3055.

Chouet, B., Dawson, P., Ohminato, T., Martini, M., Saccorotti, G., Giudicepietro, F., De Luca, G., Milana, G., Scarpa, R., 2003. Source mechanisms of explosions at Stromboli volcano, Italy, determined from moment tensor inversions of very-long-period data. J Geophys. Res., 108, 2109.

Costa, F., Morgan, D., 2011. Time constraints from chemical equilibration in magmatic crystals. In: "Timescales of magmatic processes: From core to atmosphere", Dosseto, A., Turner, S.P., Van Orman, J.A. (eds). Blackwell Publishing Ltd.

D'Orazio, M., Armienti, P., Cerretini, S., 1998. Phenocryst/matrix trace-element partition coefficients for hawaiite-trachyte lavas from the Ellittico volcanic sequence (Mt. Etna, Sicily, Italy). Min. Pet. 64., 65-88.

Davidson, J.P., Morgan, D.J., Charlier, B.L.A., Harlou, R., Hora, J.M., 2007. Microsampling and isotopic analysis of igneous rocks: implication for the study of magmatic systems. Annu. Rev. Earth Planet. Sci., 35, 273-311.

Dimanov, A., Sautter, V., 2000. "Average" interdiffusion of (Fe,Mg)-Mn in natural diopside. Eur. J. Mineral., 12, 749-760.

Downes, M.J., 1974. Sector and oscillatory zoning in calcic augites from M. Etna, Sicily. Contrib. Mineral. Petrol., 47, 187-196.

Dowty, E., 1976. Crystal structure and crystal growth: II. Sector zoning in minerals. Am. Mineral., 61, 460-469.

Dufek, J., Bachmann, O., 2010. Quantum magmatism: magmatic compositional gaps generated by melt-crystal dynamics. Geology, 38, 687-690.

Duncan, A.M., Preston, R.M.F., 1980. Chemical variation of clinopyroxene phenocrysts from the trachybasaltic lavas of Mount Etna, Sicily. Min. Mag., 43, 765-770.

Falsaperla, S., Spampinato, S., 2003. Seismic insights into explosive paroxysm at Stromboli volcano, Italy. J. Volcanol. Geotherm. Res., 125, 121-137.

Ferguson, A.K., 1973. On hour-glass sector zoning in clinopyroxene. Min. Mag., 39, 321-325.

Francalanci, L., Braschi, E., Di Salvo, S., Lucchi, F., Petrone, C.M., 2014. When magmas do not interact: paired Roman-age activity revealed by tephra studies at Stromboli volcano. Bull. Volcanol., 76, 884.

Francalanci, L., Lucchi, F., Keller, J., De Astis, G., Tranne, C.A., 2013. Eruptive, volcano-tectonic and magmatic history of the Stromboli volcano (north-eastern Aeolian archipelago). In: Geol. Soc. Lond. Mem., 37, 397-471.

Francalanci, L., Avanzinelli, R., Nardini, I., Tiepolo, M., Davidson, J.P., Vannucci, R., 2012. Crystal recycling in the steady-state system of the active Stromboli volcano: a 2.5-ka story inferred from in situ Sr-isotope and trace element data. Contrib. Mineral. Petrol., 163, 109-131.

Francalanci, L., Bertagnini, A., Métrich, N., Renzulli, A., Vannucci, R., Landi, P., Del Moro, S., Menna, M., Petrone, C.M., Nardini, I., (2008) Mineralogical, Geochemical and Isotopic Characteristics of the Ejecta from the 5 April 2003 Paroxysm at Stromboli, Italy: Inferences on the Eruptive Dynamics. In; "Learning from Stromboli and its 2002–2003 Eruptive Crisis", Calvari, S., Rosi, M., Ripepe, M. (eds). American Geophysical Union-Geophysical Monograph volume.

Francalanci, L., Davies, G.R., Lustenhouwer, W., Tommasini, S., Mason, P.R.D., Conticelli, S., 2005. Intra-grain Sr isotope evidence for crystal recycling and multiple magma reservoirs in the recent activity of Stromboli Volcano, Southern Italy. J. Petrol., 46, 1997-2021.

Francalanci, L., Tommasini, S., Conticelli, S., 2004. The volcanic activity of Stromboli in the 1906-1998 A.D. period: mineralogical, geochemical and isotope data relevant to the understanding of plumbing system. J. Volcanol. Geotherm. Res., 131, 179-211.

Francalanci, L., Tommasini, S., Conticelli, S., Davies, G.R., 1999. Sr isotope evidence for short magma residence time for the 20th century activity at Stromboli volcano, Italy. Earth Planet. Sci. Lett., 167, 61-69.

Francalanci, L., Manetti, P., Peccerillo, A., 1989. Volcanological and magmatological evolution of Stromboli volcano (Aeolian Islands): the roles of fractional crystallization, magma mixing, crustal contamination and source heterogeneity. Bull. Volcanol., 51, 355-378.

Francalanci, L., Barbieri, M., Manetti, P., Peccerillo, A., Tolomeo, L., 1988. Sr-isotopic systematics in volcanic rocks from the island of Stromboli (Aeolian arc). Chem. Geol., 73, 164-180.

France, L., Koepke, J., Ildefonse, B., Cichy, S. B., Deschamps, F., 2010. Hydrous partial melting in the sheeted dike complex at fast spreading ridges: experimental and natural observations. Contrib. Mineral. Petrol., 160, 683-704.

Giberti, G., Jaupart, C., Sartoris, G., 1992. Steady-state operation of Stromboli volcano, Italy: constraints on the feeding system. Bull. Volcanol., 54, 535-541.

Gillot, P.Y., Keller, J., 1993. Radiochronological dating of Stromboli. Acta Vulcanol., 3, 69-77.

Hammer, J., Jacob, S., Welsch, B., Hellebrand, E., Sinton, J., 2016. Clinopyroxene in postshield Haleakala ankaramite: 1. Efficacy of thermobarometry. Contrib. Mineral. Petrol., 171, 7-23.

Harris, A.J.L., Stevenson, D.S., 1997. Magma budgets and steady state activity of Vulcano and Stromboli. Geophys. Res. Lett., 24, 1043-1046.

Harris, A.J.L., Ripepe, M., Calvari, S., Lodato, L., Spampinato, L., 2008. The 5 April 2003 explosion of Stromboli: timing of eruption dynamics using thermal data. In: Calvari, S., Inguaggiato, S., Puglisi, G., Ripepe, M., Rosi, M. (eds). The Stromboli volcano-an integrated study of 2002-2003 eruption. American Geophysical Union, Geophysical Monograph Series, 182, 305-316.

Hildreth, W., Wilson, C.J., 2007. Compositional zoning of the Bishop Tuff. J. Petrol., 48, 951-999.

Hill, E., Blundy, J.D., Wood, B.J., 2011. Clinopyroxene-melt trace element partitioning and the development of a predictive model for HFSE and Sc. Contrib. Mineral. Petrol., 161, 423-438.

Hollister, L.S., Gancarz, A.J., 1971. Compositional sector zoning in clinopyroxene from the Narce area, Italy. Am. Mineral., 56, 959-979.

Hornig-Kjarsgaard, I., Keller, J., Koberski, U., Stadlbauer, E., Francalanci, L., Lenhart, R., 1993. Geology, stratigraphy and volcanological evolution of the island of Stromboli, Aeolian arc, Italy. Acta Vulcanol., 3, 21-68.

Huber, C., Bachmann, O., Manga, M., 2009. Homogenization processes in silicic magma chambers by stirring and mushification (latent heat buffering). Earth Planet. Sci. Lett., 283, 38-47.

Humphreys, M.C.S., Holness, M.B., 2010. Melt-rich segregations in the Skaergaard Marginal Border Series: tearing of a vertical silicate mush and the generation of magma chambers. Lithos, 119, 181-192.

Jackson, M.D., Blundy, J.D., Sparks, R.S.J., 2018. Chemical differentiation, cold storage and remobilization of magma in the Earth's crust. Nature, 564, 405.

Jarosewich, E., Nelen, J.A., Norberg, J.A., 1980. Reference samples for electron microprobe analysis. Geostandards Newsletter, 4, 43-47.

Kokelaar, P., Romagnoli, C., 1995. Sector collapse, sedimentation and clast population evolution at an active island-arc volcano: Stromboli, Italy. Bull. Volcanol., 57, 240-262.

Kouchi, A., Sugawara, Y., Kashima, K., Sunagawa, I., 1983. Laboratory growth of sector zoned clinopyroxenes in the system $CaMgSi_2O_6$-$CaTiAl_2O_6$. Contrib. Mineral. Petrol., 83, 177-184.

Kress, V.C., Carmichael, I.S., 1991. The compressibility of silicate liquids containing Fe_2O_3 and the effect of composition, temperature, oxygen fugacity and pressure on their redox states. Contrib. to Mineral. Petrol., 108, 82-92.

Landi, P., Corsaro, R. A., Francalanci, L., Civetta, L., Miraglia, R., Pompilio, M., Tesoro, R., 2009. Magma dynamics during the 2007 Stromboli Eruption (Aeolian Islands, Italy): mineralogical, geochemical and isotopic data. J. Volcanol. Geotherm. Res., 182, 255-268.

Landi, P., Métrich, N., Bertagnini, A., Rosi, M., 2008. Recycling and "re-hydration" of degassed magma inducing transient dissolution/crystallization events at Stromboli (Italy). J. Volcanol. Geotherm. Res., 174, 325-336.

Landi, P., Francalanci, L., Pompilio, M., Rosi, M., Corsaro, A., Petrone, C.M., Nardini, I., Miraglia, L., 2006. The December 2002-July 2003 effusive event at Stromboli volcano, Italy: insights into the shallow plumbing system by petrochemical studies. J. Volcanol. Geotherm. Res., 155, 263-284.

Landi, P., Métrich, N., Bertagnini, A., Rosi, M., 2004. Dynamics of magma mixing and degassing in plagioclase at Stromboli (Aeolian Archipelago, Italy). Contrib. Mineral. Petrol., 147, 213-227.

Langmuir, C.H., 1989. Geochemical consequences of in situ crystallization. Nature, 340, 199.

Lautze, N.C., Houghton, B.F., 2007. Linking variable explosion style and magma textures during 2002 at Stromboli volcano, Italy. Bull. Volcanol., 69, 445-460.

Lautze, N.C., Houghton, B.F., 2005. Physical mingling of magma and complex eruption dynamics in the shallow conduit at Stromboli volcano, Italy. Geology, 33, 425-428.

Le Bas, M.J., Le Maitre, R.W., Streckeisen, A., Zanettin, B., 1986. A chemical classification of volcanic rocks on the total alkali-silica diagram. J. Petrol., 27, 745-750.

Leung, I.S., 1974. Sector-zoned titanaugites: morphology, crystal chemistry, and growth. Am. Mineral., 59, 127-138.

Longerich, H.P., Jackson, S.E., Günther, D., 1996. Laser ablation inductively coupled plasma mass spectrometric transient signal data acquisition and analyte concentration calculation. J. Anal. At. Spectrom., 11, 899-904.

Lucchi, F., Francalanci, L., Keller, J., De Astis, G., Tranne, C.A., 2013. Geological map of Stromboli, scale 1:10,000 (Aeolian archipelago). In: Lucchi, F., Peccerillo, A., Keller, J., Tranne, C.A., Rossi, P.L. (eds). The Aeolian Islands Volcanoes. In: Geol. Soc. Lond. Mem., 37, enclosed DVD.

Marsella, M., Coltelli, M., Proietti, C., Branca, S., Monticelli, R., 2008. 2002-2003 lava flow eruption of Stromboli: a contribution to understanding lava discharge mechanisms using periodic digital photogrammetry surveys. In: Calvari, S., Inguaggiato, S., Puglisi, G., Ripepe, M., Rosi, M. (eds). The Stromboli volcano-an integrated study of 2002-2003 eruption. American Geophysical Union, Geophysical Monograph Series, 182, 229-246.

Marsh, B.D., 2007. Crystallization of silicate magmas deciphered using crystal size distributions. J. of the American Ceramic Society, 90, 746-757.

Marsh, B.D., 2002. On bimodal differentiation by solidification front instability in basaltic magmas, part 1: basic mechanics. Geochim. Cosmochim. Acta, 66, 2211-2229.

Marsh, B.D., 1996. Solidification fronts and magmatic evolution. Min. Mag., 60, 5-40.

Masotta, M., 2012. Magma differentiation in shallow, thermally zoned magma chambers: the example of Sabatini Volcanic District (central Italy). PhD Dissertation Sapienza-Università di Roma.

Masotta, M., Mollo, S., Gaeta, M., Freda, C., 2016. Melt extraction in mush zones: The case of crystal-rich enclaves at the Sabatini Volcanic District (central Italy). Lithos, 248, 288-292.

Masotta, M., Mollo, S., Freda, C., Gaeta, M., Moore, G., 2013. Clinopyroxene-liquid thermometers and barometers specific to alkaline differentiated magmas. Contrib. Mineral. Petrol., 166, 1545-1561.

Masotta, M., Freda, C., Gaeta, M., 2012. Origin of crystal-poor, differentiated magmas: insights from thermal gradient experiments. Contrib. Mineral. Petrol., 163, 49-65.

Masotta, M., Gaeta, M., Gozzi, F., Marra, F., Palladino, D.M., Sottili, G., 2010. H_2O- and temperature-zoning in magma chambers: the example of the Tufo Giallo della Via Tiberina eruptions (Sabatini Volcanic District, central Italy). Lithos, 118, 119-130.

Matthews, S.J., Sparks, R.S.J., Gardeweg, M.C., 1999. The Piedras Grandes-Soncor eruptions, Lascar volcano, Chile; evolution of a zoned magma chamber in the central Andean upper crust. J. Petrol., 40, 1891-1919.

McKenzie, D.P., 1985. The extraction of magma from the crust and mantle. Earth Planet. Sci. Lett., 74, 81-91.

McKenzie, D.P., 1984. The generation and compaction of partially molten rock. J. Petrol., 25, 713-765.

McNutt, S.R., 2005. Volcanic seismology. Annu. Rev. Earth Planet. Sci., 33, 461-491.

Métrich, N., Bertagnini, A., Di Muro, A., 2010. Conditions of magma storage, degassing and ascent at Stromboli: new insights into the volcano plumbing system with inferences on the eruptive dynamics. J. Petrol., 51, 603-626.

Métrich, N., Bertagnini, A., Landi, P., Rosi, M., Belhadj, O., 2005. Triggering mechanism at the origin of paroxysms at Stromboli (Aeolian archipelago, Italy): the 5 April 2003 eruption. J Geophys. Res., 32, L103056.

Métrich, N., Bertagnini, A., Landi, P., Rosi, M., 2001. Crystallisation driven by decompression and water loss at Stromboli volcano (Aeolian Islands). J. Petrol., 42, 1471-1490.

Mollo, S., Hammer, J., 2017. Dynamic crystallization in magmas. EMU Notes Mineral., 16, 373-418.

Mollo, S., Masotta, M., 2014. Optimizing pre-eruptive temperature estimates in thermally and chemically zoned magma chambers. Chem. Geol., 368, 97-103.

Mollo, S., Blundy, J.D., Scarlato, P., De Cristofaro, S.P., Tecchiato, V., Di Stefano, F., Vetere, F., Holtz, F., Bachmann, O., 2018. An integrated *P*-*T*-H_2O-lattice strain model to quantify the

role of clinopyroxene fractionation on REE+Y and HFSE patterns of mafic alkaline magmas: application to eruptions at Mt. Etna. Earth Sci. Rev., 185, 32-56.

Mollo, S., Giacomoni, P.P., Coltorti, M., Ferlito, C., Iezzi, G., Scarlato, P., 2015. Reconstruction of magmatic variables governing recent Etnean eruptions: constraints from mineral chemistry and *P*-*T*-f_{O2}-H_2O modelling. Lithos, 212-215, 311-320.

Mollo, S., Blundy, J.D., Iezzi, G., Scarlato, P., Langone, A., 2013. The partitioning of trace elements between clinopyroxene and trachybasaltic melt during rapid cooling and crystal growth. Contrib. Mineral. Petrol., 166, 1633-1654.

Mollo, S., Del Gaudio, P., Ventura, G., Iezzi, G., Scarlato, P., 2010. Dependence of clinopyroxene composition on cooling rate in basaltic magmas: implications for thermobarometry. Lithos, 118, 302-312.

Morelli, C., Giese, P., Cassinis, R., Colombi, B., Guerra, I., Luongo, G., Scarascia, S., Shutte, K.G., 1975. Crustal structure of Southern Italy. A seismic refraction profile between Puglia-Calabria-Sicily. Boll. Geofis. Teor. Appl., 18, 183-210.

Morgan, D.J., Blake, S., Rogers, N.W., DeVivo, B., Rolandi, G., Macdonald, R., Hawkesworth, C.J., 2004. Time scales of crystal residence and magma chamber volume from modelling of diffusion profiles in phenocrysts: Vesuvius 1944. Earth Planet. Sci. Lett., 222, 933-946.

Morimoto, N., 1988. Nomenclature of pyroxenes. Miner. Petrol., 39, 55-76.

Murphy, M.D., Sparks, R.S.J., Barclay, J., Carroll, M.R., Brewer, T.S., 2000. Remobilization of andesitic magma by intrusion of mafic magma at the Soufrière Hills Volcano, Montserrat, West Indies. J. Petrol., 41, 21-42.

Neave, D.A., Putirka, K.D., 2017. A new clinopyroxene-liquid barometer, and implications for magma storage pressures under Icelandic rift zones. Am. Mineral., 102, 777-794.

Nimis, P., Taylor, W.R., 2000. Single clinopyroxene thermobarometry for garnet peridotites. Part I. Calibration and testing of a Cr-in-Cpx barometer and an enstatite-in-Cpx thermometer. Contrib. Mineral. Petrol., 139, 541-554.

O'Hara, M.J., 1977. Geochemical evolution during fractional crystallisation of a periodically refilled magma chamber. Nature, 266, 503-507.

Pasquarè, G., Francalanci, L., Garduño, V.H., Tibaldi, A., 1993. Structure and geologic evolution of the Stromboli volcano, Aeolian islands, Italy. Acta Vulcanol., 3, 79-89.

Paton, C., Hellstrom, J., Paul, B., Woodhead, J., Hergt, J., 2011. Iolite: freeware for the visualisation and processing of mass spectrometric data. J. Anal. At. Spectrom., 26, 2508-2518.

Peccerillo, A., Taylor, S.R., 1976. Geochemistry of Eocene calcalkaline volcanic rocks from Kastamonu area, Northern Turkey. Contrib. Mineral. Petrol., 58, 63-81.

Peccerillo, A., De Astis, G., Faraone, D., Forni, F., Frezzotti, M.L., 2013. Compositional variations of magmas in the Aeolian arc: implications for petrogenesis and geodynamics. In: Lucchi, F., Peccerillo, A., Keller, J., Tranne, C.A., Rossi, P.L. (eds). The Aeolian Islands Volcanoes. Geol. Soc. Lond. Mem., 37, 489-508.

Perinelli, C., Mollo, S., Gaeta, M., De Cristofaro, S.P., Palladino, D.M., Armienti, P., Scarlato, P., Putirka, K.D., 2016. An improved clinopyroxene-based hygrometer for Etnean magmas and implications for eruption triggering mechanisms. Am. Mineral., 101, 2774-2777.

Petrone, C.M., Braschi, E., Francalanci, L., Casalini, M., Tommasini, S., 2018. Rapid mixing and short storage timescale in the magma dynamics of a steady-state volcano. Earth Planet. Sci. Lett., 492, 206-221.

Petrone, C.M., Bugatti, G., Braschi, E., Tommasini, S., 2016. Pre-eruptive magmatic processes re-timed using a non-isothermal approach to magma chamber dynamics. Nat. Commun., 7, 12946.

Petrone, C.M., Olmi, F., Braschi, E., Francalanci, L., 2006. Mineral chemistry profile: a valuable approach to unravel magma mixing processes in the recent volcanic activity of Stromboli, Italy. Period. Mineral., 75, 277-292.

Philpotts, A.R., Carrol, M., Hill, J.M., 1996. Crystal-mush compaction and the origin of pegmatitic segregation sheets in a thick flood-basalt flow in the Mesozoic Hartford Basin, Connecticut. J. Petrol., 37, 811-836.

Pistolesi, M., Rosi, M., Pioli, L., Renzulli, A., Bertagnini, A., Andronico, D., 2008. The paroxysmal explosion and its deposits. In: Calvari, S., Inguaggiato, S., Puglisi, G., Ripepe, M., Rosi, M. (eds). The Stromboli volcano-an integrated study of 2002-2003 eruption. American Geophysical Union, Geophysical Monograph Series, 182, 317-330.

Puglisi, G., Bonaccorso, A., Mattia, M., Aloisi, M., Bonforte, A., Campisi, O., Cantarero, M., Falzone, G., Puglisi, B., Rossi, M., 2005. New integrated geodetic monitoring system at Stromboli volcano (Italy). Engineer. Geol., 79, 13-31.

Putirka, K.D., 2017. Down the crater: where magmas are stored and why they erupt. Elements, 13, 11-16.

Putirka, K.D., 2008. Thermometers and barometers for volcanic systems. Rev. Mineral. Geochem., 69, 61-120.

Putirka, K.D., 1999. Clinopyroxene + liquid equilibria to 100 kbar and 2450 K. Contrib. Mineral. Petrol., 135, 151-163.

Putirka, K., Mikaelian, H., Ryerson, F., Shaw, H., 2003. New clinopyroxene-liquid thermobarometers for mafic, evolved, and volatile-bearing lava compositions, with applications to lavas from Tibet and the Snake River Plain, Idaho. Am. Min., 88, 1542-1554.

Putirka, K., Johnson, M., Kinzler, R., Longhi, J., Walker, D., 1996. Thermobarometry of mafic igneous rocks based on clinopyroxene-liquid equilibria, 0-30 kbar. Contrib. Mineral. Petrol., 123, 92-108.

Ripepe, M., Marchetti, E., Ulivieri, G., Harris, A.J.L., Dehn, J., Burton, M., Caltabiano, T., Salerno, G., 2005. Effusive to explosive transition during the 2003 eruption of Stromboli volcano. Geology, 33, 341-344.

Robinson, D.M., Miller, C.F., 1999. Record of magma chamber processes preserved in accessory mineral assemblages, Aztec Wash pluton, Nevada. Am. Mineral., 84, 1346-1353.

Rodríguez, C., Geyer, A., Castro, A., Villaseñor, A., 2015. Natural equivalents of thermal gradient experiments. J. Volcanol. Geotherm. Res., 298, 47-58.

Rosi, M., 1980. The island of Stromboli. Rendiconti della Società Italiana di Mineralogia e Petrologia, 36, 345-368.

Rosi, M., Pistolesi, M., Bertagnini, A., Landi, P., Pompilio, M., Di Roberto, A., 2013. Stromboli volcano, Aeolian Islands (Italy): present eruptive activity and hazards. In: Lucchi, F., Peccerillo, A., Keller, J., Tranne, C.A., Rossi, P.L. (eds). Geology of the Aeolian Islands (Italy). In: Geol. Soc. Lond. Mem., 37, 473-490.

Rosi, M., Bertagnini, A., Harris, A.J.L., Pioli, L., Pistolesi, M., Ripepe, M., 2006. A case history of paroxysmal explosion at Stromboli: timing and dynamics of the April 5, 2003 event. Earth Planet. Sci. Lett., 243, 594-606.

Rosi, M., Bertagnini, A., Landi, P., 2000. Onset of the persistent activity at Stromboli volcano (Italy). Bull. Volc. 62, 294-300.

Scandone, R., Acocella, V., 2007. Control of the aspect ratio of the chamber roof on caldera formation during silicic eruptions. Geophys. Res. Lett., 34, L22307.

Scarlato, P., Mollo, S., Petrone, C.M., Ubide, T., Di Stefano, F., 2019. Interpreting magma dynamics through a statistically refined thermometer: Implications for clinopyroxene Fe-Mg diffusion modeling and sector zoning at Stromboli. American Geophysical Union Books, in press.

Sheehan, F., Barclay, J., 2016. Staged storage and magma convection at Ambrym volcano. Vanuatu. J. Volcanol. Geotherm. Res., 322, 144-157.

Shibano, Y., Namiki, A., Sumita, I., 2012. Experiments on upward migration of a liquid-rich layer in a granular medium: implications for a crystalline magma chamber. Geochem., Geophys., Geosyst., Q03007.

Shimizu, N., 1981. Trace element incorporation into growing augite phenocryst. Nature, 289, 575-577.

Shirley, D.N., 1986. Compaction in igneous cumulates. J. Geol., 94, 795-809.

Spampinato, L., Calvari, S., Harris, A.J.L., Dehn, J., 2008. Evolution of the lava flow field by daily thermal and visible airborn surveys. In: Calvari, S., Inguaggiato, S., Puglisi, G., Ripepe, M., Rosi, M. (eds). The Stromboli Volcano. An Integrated Study of the 2002-2003 eruption. AGU, Washington, Geophysical Monograph, 182, 201-211.

Speranza, F., Pompilio, M., D'Ajello Caracciolo, F., Sagnotti, L., 2008. Holocene eruptive history of the Stromboli volcano: constraints from paleomagnetic dating. J. Geophys. Res., 113, B09101.

Taddeucci, J., Palladino, D.M., Sottili, G., Bernini, D., Andronico, D., Cristaldi, A., 2013. Linked frequency and intensity of persistent volcanic activity at Stromboli (Italy). Geophys. Res. Lett., 40, 1-5.

Tecchiato, V., Gaeta, M., Mollo, S., Scarlato, P., Bachmann, O., Perinelli, C., 2018a. Petrological constraints on the high-Mg basalts from Capo Marargiu (Sardinia, Italy): Evidence of cryptic amphibole fractionation in polybaric environments. J. Volcanol. Geotherm. Res., 349, 31-46.

Tecchiato, V., Gaeta, M., Mollo, S., Bachmann, O., von Quadt, A., Scarlato, P., 2018b. Snapshots of primitive arc magma evolution recorded by clinopyroxene textural and compositional variations: The case of hybrid crystal-rich enclaves from Capo Marargiu Volcanic District (Sardinia, Italy). Am. Mineral., 103, 899-910.

Tibaldi, A., 2001. Multiple sector collapses at Stromboli volcano, Italy: how they work. Bull. Volcanol., 63, 112-125.

Tibaldi, A., Corazzato, C., Apuani, T., Cancelli, A., 2003. Deformation at Stromboli volcano (Italy) revealed by rock mechanics and structural geology. Tectonophysics, 361, 187-204.

Tommasi, P., Baldi, P., Chiocci, F.L., Coltelli, M., Marsella, M., Pompilio, M., Romagnoli, C., 2005. The landslide sequence induced by the 2002 eruption at Stromboli volcano. In: Landslide-risk analysis and sustainable disaster management, 32, Springer, 251-258.

Ubide, T., Arranz, E., Lago, M., Galé, C., Larrea, P., 2012. The influence of crystal settling on the compositional zoning of a thin lamprophyre sill: A multi-method approach. Lithos, 132, 37-49.

Ubide, T., Kamber, B.S., 2018. Volcanic crystals as time capsules of eruption history. Nat. Commun., 9, 326.

Ubide, T., Mollo, S., Zhao, J.X., Nazzari, M., Scarlato, P., 2019a. Sector-zoned clinopyroxene as a recorder of magma history, eruption triggers, and ascent rates. Geochim. Cosmochim. Acta, 251, 265-283.

Ubide, T., Caulfield, J., Brandt, C., Bussweiler, Y., Mollo, S., Di Stefano, F., Nazzari, M., Scarlato, P., 2019b. Deep magma storage revealed by multi-method elemental mapping of clinopyroxene megacrysts at Stromboli volcano. Frontiers in Earth Sciences, in press.

Ubide, T., McKenna, C.A., Chew, D.M., Kamber, B.S., 2015. High-resolution LA-ICP-MS trace element mapping of igneous minerals: in search of magma histories. Chem. Geol., 409, 157-168.

Wadge, G., 1982. Steady state volcanism: evidence from eruption histories of polygenetic volcanoes. J. Geophys. Res., 87, 4035-4049.

Watson, E.B., Liang, Y., 1995. A simple model for sector zoning in slowly grown crystals: Implications for growth rate and lattice diffusion, with emphasis on accessory minerals in crustal rocks. Am. Mineral., 80, 1179-1187.

Welsch, B., Hammer, J., Baronnet, A., Jacob, S., Hellebrand, E., Sinton, J., 2016. Clinopyroxene in postshield Haleakala ankaramite: 2. Texture, compositional zoning and supersaturation in the magma. Contrib. Mineral. Petrol., 171, 6.

White, W.M., 2013. Geochemistry. John Wiley and Sons.

White, R., McCausland, W., 2016. Volcano-tectonic earthquakes: A new tool for estimating intrusive volumes and forecasting eruptions. J. Volcanol. Geotherm. Res., 309, 139-155.

Figure captions

Fig. 1. a) Location and aerial view (Google Earth) of Stromboli Island in the Aeolian archipelago, Sicily Province, in the southern Tyrrhenian Sea, Italy. b) TAS (Total Alkali vs. Silica; Le Bas et al. 1986) classification diagram and K_2O vs. SiO_2 diagram (Peccerillo and Taylor 1976). c) Variations in major and trace elements (Mg#, Ce, Cr, Al_2O_3/CaO, Zr, and Sr) over time.

Fig. 2. Thin section scans of black scoriae from 15/12/2017 normal activity, 01/11/2017 major activity and 05/04/2003 paroxysm and golden pumice from 05/04/2003 paroxysm.

Fig. 3. Classification scheme of clinopyroxene phenocrysts on the basis of their textural and chemical features. Group A consists of diopsidic antecrysts with augitic overgrowths, whereas Group B refers to phenocrysts in which the diopsidic cores are absent. The two groups have been further divided into sub-groups depending on the presence (Sub-group A1 or B1) or absence (Sub-group A2 or B2) of diopsidic bands, following the classification scheme proposed by Petrone et al. (2018). Sub-groups A1 and B1 are the least common in all samples (~4 vol.% and ~3 vol.%, respectively), Sub-group A2 is more common (~29 vol.%) than Sub-groups A1 and B1 and Sub-group B2 is recognized as the most abundant in all samples (~64 vol.%).

Fig. 4. Variations of Di, Hd, Jd, ∑Ts vs. Mg#. Di, diopside. Hd, hedenbergite. Jd, jadeite. ∑Ts, sum of Ca-Tschermak, CaFe-Tschermak and CaTi-Tschermak components.

Fig. 5. Variations of Yb, Zr, Sc, Cr vs. La diagrams.

Fig. 6. ΔDiHd (Putirka et al., 1996; Mollo et al., 2013), ΔD_{Na} (Blundy et al., 1995) and ΔD_{Ti}, (Hill et al., 2011; Mollo et al., 2018) equilibrium tests demonstrate the attainment of near-equilibrium crystallization between clinopyroxene and feeding melt.

Fig. 7. Probability density function for barometric (error of ± 136 MPa; Putirka et al., 1996), thermometric (error of ± 6 °C; Scarlato et al., 2019) and hygrometric (error of ± 0.5 wt.%; Perinelli et al., 2016) estimates. a) Gaussian distribution plots show that the augitic mantles and rims peak at low-*T* (~1,130 °C) and diopsidic cores and bands equilibrate at comparable high-*T* (~1,175 and ~1,165 °C, respectively). Pressure does not change significantly (160-190 MPa) among the different crystal portions, in agreement with the lack of substantial changes for the *P*-sensitive jadeite (e.g., Blundy et al., 1995) component in clinopyroxenes showed in Fig. 4. The variance of our pressure estimates spans the two main reservoirs recognized at Stromboli (e.g., Bertagnini et al., 2003; Landi et al., 2004; Aiuppa et al., 2010; Métrich et al., 2010). H_2O estimates (0.5-2.4 wt.%) consistently overlap within the hygrometer uncertainty of ± 0.5 wt.%, with the more evolved compositions of the matrix glass and clinopyroxene mantles/rims peaking at a slightly higher H_2O contents (~1.5 wt.%). b) Comparison between *P*-*T*-H_2O estimates and eruption dates highlighting an almost constant crystallization path over the fourteen years of the investigated volcanic activity.

Fig. 8. The compatible and incompatible behavior of Cr and Zr in clinopyroxenes, respectively, were examined for the diopsidic antecrysts and recharge bands in relation to the augitic overgrowths for each single eruption investigated in this study. The red curve represents the Rayleigh fractional crystallization (*FC*) vector that does not fully reproduce the clinopyroxene data for *F* values ranging from 1 to 0.79. Grey curves result from the *in situ* crystallization model (Langmuir, 1989) accounting for the contribution of residual melts trapped/extracted from the crystal mush, leading to less enrichments/depletions of incompatible/compatible trace elements. The trace element variability observed for the diopsidic-augitic clinopyroxene domains is most closely reproduced for *f* values between 0.8 and 0.5. Clinopyroxene sub-groups have been reported for each single event and timescale estimates were performed using the NIDIS model proposed by Petrone et al. (2016).

Phenocrysts erupted in 2003 do not show diopsidic bands surrounding resorbed cores making it possible to calculate timescales either at the resorbed core-inner mantle interface or across the diopsidic band. The Sub-group A2 only provides information about the minimum remobilization time of diopsidic antecrysts. No Fe-Mg compositional boundaries (i.e., no timescales) are found in clinopyroxenes from Sub-group B2.

Fig. 9. Working model for the extended plumbing system at Stromboli volcano during the a) Post-Pizzo period (Petrone et al., 2018) and the b) Present-day 2003-2017 activity (this study). During the Post-Pizzo period, the abundant occurrence of diopsidic bands is directly related to quasi-instantaneous timescales caused by rapid and voluminous injections of fresh *lp*-magmas triggering the eruption. This means that mafic *lp*-magmas do not stall within the crystal mush over prolonged time periods, and no antecrysts are transported into the shallow *hp*-reservoir. We propose that the 2003-2017 activity represents a new phase in the lifetime of Stromboli volcano, characterized by more efficient mechanisms of mush disruption and cannibalization, in which the old diopsidic antecrysts were continuously remobilized and transported by the *lp*-magmas permeating the mush. The disappearance of diopsidic recharge bands within augitic overgrowths with time (Fig. 8) indicates that injections feeding the persistent Present-day activity are efficiently mixed and homogenized. The ubiquitous formation of sector zoned phenocrysts within the plumbing system of Stromboli denotes that the crystal growth is controlled by kinetic effects that we link to magma degassing (e.g., Métrich et al., 2001, 2005, 2010; Bertagnini et al., 2003, 2008) and convection inducing low degrees of undercooling ($\Delta T = T_{liquidus} - T_{crystallization}$) (Mollo and Hammer, 2017; Ubide et al., 2019a, 2019b).

Fig. 10. a) W_0 (i.e., melt migration velocity; m/s) vs. Z_0 (i.e., thickness of the solidification front; m) from the equation of Bachmann and Bergantz (2004) to constrain the spatial distribution and physical state of the solidification front in terms of thickness and compaction, in which Φ corresponds to the porosity of the crystal mush. The green region corresponds to W_0 changes (from 10^{-10} to 10^{-9} m/s) of

highly porous mushy bodies under undergoing compaction, where Φ is within the range of 0.4-0.5 (McKenzie, 1984, 1985; Shirley, 1986; Bachmann and Bergantz, 2004). b) σ_c (local strength; bar) vs φ (crystal fraction) diagram modified from Marsh (2002). Values of $Z_0 \leq 400$ m and $\varphi \leq 0.6$ yield a characteristic strength of 0.3-2 bars, denoting tearing and disruption phenomena of the solidification front within the shallow *hp*-reservoir.

Fig. 1S. Major and trace element maps of clinopyroxene phenocrysts obtained with electron microprobe and with LA-ICP-MS, respectively.

Fig. 2S. Chondrite-normalized patterns of REE showing the trace element concentrations analyzed in bulk rocks and clinopyroxene phenocrysts.

Fig. 3S. Histogram diagram showing modal frequencies of thermometric (error of ± 6 °C; Scarlato et al., 2019), barometric (error of ± 136 MPa; Putirka et al., 1996) and hygrometric (error of ± 0.5 wt.%; Perinelli et al., 2016) estimates.

Fig. 4S. Back-scattered electron (BSE)-SEM images and grey value diffusion profiles (grey circles) of 12 representative clinopyroxene crystals calculated inside the blue area in the associated BSE-SEM images. Each diffusion profile is calculated (blue area) using the 'greyscale' procedure of Petrone et al. (2016) and calibrated against the chemical composition (Mg#) measured with the electron microprobe. The diffusion profiles across the boundaries have been modelled using the NIDIS code (Petrone et al., 2016). For each crystal zone we report the relative equilibrium temperature used in the NIDIS modeling.

Figures

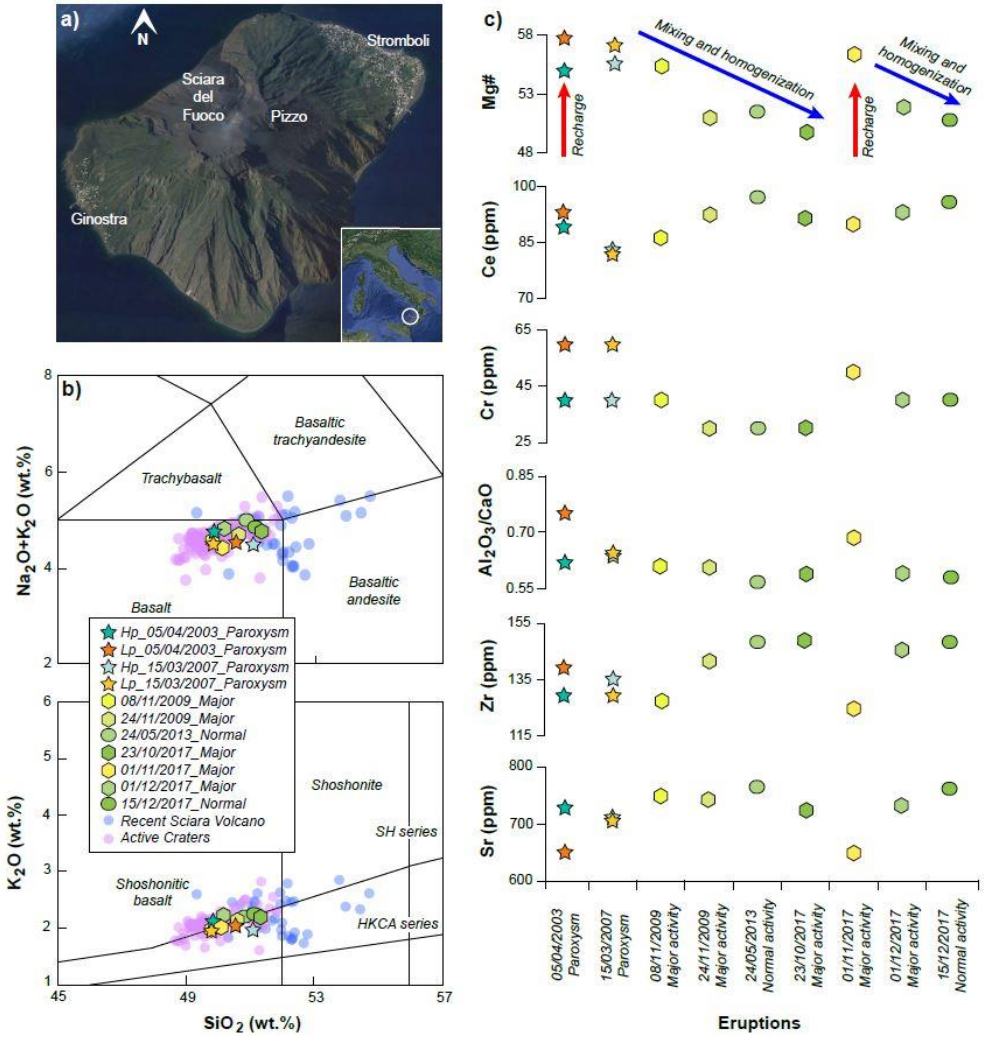

Figure 1

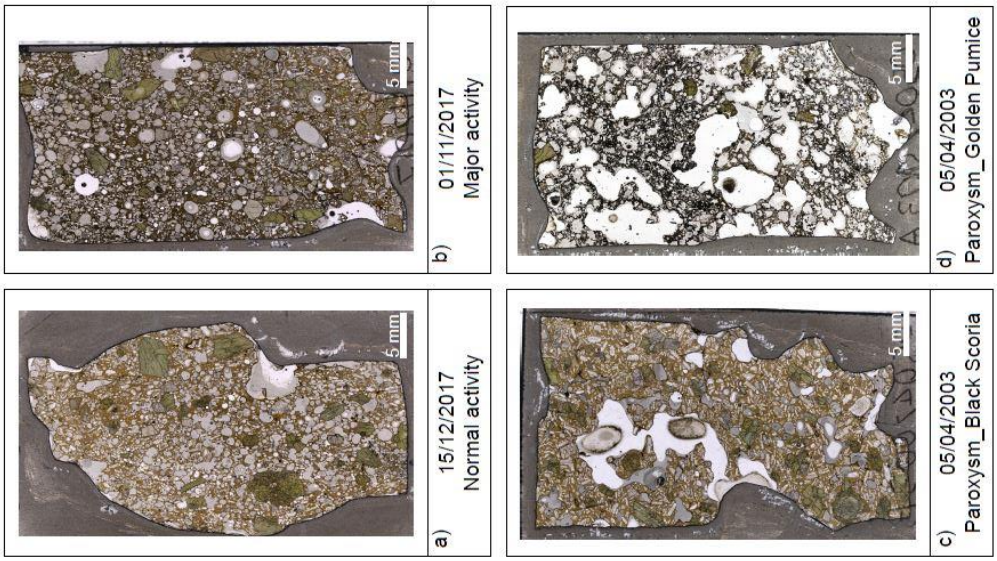

Figure 2

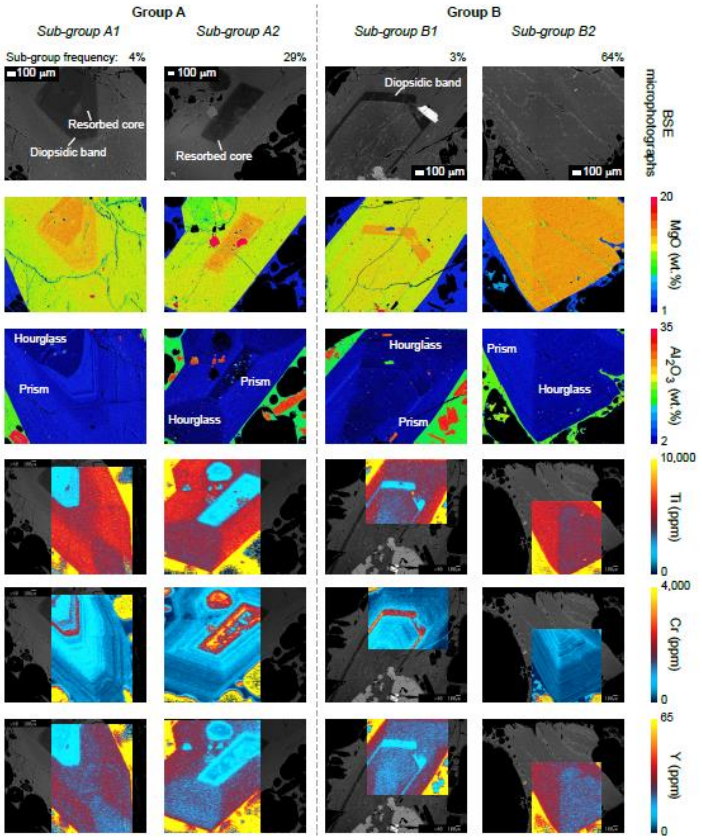

Figure 3

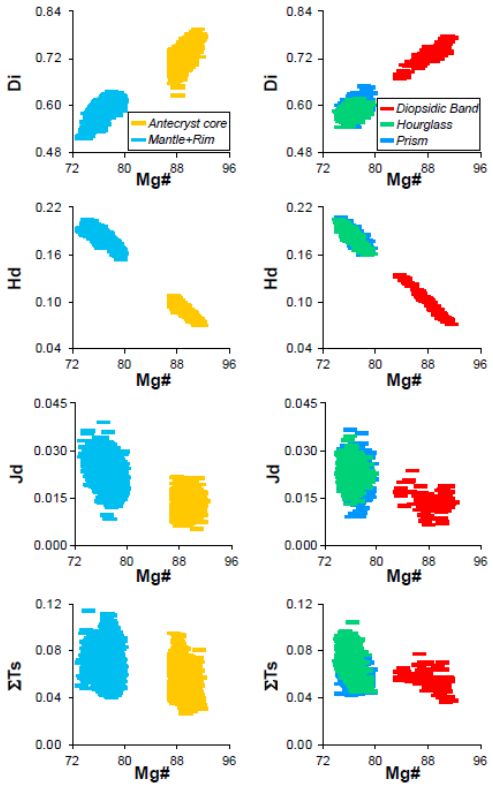

Figure 4

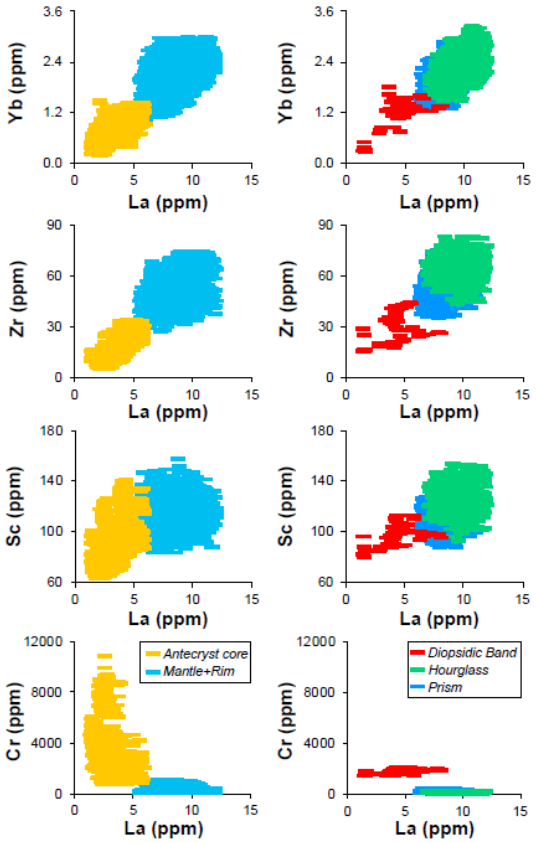

Figure 5

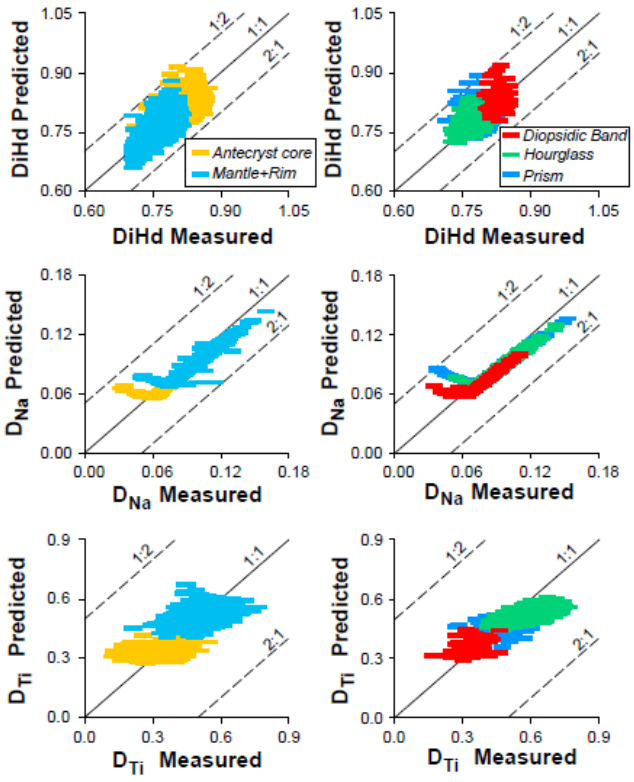

Figure 6

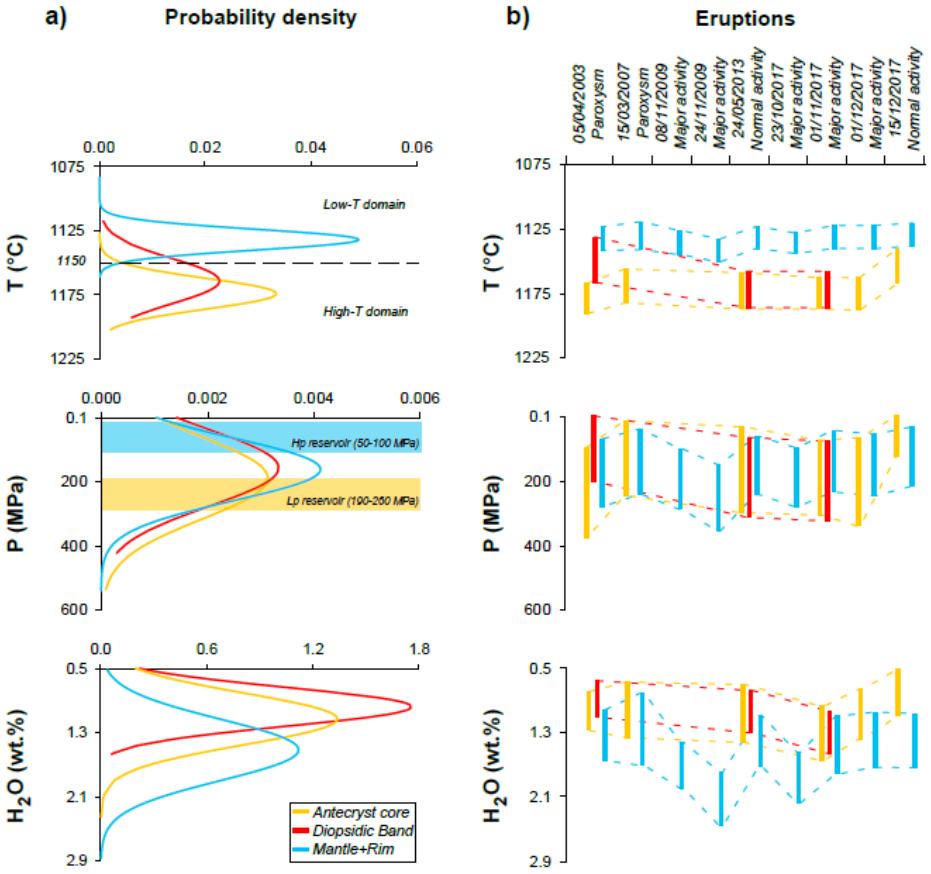

Figure 7

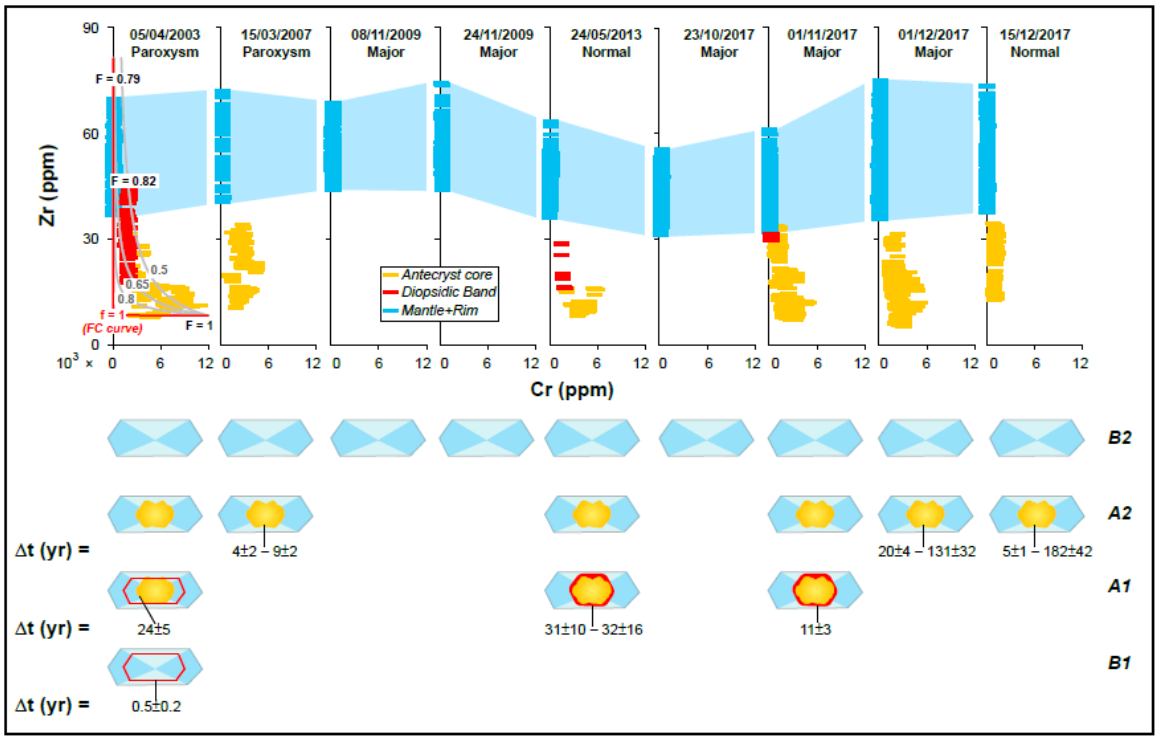

Figure 8

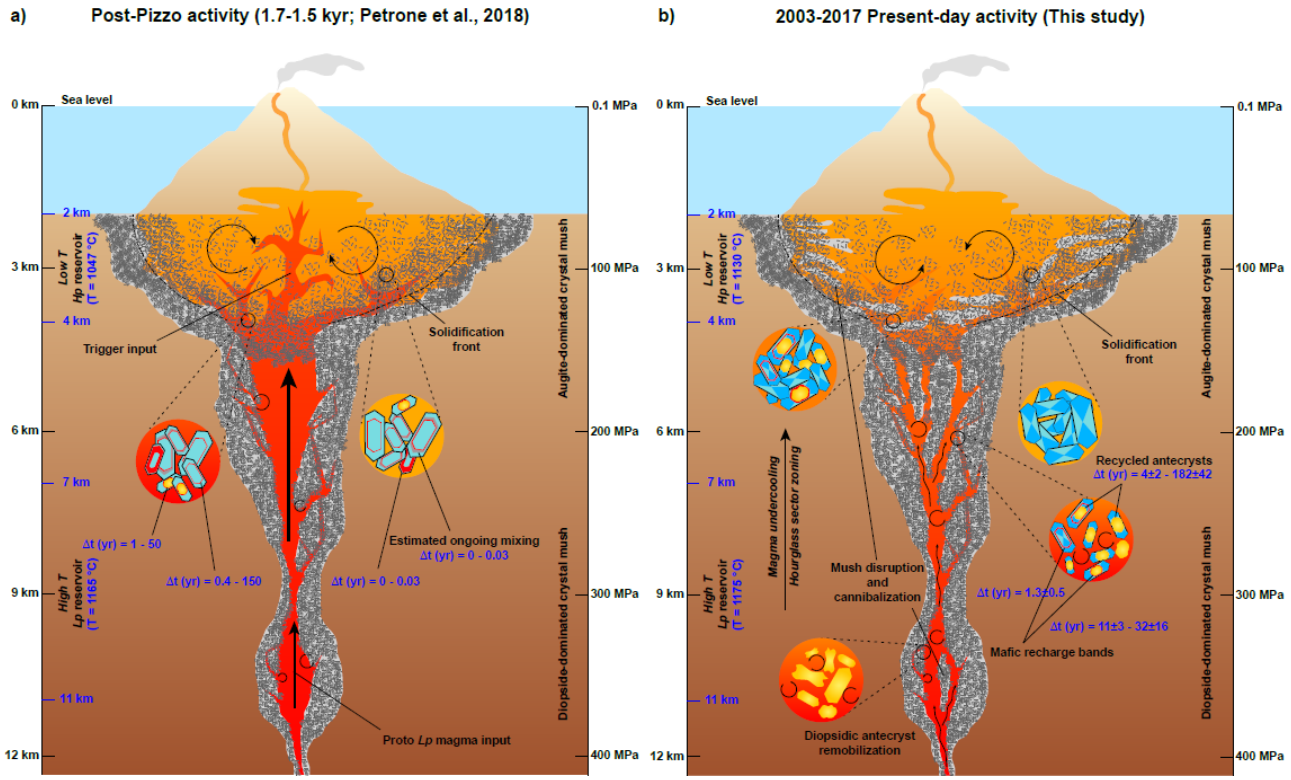

Figure 9

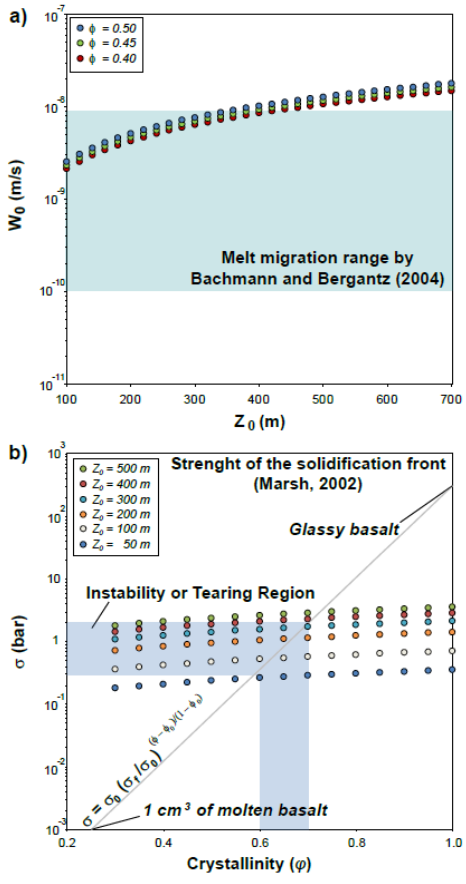

Figure 10

Supplementary data to this article can be found online at

https://drive.google.com/drive/folders/1_yvgMrDq1SFrz2PBUllLlTK6h0xloqM_?usp=sharing

Conclusions

A fundamental goal of the modern petrology is to provide quantitative constraints about the most effective pre-eruptive processes taking place in volcanic systems. Experimental investigations and very detailed chemical studies on zoned crystals from active volcanoes allow us to unravel the dynamics governing magmatic plumbing systems and their eruptive behavior over time. During the last decades, the incredible technological improvements have supported the progresses in terms of geophysical and geochemical monitoring, as well as our knowledge about magma chamber processes. First of all, the ability to track accurately the chemical evolution of active and quiescent volcanoes, together with the capacity to map the changes of the volcanic edifice through time have forced us to strongly revise our simple view of a classic plumbing system fed by a single magma chamber in which melt and solid phases are stored before the eruption. A dynamic concept of interconnected ponding zones forming a vertically-extended mush column is actually considered more realistic and matches well with the information obtained by different geophysical monitoring techniques (e.g., seismicity, ground deformations, microgravity variations). This drastic change in what we think about the architecture of volcanic plumbing systems implies also a drastic change in what petrology could provide about the determination of the ambient intensive thermodynamic variables (P, T, f_{O2}, H_2O, X) and timescales of the processes involved in the magmatic evolution.

In this PhD study, I have used the compositional variations in terms of major and trace element of experimental olivines and natural clinopyroxenes to gain quantitative information about basalt-carbonate interaction and geochemical evolution of different magmatic plumbing systems in Italy, namely the Colli Albani Volcanic District and Stromboli volcano, respectively. Divalent (Ni, Mg, Fe, Mn, Ca) and trivalent (REE, Y, Sc) cation partition coefficients between olivine and basaltic liquids have been experimentally investigated under the effect of carbonate assimilation. The compositional changes of olivine in primitive magmatic skarn environments has been determined during the first stages of the interaction between melt and host sedimentary rocks at the periphery of the magma chamber. The incorporation of divalent cation has been discussed to resolve the influence of

temperature, crystal chemistry and melt composition and structure. The contribution of crystal and melt during the crystallization of Fo-CaO-rich olivine from highly decarbonated basaltic melts has been statistically quantified for each element. Additionally, various predictive partitioning models from literature have been refined and readapted to evaluate the high-*T* decarbonation process. REE+Y+Sc substitution mechanisms in olivine have been explored in the framework of the lattice strain theory (i.e., r_0; E; D_0), demonstrating that the partitioning of trivalent cations requires maintenance of local charge-balance in olivine crystal structure by formation of vacancies disordered in both M1 and M2 octahedral sites. These data have been compared with natural compositions of olivines and related melt inclusions from cumulate and endoskarn rocks at the Colli Albani Volcanic District. Major and trace element concentrations in experimental olivine and residual melt successfully draw the AFC (assimilation, fractional crystallization) differentiation trend of high-*T* endoskarn and cumulate rocks formed at the early stage of magma contamination and differentiation.

Chemically zoned clinopyroxene phenocrysts from 2003-2017 eruptive period of Stromboli volcano have been investigated with quantitative analyses and mapping of major and trace elements. These novel data indicate multi-stage crystallization across the *lp-hp* reservoir, under stable *P*-*T*-H_2O conditions over time. Diopsidic bands are markers of mafic, high-*T* magma injections into the shallow reservoir, whereas resorbed diopsidic antecrysts testify to the mush cannibalism and disruption at different depths. Fe-Mg diffusion chronology across clinopyroxene compositional boundaries has been used to infer the timescales of these processes. Results show that relic diopsidic crystals were transported within the mush column over longer periods of time (up to 200 years) after the 2003 paroxysm, characterized by very short timescales (less than 1 year) estimated for the diffusive re-equilibration of compositional zoning across diopsidic bands. These data are also consistent with the *in situ* crystallization modeling of clinopyroxene phenocrysts within the solidification front of the crystal mush, where 50-80% of residual melts turned back towards the magma reservoir. Finally, the geochemical modeling has been coupled with an instability model of the solidification front. Indeed, this huge upward extraction of interstitial melts is related to failure and detachment of the growing

crystal structure at the roof of ~400 m thick solidification front, alongside modest but persistent seismicity ascribed to the shear-failure of crystalline bodies.

Acknowledgements

The present study was inspired by Prof. Silvio Mollo (Sapienza – University of Rome). I want to thank him for his patient supervision and fruitful discussions. Many thanks also to Dr. Piergiorgio Scarlato (Istituto Nazionale di Geofisica e Vulcanologia – Sezione di Roma 1) for his co-supervising all my research activities, providing economical support, experimental and analytical facilities and rock samples from Stromboli volcano.

I thank Dr. Manuela Nazzari for her assistance with the electron microprobe and with the scanning electron microscope. Special thanks also to Dr. Elisabetta Del Bello, Dr. Tullio Ricci, Dr. Jacopo Taddeucci (Istituto Nazionale di Geofisica e Vulcanologia – Sezione di Roma 1), and Dr. Daniele Andronico (Istituto Nazionale di Geofisica e Vulcanologia – Sezione di Catania) for their support during fieldwork and sampling activities.

I wish to thank Dr. Teresa Ubide, Dr. John Caulfield (University of Queensland), Prof. Olivier Bachmann, Dr. Marcel Guillong, and Dr Oscar Laurent (Institute of Geochemistry and Petrology - ETHZ) for their assistance with laser ablation inductively coupled plasma mass spectrometry analyses and mapping and for the inspiring discussions. I am also grateful to Dr. Chiara Maria Petrone (Natural History Museum – London) for teaching me the NIDIS (Non-Isothermal Diffusion Incremental Step) model and for hosting me at NHM in London. Special thanks also to Prof. Jonathan D. Blundy (University of Bristol) for his precious and instructive help to interpret the partitioning behavior of trivalent cations between olivine and basaltic melt.

Final thanks to all people of High Pressure High Temperature (HP-HT) Laboratory of Geophysics and Volcanology of the Istituto Nazionale di Geofisica e Vulcanologia – Sezione di Roma 1.